**Indian Institute of Technology Guwahati**

Doctoral Thesis

# Development of a Zonal Wavefront Sensor with Enhanced Performance Using a Reconfigurable Array of Binary Diffraction Gratings

**Mr. Biswajit Pathak**

**Roll No. 136121032**

Thesis submitted in partial fulfilment of the requirements for the degree of Doctor of Philosophy of the Indian Institute of Technology Guwahati, Guwahati, India.

**Supervisor: Dr. Bosanta R. Boruah**

**Computer Generated Holography Laboratory**
**Departmernt of Physics**
**Indian Institute of Technology Guwahati**
**Guwahati (Assam), India, Pin - 781039**

**October, 2017**

*Dedicated To My Beloved Parents*

# Declaration

**Mr. Biswajit Pathak**
Roll No.: 136121032
Department of Physics
Indian Institute of Technology Guwahati
Guwahati, India
E-mail:p.biswajit@iitg.ernet.in

---

I hereby declare that the results embodied in this thesis is the result of experiments carried out by me at the Department of Physics, Indian Institute of Technology Guwahati, Guwahati, India under the supervision of **Dr. Bosanta R. Boruah**. This thesis has not been submitted to any university/ institute or elsewhere for the award of any degree, diploma or associateship.

Mr. Biswajit Pathak

Date

# Certificate

**Dr. Bosanta R. Boruah**
Associate Professor
Department of Physics
Indian Institute of Technology Guwahati
Guwahati, India
E-mail:brboruah@iitg.ernet.in

---

This is to certify that the work contained in the thesis entitled **‘Development of a Zonal Wavefront Sensor with Enhanced Performance Using a Reconfigurable Array of Binary Diffraction Gratings’** by **Mr. Biswajit Pathak** (Roll No. 136121032), a student of Department of Physics, Indian Institute of Technology Guwahati, for the award of degree of Doctor of Philosophy, has been carried out under my supervision.

The present thesis or any part thereof has not been submitted elsewhere for award of any other degree, diploma or associateship.

Dr. Bosanta R. Boruah

Date

# Acknowledgements

The existence of this thesis is owed to the help, support and motivation of several people. At the very outset, I would like to offer my sincere gratitude to my thesis supervisor Dr. Bosanta R. Boruah for his continuous support throughout my Ph.D. work. Under his able guidance I was able to overcome all the hurdles that stood in my way and all such events served to be a good learning experience for me. The present work would not have materialized into reality without his support, encouragement and guidance.

Besides my advisor, I would like to thank the rest of my Doctoral committee members: Dr. Ashwini K. Sharma, Dr. Tarak N. Dey, Dr. Karuna Kalita for their encouragement, insightful comments and suggestions.

My sincere thanks also goes to the past (during the tenure of my PhD) and present HoD of Physics, Prof. Saurabh Basu and Prof. Poulose Poulose, and also to the entire staff of the Dept. of Physics IIT Guwahati, for providing me the necessary help and the opportunity to utilize different resources of the department to pursue my Ph.D. work.

I take this opportunity to sincerely acknowledge the partial financial support received from DIT, India during my Ph.D work. In addition I would also like to thank all the journal reviewers for their constructive advices.

I would like to thank all my past and present labmates: Abhijit Das, Md. Gaffar, Debapriya Roy, Mobarak Hossain, Santanu Konwar, Ranjan Kalita, S. S. Goutam Buddha, Nagendra Kumar, Karuna Sindhu Malik for the stimulating discussions we had during the Ph.D. work. It is a pleasure to offer my sincere thanks to all the SPIE IIT Guwahati student chapter members for working together in organizing all those life-long cherishing activities and placing their trust in me during my tenure as President of the chapter.

I am indebted to all my school teachers at Salt Brook School and later at Salt Brook Academy, my professors at Cotton College, IIT (ISM) Dhanbad and IIT Guwahati for imparting their service selflessly. They provided me with extensive personal and professional guidance and taught me a great deal about both scientific research and life in general. All the knowledge that I gained under their tutelage has made me the person I am today. I would like to express my deep gratitude to Ashwini Dowerah sir (ex-Principal of SBS and SBA) for his encouraging words and waiving my tution fees during my school days. His magnanimous gesture brought a lot of relief to our family during our personal as well as financial crisis. My sincere thanks and appreciation also goes to Porag sir and Varsha maa'm for their kindness and being more than a teacher to me.

I would like to thank my family members: my parents, Lt. Birendra N. Pathak, Mrs. Runumi Pathak and to my sisters (Jimli and Soonmoni) and brother (Dibojit) for their unconditional love and support throughout my life and my studies. Their patience and sacrifice will remain my inspiration throughout my life. This journey would not have been possible without them and so I dedicate this milestone to them.

Personally, I would like to acknowledge all my close friends at IIT Guwahati for the wonderful times we shared together and also providing me with the necessary distractions from my research that made my stay at IIT Guwahati memorable.

I offer my heartfelt gratitude to Pranjal, Shishir, Vivek, Siddharth, Ankur, Angkhuman, Dipankar, Ashim, Bidyut, Mukesh, Sourav, Pallabi, Arfeena, Madhusmita, Rajashree, Parthana for being with me in all thicks and thins of my life. I consider myself really fortunate to have friends like them in my life. Particular thanks goes to Monmi for her infallible love and support during my stressful and difficult moments. She has been a constant source of moral support and motivation, which drives me to give my best.

# Abstract

The Shack Hartmann wavefront sensor (SHWS) is a widely used zonal wavefront sensor, named after Johannes Franz Hartmann and Roland Shack. It consists of a 2D array of micro-lenses called lenslets along with a detector placed at the common focal plane of these micro-lenses. If a plane wavefront, is incident on the lenslet array, it generates an evenly spaced grid of spots on the focal plane of the lenslets array. However, a deviation of the incident wavefront from a plane wavefront will produce a displacement of the focal spots from their original locations. The shifts of the focal spot centroid positions with respect to the reference positions contain information of the local wavefront slopes of the incoming distorted wavefront. These local slope information can be used in a standard estimation algorithm to obtain the phase profile of the incident beam. Therefore, the SHWS comprises two essential steps, namely, the wavefront sensing and the wavefront estimation. Unfortunately, a conventional SHWS encounters a number of issues in the process of wavefront sensing and wavefront estimation that puts limitations in the performance of the sensor.

The conventional SHWS has a fixed layout of lenses which leads to a fix dynamic range as there exists no option to dynamically vary the number of lenslets. Besides, the conventional SHWS uses a digital camera to capture the focal spot array which usually has a low frame rate that limits the sensing frame rate of the sensor. On the other hand, an appropriate estimation geometry along with an estimation algorithm is mandatory for accurate measurement of wavefront in a SHWS. It is to be noted here that an appropriate estimation algorithm should be evaluated in terms of the associated error propagation. A robust estimation algorithm is expected to have less error propagation in regards to the important sources of error associated with it. Further, the SHWS has limited spatial resolution due to the limited number of lenses used in sampling the incident wavefront. Scientific literature reveals several schemes to enhance the spatial resolution in the estimated wavefront in SHWS; however, the improvement comes at the expense of slower sensor frame rate. Another important aspect of the sensing process of a SHWS is the accuracy associated with the detection of the focal spot centroid position. The conventional SHWS has limited centroid detection accuracy due to the fixed number of pixels describing the sensor area of the digital camera. Existing ways to improve the accuracy comes at the cost of extensive

pre-processing or post-processing of the data. Yet another important limitation of the SHWS is the fabrication of the lenslets array, as it is considered to be a specialized as well as tedious job because of the number of steps involved. Recent developments in the fabrication technology has minimised its associated issues to a great extent. However, it still remains incompatible to many applications that require an easy and affordable fabrication scheme and that can deliver a lenslet array of reasonably good performance while the sensor parameters can be easily modified as when required by the application.

In view of the above issues related to wavefront sensing and wavefront estimation in a conventional SHWS, the present thesis aims to develop a grating array based zonal wavefront sensor where the same issues can be addressed. The sensor in the thesis work uses a two dimensional array of plane diffraction gratings and a single focusing lens. This arrangement thus replaces the lenslets array of the SHWS, thereby overcoming the limitations associated with the lenslets array. We call such an arrangement as grating array based zonal wavefront sensor (GAWS). The proposed sensor is implemented using a liquid crystal spatial light modulator (LCSLM), employing a computer generated holography technique. In this thesis we introduce an improved wavefront estimation algorithm, applicable for Shack-Hartmann type wavefront sensors that shows significant improvement in the wavefront estimation. We also theoretically analyze the performance of the proposed wavefront estimation algorithm in a comprehensive manner by quantifying the important sources of error associated with it. Further, we introduce a scheme to enhance the spatial resolution of the GAWS by using a sequence of laterally shifted binary grating array patterns, realised with the help of the 24 bit-planes display of a ferroelectric LCSLM. We also propose a scheme to improve the accuracy of centroid detection and enhance the dynamic range of the sensor or reduce the possibility of crosstalk, in the GAWS by using more than one digital camera plane via a beam splitting mechanism. In addition, we describe the use of a print of an array of binary diffraction gratings on a transparent polyester sheet as a cost effective means to implement the GAWS. Each of the proposed schemes is demonstrated with the help of proof-of-principle experiments. Thus, in the present thesis, along with the description of the proposed schemes, we present experimental results in order to emphasize the effectiveness of each of the schemes.

# Acronyms

| | | |
|---|---|---|
| SHWS | - | Shack Hartmann Wavefront Sensor |
| GAWS | - | Grating Array Based Zonal Wavefront Sensor |
| CCD | - | Charged Coupled Device |
| CMOS | - | Complementary Metal Oxide Sensor |
| CGH | - | Computer Generated Holography |
| FT | - | Fourier Transform |
| PC | - | Personal Computer |
| FLC | - | Ferro-electric Liquid Crystal |
| ID | - | Iris Diaphragm |
| LC | - | Liquid Crystal |
| SLM | - | Spatial Light Modulator |
| LCSLM | - | Liquid Crystal Spatial Light Modulator |
| NLCSLM | - | Nematic Liquid Crystal Spatial Light Modulator |
| FLCSLM | - | Ferroelectric Liquid Crystal Spatial Light Modulator |
| SME | - | Slope Measurement Error |
| ADE | - | Algorithm Discretization Error |
| LSR | - | Low Spatial Resolution |
| HSR | - | High Spatial Resolution |
| MPE | - | Maximum a Posteriori Estimator |
| FWHM | - | Full Width at Half Maximum |

# Contents

# List of Figures

# List of Tables

## CHAPTER 1

# General Introduction

## 1.1 Introduction

A wavefront of a light beam is the surface defined by the locus of points in the beam having the same phase or the same optical path length from the source of light. The contour of such a wavefront of light beam may get changed when it is reflected from a surface or transmitted through a medium. It is seen that the reflecting surface or the medium of propagation has such a profound effect on the profile of the wavefront that the information contained in it may be lost. Therefore, in such a situation, extracting the original information carried by the beam of light becomes crucial. This requires a device, that can measure the wavefront of an incident light beam, known as the wavefront sensor [1, 2]. The wavefront sensors have been playing an important role in various field of applications such as adaptive optics [3, 4], laser beam characterization [5], astronomy [6], ophthalmology [7], optical shop testing and metrology [8, 9], optical trapping [10], and so on. Based on the working principle, the wavefront sensors are broadly classified into geometric sensors and interferometric sensors [11]. Both the types of sensors have their respective advantages and limitations. However, the geometric sensors are considered to be more robust than the interferometric sensors for the type of applications mentioned above [11]. The geometric sensors are further classified into zonal wavefront sensor and modal wavefront sensor [12]. Zonal wavefront sensors make discrete measurement over the local slope of each segment after dividing the incident wavefront into a number of segments. Thereafter, the information of all the local slopes are combined and the profile of the entire beam is obtained. On the other hand, the modal wavefront sensor expresses the incident phase profile in the form of a linear combination of orthogonal phase functions [13] (such as the Zernike, Fourier, etc.) by looking at the property of the focused beam. A major limitation of the modal wavefront sensing arises from the compulsory requirement of the orthogonality of the Zernike polynomials (or any other basis function) over the sampling geometry. An arbitrary wavefront may not accurately be represented by a combination of limited number of Zernike polynomials. Moreover, a zonal wavefront sensor provides more quantitative information of the wavefront in comparison to the modal wavefront sensor [14, 15]. Hence, the zonal wavefront sensor is considered to be more robust than the modal wavefront sensor [16, 17] to measure arbitrary distortions in the beam.

One of the widely used zonal wavefront sensors for the type of applications mentioned above is the Shack Hartmann wavefront sensor (SHWS), named after Johannes Franz Hartmann and Roland Shack [16]. It is a modified version of the original Hartmann wavefront sensor developed in 1904 by J. Hartmann [18]. The SHWS consists of an array of microlenses (each having same focal length and aperture size) along with a detector placed at the common focal plane of these microlenses. The detector is used to capture the focal spot corresponding to each of the lenslets. A regularly spaced grid of spots are obtained on the focal plane of the lenslets array for a plane incident wavefront. However, introduction of any distortion into the incident wavefront will displace the spots from their original locations (also known as the reference position). The shift of the focal spot centroid positions with respect to the reference positions depends on the information of the local wavefront slopes of the incoming distorted wavefront. These local slope information can be used in an estimation algorithm [12] in order to obtain the phase profile of the incident beam. Thus, a basic wavefront sensor, including the SHWS has two essential steps, namely, the wavefront sensing and the wavefront estimation. Wavefront sensing refers to the process of locating the centroid position corresponding to the sampled wavefront, whereas, wavefront estimation refers to the process of working on the data collected during wavefront sensing by using a standard estimation algorithm.

However, the process of wavefront sensing and wavefront estimation in a Shack-Hartmann type zonal wavefront sensor is associated with a number of issues or limitations that influence its performance. A conventional SHWS uses a digital camera to capture the focal spot array which has a low frame rate. Consequently the sensor has a limited sensing frame rate. The frame rate of the camera can be increased by reducing the effective number of rows in the camera, however, this will lead to a reduction in the dynamic range of the sensor.

For accurate measurement of wavefront in a wavefront sensor, it requires an appropriate estimation geometry along with an estimation algorithm. The estimation geometry is referred to the geometrical arrangement of the scheme while the estimation algorithm refers to the equations involved in the scheme. There are three basic estimation geometries available so far, which were proposed by Hudgin [19], Fried [20], and Southwell [12]. Of the three geometries, as far as robustness [21] and error propagations are concerned, Southwell geometry is considered to be the best. In the Southwell geometry, both the x-slopes and y-slopes are measured at the same point where the phase is to be estimated. The Southwell geometry has been the popular geometry for wavefront estimation, nevertheless there have been efforts to further improve the accuracy of wavefront estimation beyond that is achievable with the Southwell geometry. This includes a dither-based sensor proposed [22] to remove the inconsistency in wavefront estimation and iterative compensation [23] method to remove the imperfection in the Southwell geometry. Both the methods have shown significant improvement in accuracy, yet the improvement has been achieved only at the cost of processing time. Recently, the concept of truncation error in integration equations was introduced to reduce the estimation error in the Southwell geometry [24]. The truncation error can be minimised by incorporating more number of slopes in the integral equation. However, in this method only the vertical and the horizontal slope values are considered in the integral equation. Thus, efforts are still on to come up with a more efficient estimation algorithm that can further improve the estimation performance over the Southwell algorithm, without compromising much with the processing time.

While selecting an estimation algorithm it is very important to assess the performance of the estimation algorithm in terms of the error propagation. Two important sources of error in the estimation process are the algorithm discretization error and the slope measurement error [12, 21]. A robust estimation algorithm is also expected to have superior error propagation performance in regards to these important sources of error.

The spatial resolution of a conventional SHWS is defined by the fixed number of lenses in the lenslets array used in the sampling of the incident wavefront. One simple way to enhance the spatial resolution of the sensor would be to reduce the diameter of the lenslets used. However, such an approach will result in the increased size of the diffraction-limited focal spot. Alternatively, one can also reduce the diameter of the lens subaperture together with the reduction in the focal length of the lens. However, this approach will demand a digital camera with higher spatial resolution and also, a reduction in the focal length will reduce the sensitivity of the wavefront sensor. Scientific literature reveals several reports on enhancement of spatial resolution; however, the improvement comes at the expense of slower sensor frame rate.

Accuracy in locating the focal spot centroid is another important aspect in the sensing process of a SHWS. More the number of pixels over which the focal spot is defined, smaller is the error in locating its centre. Thus, it is expected in a SHWS that the focal spots are defined with a full width at half maximum which is much larger than the size of a single pixel. This will require the focal spots to be imaged by a camera which has large number of pixels. However, the digital camera has fixed number of pixels describing the sensor area, which puts an upper limit in the centroid detecting accuracy in the conventional SHWS.

Previously the construction of the lenslets array was quite tedious, considering the number of steps involved in the process which included cutting and polishing of glass slab with certain shape, individual mounting of each lens, etc. [25]. Recent developments in the field of binary optics technology has minimised the fabrication related issues to a great extent. Nowadays, customized computer aided design (CAD) program has made the process of designing the lenslets quite easier. This leads to the designing of lenslets of various shape, size or pattern [26, 27]. However, if an application requires frequent and onsite modification of the lenslets array parameters, such a state of the art fabrication facility may not easily be made available at the site of the application. Thus, many applications require an easy and affordable fabrication scheme that can deliver a reasonably good performance such that the sensor parameters can be easily modified as and when required by the application.

In view of the above issues related to wavefront sensing and wavefront estimation of a conventional SHWS, the present thesis aims to develop a grating array based zonal wavefront sensor with enhanced performance. It uses a two dimensional array of tiny plane diffraction gratings and a single focusing lens [28]. This arrangement thus replaces the lenslets array of the SHWS, thereby overcoming the limitations associated with the lenslets array. We call such an arrangement as grating array based zonal wavefront sensor (GAWS). The proposed sensor is implemented using a liquid crystal spatial light modulator (LCSLM), employing a computer generated holography technique [29, 30].

An array of grating elements, each having specific spatial frequencies, are first numerically constructed in such a way that each element has the same shape and size of the aperture and are uniformly distributed. For convenience of implementation, the grating elements are considered to have a binary transmittance function. The grating array pattern is then written onto the LCSLM panel via a computer interface. When a laser beam is incident, the LCSLM panel behaves like an array of plane diffraction grating, diffracting the incident beam into 0, $\pm 1$, $\pm 3$, $\pm 5$, $\cdots$ and so on orders with gradually decreasing intensities. When the diffracted beams are focused using a lens, the location of a focal spot is decided by the corresponding diffraction order and spatial frequencies in the grating element. Thus, by choosing the spatial frequencies appropriately and for a plane incident wavefront it is possible to send one of the diffracted orders to form an array of focal spots, in a way very similar to the focal spot array formed by the lenslet array of SHWS. Although any diffraction order can produce a focal spot array; however, in our work we have chosen the $+1$ diffraction order as the beam in this case has the maximum energy. As stated earlier, we incorporate a computer generated holography technique to construct the grating element so that the $+1$ order diffracted beam carries a user defined phase profile. As such each grating element is in fact a binary hologram that can be reconfigured dynamically at the refresh rate of the LCSLM. The focal spot array of the $+1$ order beams, likewise the SHWS, get shifted from their ideal positions if the incident beam contains any distortion. The shifts in the centroid positions are associated with the local wavefront slopes which can be employed to estimate the unknown wavefront by using an appropriate estimation algorithm.

The GAWS offer a number of flexibilities and advantages over the SHWS. In the case of GAWS, the focal spot for a certain grating element may not necessarily be at a fixed position with respect to the centre of the grating element, unlike the SHWS, where the focal spot is located on the optical axis of the lenslets. Separation between two adjacent focal spots in the case of GAWS can be changed by modifying the spatial frequencies of the grating elements. Thus, it offers a flexible dynamic range. In the case of GAWS, the focal spot array in the case of an unaberrated incident beam does not need to follow same geometry as the grating array and it can be configured to have lesser number of rows than the number of rows of the grating array. This facilitates enhancing the frame rate of the digital camera that images the array of focal spots, as the camera can be operated with lesser number of active rows. The same can also reduce the crosstalk in the vertical direction.

The GAWS can be implemented using a fast response ferroelectric LCSLM that can display at least 1440 binary patterns in one second. We have utilised this facility to programmably incorporate lateral shifts in the grating array in order to enhance the spatial resolution in wavefront estimation. We could enhance the spatial resolution without compromising much on the sensing frame rate. The programmability of the focal spot array further facilitates use of more than one digital camera to record just one focal spot array by splitting the single array into sub-arrays. This allows enhancing the centroid detecting accuracy without affecting the dynamic range of the sensor.

The numerically constructed grating array can also be synthesized by printing it on a polyester film (i.e. OHP sheet) using an ordinary laser printer. The grating array on the polyester film offer reasonable quality and uniformity. Thus, grating arrays of different parameters based on specific applications can be realised in an easy and affordable way.

We have also come up with a zonal wavefront estimation algorithm which is an improved version over the well-known Southwell algorithm. The proposed algorithm offers better accuracy without sacrificing much on the processing time. It also has superior performance in terms of error propagation during the estimation process.

The present thesis describes various schemes proposed to address the issues with the conventional SHWS. Each of the proposed schemes has also been demonstrated with the help of proof-of-principle experiments. Thus, along with the description of the schemes, the thesis presents results of the various proof-of-principle experiments in order to emphasize the effectiveness of each of the schemes.

Below we provide an overview of the present thesis.

In **chapter1**, we provide a general introduction to the research problem. It begins with an introduction to wavefront sensors and primarily, to the popular Shack-Hartmann wavefront sensor (SHWS). Afterwards, we provide a brief overview of the various limitations associated with the sensing and estimation in a SHWS type zonal wavefront sensor. We then introduce the grating array based wavefront sensor and briefly discuss how some of the issues with the conventional SHWS can be addressed. This is followed by a chapter-wise overview of the entire thesis.

In **chapter2**, we present a discussion about the two basic aspects associated with a Shack-Hartmann type zonal wavefront sensors, namely, the wavefront sensing and the wavefront estimation. It begins with a brief discussion on fundamentals of zonal wavefront sensing and modal wavefront sensing. The working principles of the important sensors falling under each, zonal wavefront sensing (i.e. Shack Hartmann wavefront sensor) and modal wavefront sensing (i.e. Curvature wavefront sensor) are also described briefly. This is followed by a short discussion on the two types of estimation processes, namely, the zonal wavefront estimation and the modal wavefront estimation. Finally, we provide a brief discussion related to the three important estimation geometries associated with the wavefront estimation process.

In **chapter3**, we describe the development of a robust grating array based zonal wavefront sensor (GAWS). It begins with a discussion on the generation of user defined wavefront and dynamic control of the +1 order beam, using computer generated holography technique. Then, an elaborate discussion about the construction and working of the GAWS is provided. This is followed by a brief introduction on the various components associated with the GAWS. We then illustrate experimental implementation of GAWS and provide experimental results that show efficient working of the sensor for different grating array dimensions. Finally, we present results to show how the GAWS, helps in realizing a faster frame rate and reduces the crosstalk along the vertical direction, due to its ability to form 1D array of focal spots.

In **chapter4**, we introduce an improved version of the Southwell algorithm applicable for zonal wavefront estimation in a Shack-Hartmann type wavefront sensor. The chapter begins with a brief literature survey of various existing approaches to improve the accuracy of wavefront estimation (related to Shack-Hartmann type wavefront sensor). Then we provide the mathematical expressions developed for the proposed algorithm along with the expressions for the Southwell algorithm. This is followed by the illustration of experimental implementation of the proposed algorithm and the Southwell algorithm. Finally, we present experimental results that demonstrate significant improvement in the wavefront estimation, using the proposed algorithm, relative to the Southwell algorithm.

In **chapter5**, we theoretically analyze the two important sources of error associated with the improved wavefront estimation algorithm (introduced in chapter 4) and made a comparative study of the same with the Southwell algorithm. It begins with a brief introduction about the two important sources of error, namely, the slope measurement error and the algorithm discretization error. Then, we provide an analytical work out to quantify the amount of slope measurement error for both the Southwell algorithm and the improved algorithm. Further, using Taylor series expansion, we also analytically quantify the algorithm discretization error for both the Southwell algorithm and the improved algorithm. The analytical expressions suggest that both the errors decrease as the grid dimension of the sensing scheme increases. Finally, we present experimental results that validate the analytical workout developed in the chapter and demonstrate the dependency of these errors with the experimentally obtained root mean square (RMS) errors.

In **chapter6**, we introduce a scheme which can effectively enhance the spatial resolution of the grating array based zonal wavefront sensor (GAWS) to a significant extent. It begins with a brief literature survey of the existing approaches to enhance the spatial resolution of a Shack-Hartmann type wavefront sensor and the associated limitations. This is followed by a detailed description of the spatial resolution enhancement scheme through the use of a fast response ferroelectric liquid crystal spatial light modulator (FLCSLM). Afterwards, we illustrate a proof-of-concept experiment to implement the proposed spatial resolution enhancement scheme. The proposed scheme shows the enhancement in spatial resolution at a frame rate equivalent to the standard refresh rate of the video signal or even at a faster rate. Finally, we provide experimental and numerical results that demonstrate the efficient working of the proposed scheme which can detect spatial wavefront features that would have been missed by the conventional method.

In **chapter7**, we propose a scheme to improve the accuracy of centroid detection in the grating array based zonal wavefront sensor (GAWS) by using more than one digital camera via a beam splitting mechanism. It begins with a literature survey of the existing methods to improve the accuracy of centroid detection in a Shack-Hartmann type wavefront sensor. We then provide a detailed description of the proposed scheme by using multiple digital cameras to locate an array of focal spots. This is followed by experimental implementation of the proposed scheme that illustrates describing each of the focal spots with more number of pixels over a larger detector subaperture area. Finally, we show that such an arrangement can also enhance the dynamic range of the sensor and reduce the possibility of crosstalk between adjacent zones.

In **chapter8**, we describe the design and fabrication of a grating array based zonal wavefront sensor (GAWS) using a print of an array of binary diffraction gratings on a transparent polyester sheet. The chapter begins with a literature survey of the existing methods to fabricate high quality lenslets for the SHWS and the associated limitations. We then provide mathematical relations involving the controllable parameters of the grating array to generate an array of well separated $+1$

order focal spots, for a given focusing lens. This is followed by a brief description of the experimental implementation of the proposed sensing method. We then present experimental results that show the generation of +1 order focal spots, agreeing well with the numerical simulation results and that demonstrate a reasonably accurate estimation of an applied phase profile of the incident beam.

In **chapter9**, we provide a brief summary of the important research findings of the thesis work along with the possibilities of future relevant research explorations.

## 1.2 Conclusion

In this chapter, we have provided a general introduction to the research problem. It begins with an introduction to wavefront sensors and primarily, to the popular Shack-Hartmann wavefront sensor (SHWS). Afterwards, we provide a brief overview of the various limitations associated with the sensing and estimation in a SHWS type zonal wavefront sensor, and the proposed schemes to address the same. This is followed by a chapter-wise overview of the entire thesis.

## CHAPTER 2

# Introduction to Wavefront Sensing and Wavefront Estimation Methods

## 2.1 Introduction

In this chapter, we discuss two essential aspects, namely, the wavefront sensing and the wavefront estimation, associated with a basic wavefront sensor. The first part of this chapter presents a discussion on fundamentals of zonal wavefront sensing and modal wavefront sensing. The working principles of the important sensors falling under each, zonal wavefront sensing (Shack Hartmann wavefront sensor) and modal wavefront sensing (Curvature wavefront sensor) are described briefly. The second part discusses two wavefront estimation processes, namely, the zonal wavefront estimation and the modal wavefront estimation. This is followed by a brief discussion related to the three important estimation geometries associated with a wavefront estimation process.

## 2.2 Wavefront Sensing

It is well known that a simple photo sensitive detector is not capable of measuring the wavefront directly by measuring the intensity or brightness level of a light beam. However, the wavefront can be measured indirectly, when the sensor is allowed to receive a deformed wavefront (by saying deformed wavefront, we mean the deviation of the wavefront with respect to an ideal or plane wavefront). This deviation causes a change in the focal spot, relative to the focal spot obtained due to a plane wavefront. The change may be in the intensity level of the focal spot, shape of the focal spot, shift in the centroid of the focal spots, etc. All these variations of the focal spot on the detector plane, are directly linked to the deformed wavefront, which can be analyzed further to estimate the incident wavefront. Based on these indirect approaches, the wavefront sensors are broadly classified into interferometric sensors and geometric sensors [11, 31]. As the name suggests, the interferometric sensor works based on the phenomenon of interference of light beam. The incident wavefront can be estimated by recording and analysing the interference pattern formed due to superposition of various portions of the incident wavefront. The most commonly used interferometric sensors are the lateral shearing interferometers [32], Twyman-Green interferometers [33], etc. The geometric sensors on the other hand use geometrical optics approximations for light propagation. Here, the incident wavefront can be estimated from a linear relationship between wavefront slope and focal spot location or intensity variation in the image plane. The Shack Hartmann Wavefront Sensor (SHWS) [25], Curvature Wavefront Sensor (CWS) [34], etc., are some important types of geometric sensors. Both the geometric sensors and interferometric sensors have their respective advantages and limitations. However, the geometric sensors are considered to be more robust than the interferometric sensors [11] for the type of applications mentioned in chapter 1. The geometric wavefront sensors, again, depending on the type of measurement are sub-divided into zonal wavefront sensor and modal wavefront sensor [12].

## 2.3 Zonal Wavefront Sensing

Zonal wavefront sensing refers to the process where an incident beam is expressed locally over a finite number of discrete zones or small spatial areas as shown in Fig. 2.1. Wavefront slope information of each zone is measured initially and the profile of the entire incident beam is then obtained by combining the information of local slopes from each of the zones.

### 2.3.1 Shack Hartmann Wavefront Sensor

The Shack Hartmann wavefront sensor is one of the popular zonal wavefront sensors. It is a modified version of the original Hartmann wavefront sensor developed in 1904 by J. Hartmann [18, 25, 35, 36]. The primary objective of the development of

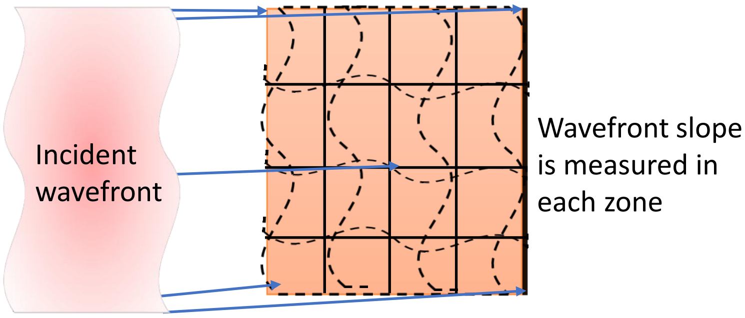

**Figure 2.1:** Dividing a wavefront into discrete zones.

Hartmann sensor was to carry out optical metrology of large optical elements like mirrors, lenses, etc. The Hartmann sensor consists of an opaque plate, with an array of holes (each of these holes acts like an aperture), as shown in Fig. 2.2 and a photographic film as the detector. In the figure, a plate, known as the Hartmann plate, containing a series of small apertures is illuminated with a light source that is placed in front of a test mirror. The incident rays pass through the apertures to fall on the mirror. Again, the reflected rays from the mirror pass through the apertures to be finally recorded on a photographic plate giving rise to a pattern of spots. The position of the spots in the photographic plate is an indication of the tilt of the local wavefront at each hole which in turn describes the optics quality of the mirror. This technique is known as the Hartmann test. However, there are certain disadvantages associated with this technique, such as an inherently lower spatial resolution and very low light gathering efficiency of the arrangement. Additionally, there exist some disturbing diffraction effects due to the presence of an array of holes.

In 1971, Roland Shack suggested the use of a lens array instead of the array of holes. The improved version of the sensor is known as the Shack Hartmann wavefront sensor (SHWS) [25]. Modern SHWS consists of a two dimensional array of micro-lenses, called lenslets, followed by a detector. The SHWS works almost in a similar way as that of the Hartmann sensor. However, now the incident wavefront is allowed to pass through the lenslets array and the resulting spots are captured on the detector. It is to be noted, that the spots obtained in the case of SHWS for a specific diameter lenslets are smaller in size, in comparison to those obtained from the same diameter apertures of the Hartmann sensor.

Figure 2.3 illustrates the working principle of the SHWS. The array of lenslets of the SHWS samples an incident beam of light to form an array of focal spots having the same dimension as that of the lenslets array dimension. For a plane unaberrated

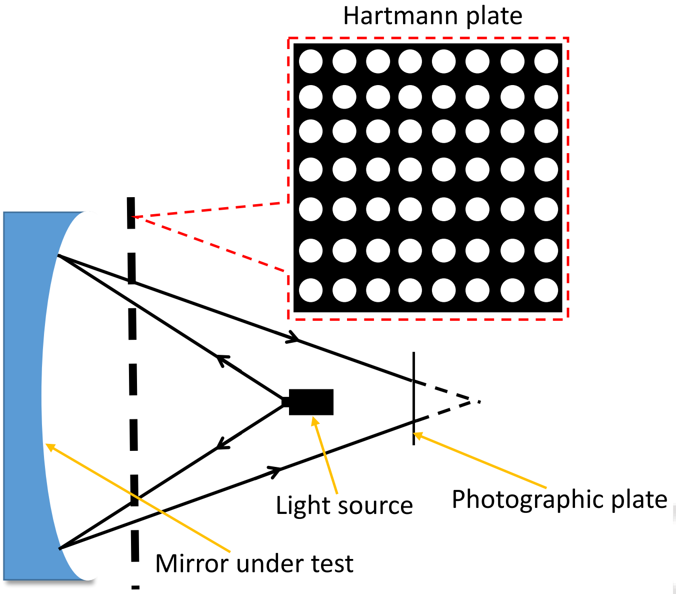

**Figure 2.2:** Schematic diagram of a Hartmann Sensor.

wavefront denoted by $U_1U_2$, the focal spots are formed along the optical axis of each lenslet. This results in a regularly spaced grid of spots (referred to as the reference positions) denoted by the white filled circles as shown in Fig. 2.3(a). The focal spots are captured by placing a detector at the focal plane such that each of the focal spots lie within its detector subaperture corresponding to each of the lenslets aperture. Each of the focal spots lie at the centre of its corresponding detector subaperture if a wavefront like $U_1U_2$ is incident. However, if the incident wavefront has some deformation as indicated by $A_1A_2$, there will be a shift in the spots (referred to as the shifted positions) with respect to the corresponding reference positions. Such spots are represented by the red filled circles, shown in Fig. 2.3(b). The amount of shift in the focal spots is proportional to the tilt of the wavefront portion across each lenslet aperture. Thus, the shifts of the focal spots contain information of the local wavefront slopes of the incoming deformed wavefront. The incident wavefront can be estimated from a measurement of the local wavefront slopes. Thus, wavefront sensing and wavefront estimation in the case of the SHWS can be performed in two steps. In the first step, the focal spot centroid positions corresponding to reference positions and shifted positions are obtained. The local slopes ($S^x$, $S^y$) of the wavefront are subsequently determined by calculating the focal spot shifts along the horizontal and vertical directions. In the second step, these local slope information from each of the sampled wavefront are combined to obtain the entire profile of the incident beam, by following a wavefront estimation algorithm.

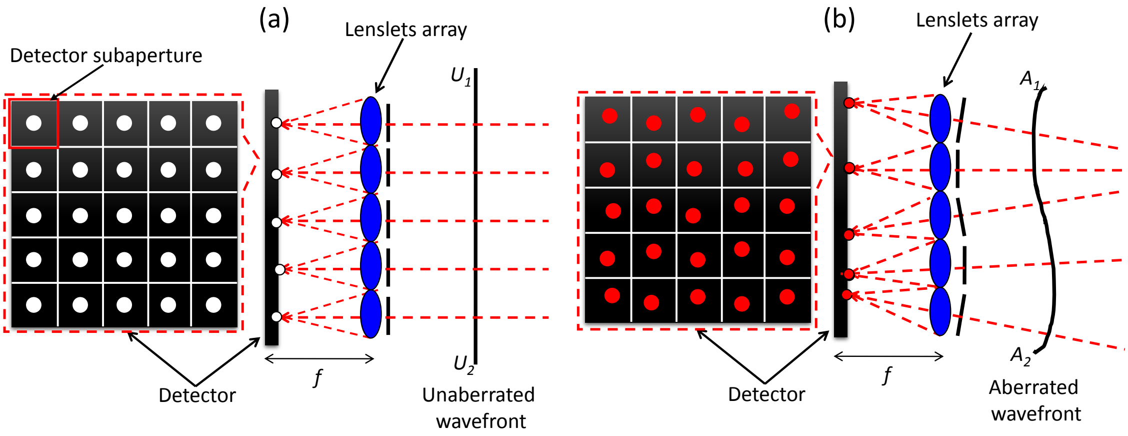

**Figure 2.3:** Schematic diagram of a Shack-Hartmann Wavefront Sensor.

A centroid calculation is carried out within each detector subaperture to determine the centre of mass of each of the focal spot [37]. In Fig. 2.4, let $AC$ represents a portion of an incident wavefront tilted by an angle $\theta$ with respect to the plane wavefront portion $AB$, across a lens subaperture. This tilt of the wavefront portion gets translated into a shift of the focal spot, from point $Q$ to $P$, in the plane of the detector. The black and red circles indicate the reference positions and shifted positions of the focal spots, respectively. If $(X_r, Y_r)$ and $(X_s, Y_s)$ represent the $(x, y)$ centroid location of the reference array of focal spots and the shifted array of focal spots, respectively, then we get

$$\begin{bmatrix} X_r \\ Y_r \end{bmatrix} = \begin{bmatrix} \frac{\sum_{i,j} x_{i,j} I_{i,j}}{\sum_{i,j} I_{i,j}} \\ \frac{\sum_{i,j} y_{i,j} I_{i,j}}{\sum_{i,j} I_{i,j}} \end{bmatrix} \tag{2.1}$$

$$\begin{bmatrix} X_s \\ Y_s \end{bmatrix} = \begin{bmatrix} \frac{\sum_{i,j} x'_{i,j} I_{i,j}}{\sum_{i,j} I_{i,j}} \\ \frac{\sum_{i,j} y'_{i,j} I_{i,j}}{\sum_{i,j} I_{i,j}} \end{bmatrix} \tag{2.2}$$

where $(i, j)$ represents the row and column indices with values from 1 to the size (in number of pixels) of a single detector subaperture area. $I_{i,j}$ denotes the focal spot intensities on the detector subaperture and $(x_{i,j}, y_{i,j})$, $(x'_{i,j}, y'_{i,j})$ denote the reference focal spot co-ordinates and shifted focal spot co-ordinates, respectively. By measuring the displacements of the focal spot centroid positions in the horizontal direction and vertical direction, an array of x-slopes and an array of y-slopes, denoted by $S^x$ and $S^y$ respectively, are obtained. The slope values, $S^x$ and $S^y$ are related to the phase $\phi(x, y)$ as

$$\begin{bmatrix} S^x(i,j) \\ S^y(i,j) \end{bmatrix} = \begin{bmatrix} \frac{\partial\phi(x,y)}{\partial x} \\ \frac{\partial\phi(x,y)}{\partial y} \end{bmatrix} \approx \frac{1}{f} \begin{bmatrix} X_s - X_r \\ Y_s - Y_r \end{bmatrix} \tag{2.3}$$

where $X_s - X_r = \Delta x$, $Y_s - Y_r = \Delta y$ and $f$ is the focal length of the SHWS lenslet.

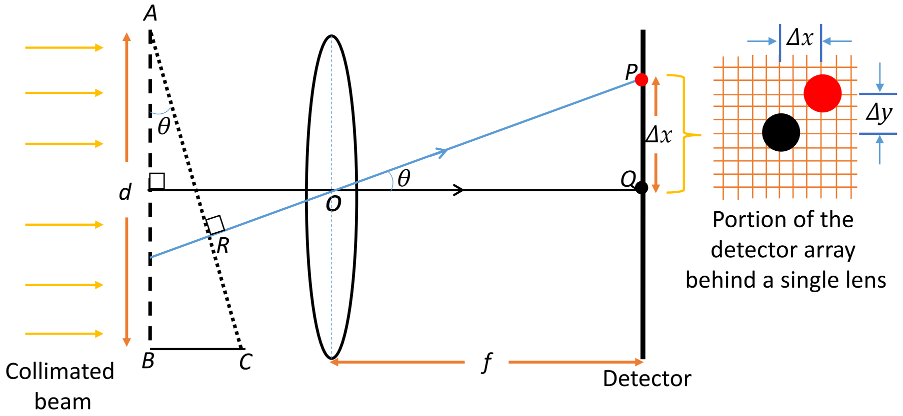

**Figure 2.4:** Shift in the focal spot centroid due to a slope in the incident wavefront.

## 2.4 Modal Wavefront Sensing

Modal wavefront sensing is referred to the process where an incident beam phase profile is expressed in terms of some orthogonal basis functions as shown in Fig. 2.5. The entire incident beam information is collected globally in terms of intensity distribution variation in the image plane, which are further analyzed to extract the information regarding the wavefront.

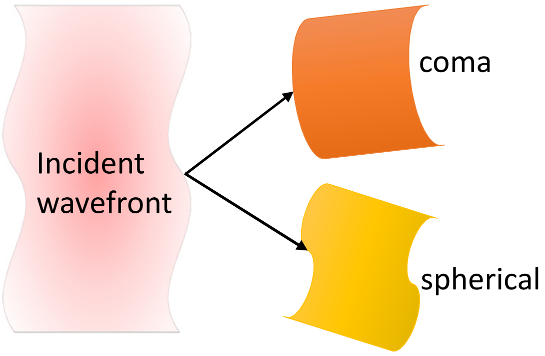

**Figure 2.5:** Decomposition of a wavefront into its constituent orthogonal modes.

### 2.4.1 Curvature Wavefront Sensor

Curvature wavefront sensor (CWS) is one of the popular modal wavefront sensors which was proposed by Roddier in 1988 [34, 38]. Unlike in the case of SHWS, it measures the wavefront curvature instead of wavefront slopes. The wavefront curvature is extracted by taking the second derivative of the wavefront slopes. It measures the image of the beam at two locations, when it is within the focus, referred to as intra-focal image and when it is outside the focus, referred to as extra-focal image as shown in Fig. 2.6. The CWS is based on the principle that a plane incident wavefront should result in equal intensities at both locations at equal distances from the focus. Thus, if there exists an intensity difference between intra-focal plane and extra-focal plane, it is due to a curvature present in the wavefront. Thus, the difference in the intensities in the two images gives a measure of the incident wavefront curvature (i.e., its second derivative).

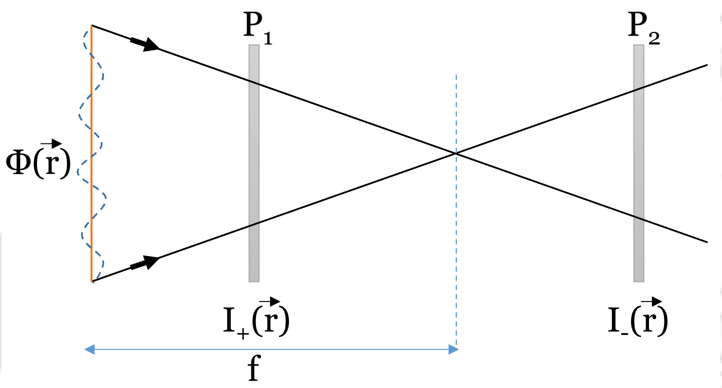

**Figure 2.6:** Schematic diagram of a curvature wavefront sensor.

Let $I_1$ and $I_2$ be the intensity distributions due to a wavefront curvature, produced at a distance $l$, before the focal plane (say in plane $P_1$) and after the focal plane (say in plane $P_2$), respectively. Using geometrical optics approximation, the normalized difference between the two intensity distributions in terms of the phase $\phi$ is given [34, 36] as

$$\frac{I_2(r) - I_1(r)}{I_2(r) + I_1(r)} = \frac{f(f-l)}{2l}\left[\frac{\partial \phi}{\partial n} + P\nabla^2\phi\right] \tag{2.4}$$

where, $P$ is the transmission function of the aperture, $\nabla^2$ is the Laplacian operator, $\frac{\partial \phi}{\partial n}$ is the first derivative of the wavefront normal to the boundary and $f$ is the focal length of the lens. Equation 2.4 is known as the intensity transport equation which can be solved to obtain the wavefront from the intensity information. The spatial resolution can be enhanced by increasing the distance $l$, although this adversely affects the sensitivity. On the other hand, a smaller distance yields a higher sensitivity to low order wavefront deformations.

Both the SHWS and CWS have their own advantages as well as disadvantages. In a CWS, the orthogonality requirement of the basis functions over the sampling geometry is a major concern. Also, its performance is limited due to the fact that highly deformed wavefronts cannot be accurately represented by a Zernike basis (or any other basis function) for a fixed number of measured values. In contrary to the CWS, orthogonality requirement in the case of SHWS is not a must and its performance in the case of a highly deformed wavefront is quite reliable. This makes SHWS, the most widely used zonal wavefront sensor and holds ground due to its robust and easily implementable nature.

## 2.5 Wavefront Estimation

Wavefront estimation may be regarded as the processing of the data that is collected during wavefront sensing. Here, we discuss wavefront estimation related to a Shack Hartmann type wavefront sensor only. Once the slope measurements are available, a mathematical relationship is established that relates the unknown phase value $\phi$ with the measured slope values, $S^x$ and $S^y$. But this mathematical relationship between the phase and the measured slopes can be obtained only through certain estimation geometries. There are three basic estimation geometries available so far. The three estimation geometries and the corresponding estimation algorithms were proposed by Hudgin [19], Fried [20], and Southwell [12]. In this thesis, estimation geometry refers to the geometrical arrangement and the estimation algorithm refers to the set of equations, associated with the estimation process. It is to be mentioned that the Southwell geometry is mostly preferred for SHWS as the location of the lenslets array best matches the respective geometrical arrangement. The wavefront estimation process on the other hand, can be sub-divided into two categories [12, 39], namely, the zonal estimation and the modal estimation, depending on the procedure followed to estimate the wavefront. Although, both the methods of estimation have their own strength and limitation, it is possible to convert from one estimation method to the other, as they represent the same wavefront [39]. However, due to the complexity involved, such a process of conversion between the two estimation process is not preferred.

## 2.6 Zonal Wavefront Estimation

In the zonal wavefront estimation, the whole wavefront is described locally over a finite number of zones (say $N$ number of zones) [12, 39]. The number of zones is basically the number of lenslets used in the SHWS to sample the incident wavefront. The zones may constitute a regular grid of square, rectangle, hexagon, etc. Usually the grid structure is chosen to suit the target area under observation. The incident wavefront which is usually continuous in nature is discretized by the $N$ lenslets array and focused onto $N$ discrete phase points, known as grid points. Thus, the entire wavefront can only be exactly represented if $N$ approaches infinity.

Zonal slope based wavefront estimation can be performed by primarily two approaches, namely, the least square based method [23, 40] and the Fourier transform method [41, 42]. However, further analysis of the above two methods reveal that the least square based iterative method in addition to being flexible, increases the estimation accuracy [43, 44]. The least square based estimation method can be performed either by matrix iterative method or by matrix inversion method [12].

### 2.6.1 Matrix Iterative Method

Here, we first provide a short discussion on the three important wavefront estimation geometries and the respective algorithms. Figure 2.7 shows a representation of the three geometries. The horizontal and vertical arrows indicate the x-slope and y-slope sampling positions, and the dots indicate the estimated phase points.

In the Hudgin geometry [19], i.e., in Fig. 2.7(a), the wavefront slopes are measured at the mid point between two neighboring grid points. Here, the slope measurements along $x$ and $y$ directions do not overlap. Thus, if $\phi(i,j)$, $S^x(i,j)$ and $S^y(i,j)$ represent the phase, the horizontal slope and the vertical slope, respectively, at the location $(i,j)$, then the relation between phase and measured slopes can be written as,

$$\left.\begin{aligned} S^x(i,j) &= \frac{\phi(i,j+1)-\phi(i,j)}{d} \\ S^y(i,j) &= \frac{\phi(i,j+1)-\phi(i,j)}{d} \end{aligned}\right\} \tag{2.5}$$

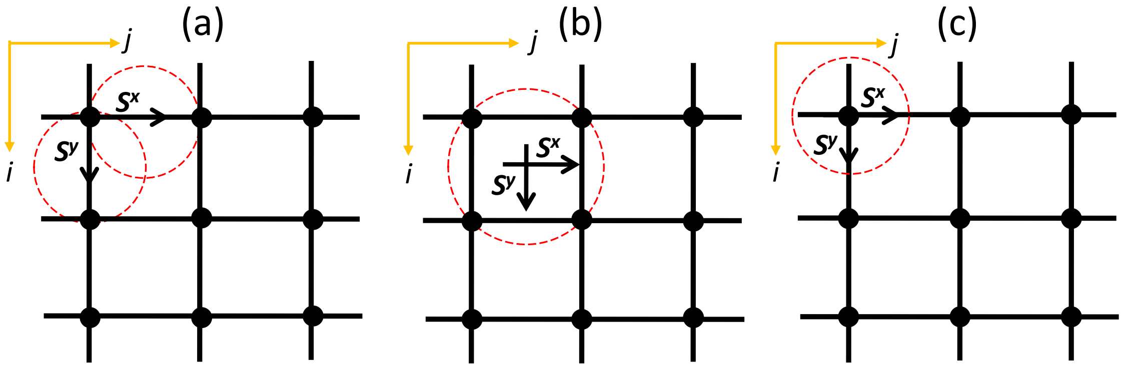

**Figure 2.7:** (a) Zonal wavefront estimation geometry of (a) Hudgin, (b) Fried and (c) Southwell. The horizontal and vertical arrows indicate x-slope and y-slope sampling positions and the dots are estimated phase points.

Therefore, considering 4 neighboring grid points, namely $(i, j+1)$, $(i, j-1)$, $(i+1, j)$ and $(i-1, j)$, we get,

$$\phi(i,j) = \begin{cases} \phi(i,j+1) - dS^x(i,j) \\ \phi(i,j-1) + dS^x(i,j-1) \\ \phi(i+1,j) - dS^y(i,j) \\ \phi(i-1,j) + dS^y(i-1,j) \end{cases} \tag{2.6}$$

Here $d$ is the separation between two adjacent grid points in the vertical or horizontal direction. Adding all the relations of Eq. 2.6, we get

$$\begin{aligned} \phi(i,j) \quad &= \frac{\phi(i,j+1) + \phi(i,j-1) + \phi(i+1,j) + \phi(i-1,j)}{4} \\ &+ \frac{d}{4}[S^x(i,j-1) - S^x(i,j) + S^y(i-1,j) - S^y(i,j)] \end{aligned} \tag{2.7}$$

Equation 2.7 gives an estimation of the phase value at the location $(i, j)$ using Hudgin geometry.

In the Fried geometry [20], i.e., in Fig. 2.7(b), both the x-slopes and y-slopes are measured at the point $(i, j)$ as an average of the phase differences along its two parallel borders in the x-direction or in the y-direction. Here, both the x-slopes and y-slopes are measured at the same point and the grid for wavefront slope measurements and the phase points to be estimated are separated by a distance of $d/2$, both in the $x$ and $y$ directions. Thus, in the Fried geometry, the relation between phase and measured slopes can be written as,

$$\left.\begin{aligned} S^x(i,j) &= \frac{[\frac{\phi(i,j+1)+\phi(i+1,j+1)}{2} - \frac{\phi(i,j)+\phi(i+1,j)}{2}]}{d} \\ S^x(i,j) &= \frac{[\frac{\phi(i+1,j)+\phi(i+1,j+1)}{2} - \frac{\phi(i,j)+\phi(i,j+1)}{2}]}{d} \end{aligned}\right\} \tag{2.8}$$

Considering 4 neighboring grid points, namely $(i, j+1)$, $(i, j-1)$, $(i+1, j)$ and $(i-1, j)$, we get,

$$\phi(i,j) = \begin{cases} \phi(i,j+1) + \phi(i+1,j+1) - \phi(i+1,j) - 2dS^x(i+\frac{1}{2}, j+\frac{1}{2}) \\ \phi(i+1,j) + \phi(i+1,j+1) - \phi(i,j+1) - 2dS^y(i+\frac{1}{2}, j+\frac{1}{2}) \\ \phi(i,j-1) + \phi(i+1,j-1) - \phi(i+1,j) + 2dS^x(i+\frac{1}{2}, j-\frac{1}{2}) \\ \phi(i+1,j-1) + \phi(i+1,j) - \phi(i,j-1) - 2dS^y(i+\frac{1}{2}, j-\frac{1}{2}) \\ \phi(i-1,j+1) + \phi(i,j+1) - \phi(i-1,j) - 2dS^x(i-\frac{1}{2}, j+\frac{1}{2}) \\ \phi(i-1,j) + \phi(i-1,j+1) - \phi(i,j+1) + 2dS^y(i-\frac{1}{2}, j+\frac{1}{2}) \\ \phi(i-1,j-1) + \phi(i,j-1) - \phi(i-1,j) + 2dS^x(i-\frac{1}{2}, j-\frac{1}{2}) \\ \phi(i-1,j-1) + \phi(i-1,j) - \phi(i,j-1) + 2dS^y(i-\frac{1}{2}, j-\frac{1}{2}) \end{cases} \tag{2.9}$$

Adding all the relations of Eq. 2.9, we get

$$\begin{aligned} \phi(i,j) \quad = \quad & \frac{[\phi(i+1,j-1) + \phi(i+1,j+1) + \phi(i-1,j+1) + \phi(i-1,j-1)]}{4} + \\ & \frac{d}{4}[-S^x(i+\frac{1}{2}, j+\frac{1}{2}) - S^y(i+\frac{1}{2}, j+\frac{1}{2}) + S^x(i+\frac{1}{2}, j-\frac{1}{2}) \\ & -S^y(i+\frac{1}{2}, j-\frac{1}{2}) - S^x(i-\frac{1}{2}, j+\frac{1}{2}) + S^y(i-\frac{1}{2}, j+\frac{1}{2}) \\ & +S^x(i-\frac{1}{2}, j-\frac{1}{2}) + S^y(i-\frac{1}{2}, j-\frac{1}{2})] \end{aligned} \tag{2.10}$$

Equation 2.10 gives an estimation of the phase value at the location $(i, j)$ using Fried geometry.

In the case of Southwell geometry [12], as shown in Fig. 2.7(c), the mean horizontal (or vertical) slope at an intermediate point between two adjacent grid points in the horizontal (or vertical) direction is expressed in terms of the phase difference at the two adjacent grid points in the horizontal (or vertical) direction. Here, the x-slope measurement coincide with the y-slope measurement, and both the slope measurements take place at the same point where the phase is required to be estimated. The estimation algorithm relating the phase and slope values may be written as

$$\left.\begin{aligned}\frac{[S^x(i,j+1)+S^x(i,j)]}{2}=\frac{[\phi(i,j+1)-\phi(i,j)]}{d}\\ \frac{[S^y(i+1,j)+S^y(i,j)]}{2}=\frac{[\phi(i+1,j)-\phi(i,j)]}{d}\end{aligned}\right\} \tag{2.11}$$

Considering 4 neighboring grid points, namely $(i,j+1)$, $(i,j-1)$, $(i+1,j)$ and $(i-1,j)$, we get,

$$\phi(i,j)=\begin{cases}\phi(i,j+1)-\frac{d}{2}[S^x(i,j)+S^x(i,j+1)]\\ \phi(i,j-1)+\frac{d}{2}[S^x(i,j)+S^x(i,j-1)]\\ \phi(i+1,j)-\frac{d}{2}[S^y(i,j)+S^y(i+1,j)]\\ \phi(i-1,j)+\frac{d}{2}[S^y(i,j)+S^y(i-1,j)]\end{cases} \tag{2.12}$$

Adding all the relations of Eq. 2.12, we get

$$\begin{aligned}\phi(i,j) &= \frac{\phi(i-1,j)+\phi(i,j-1)+\phi(i+1,j)+\phi(i,j+1)}{4}\\ &+\frac{d}{8}[S^x(i,j-1)-S^x(i,j+1)+S^y(i-1,j)-S^y(i+1,j)]\end{aligned} \tag{2.13}$$

Equation 2.13 gives an estimation of the phase value at the location $(i,j)$ using Southwell geometry. For all the geometries, the phase at the grid point $(i,j)$, given by Eq. 2.7, Eq. 2.10 and Eq. 2.13 can be estimated by performing a matrix iterative operation. Some important iterative methods used for phase estimation are Jacobi, Gauss-Seidel, Successive Over Relaxation, etc [12]. The implementation of matrix iterative method to estimate a wavefront in a zonal wavefront estimation process can be found in the works of M. li et al. [Appl. Opt., 56 (2017)], P. H. Phuc et al. [J. Korean Phys. Soc., 70 (2017)], etc.

### 2.6.2 Matrix Inversion Method

In all the geometries discussed above, it is possible to stack the slopes in a matrix $S$ and the unknown phase values in another matrix $\phi$. Then a compact linear matrix relationship between $S$ and $\phi$ can be established to facilitate the application of matrix inversion technique [12, 21]. The above matrix formalism can be better understood by considering the Southwell algorithm for a $3\times 3$ (say) grid dimension, such that

$$\left.\begin{array}{l} \dfrac{[S^x(i,j+1)+S^x(i,j)]}{2} = \dfrac{[\phi(i,j+1)-\phi(i,j)]}{d} (\text{for i} = 1,\ 3;\ \text{j} = 1,\ 2) \\ \dfrac{[S^y(i+1,j)+S^y(i,j)]}{2} = \dfrac{[\phi(i+1,j)-\phi(i,j)]}{d} (\text{for i} = 1,\ 2;\ \text{j} = 1,\ 3) \end{array}\right\} \tag{2.14}$$

The LHS of the above equation is

$$\begin{bmatrix}
0.5 & 0.5 & 0 & 0 & 0 & 0 & 0 & 0 & 0 & 0 & 0 & 0 & 0 & 0 & 0 & 0 & 0 & 0 \\
0 & 0.5 & 0.5 & 0 & 0 & 0 & 0 & 0 & 0 & 0 & 0 & 0 & 0 & 0 & 0 & 0 & 0 & 0 \\
0 & 0 & 0 & 0.5 & 0.5 & 0 & 0 & 0 & 0 & 0 & 0 & 0 & 0 & 0 & 0 & 0 & 0 & 0 \\
0 & 0 & 0 & 0 & 0.5 & 0.5 & 0 & 0 & 0 & 0 & 0 & 0 & 0 & 0 & 0 & 0 & 0 & 0 \\
0 & 0 & 0 & 0 & 0 & 0 & 0.5 & 0.5 & 0 & 0 & 0 & 0 & 0 & 0 & 0 & 0 & 0 & 0 \\
0 & 0 & 0 & 0 & 0 & 0 & 0 & 0.5 & 0.5 & 0 & 0 & 0 & 0 & 0 & 0 & 0 & 0 & 0 \\
0 & 0 & 0 & 0 & 0 & 0 & 0 & 0 & 0 & 0.5 & 0 & 0 & 0.5 & 0 & 0 & 0 & 0 & 0 \\
0 & 0 & 0 & 0 & 0 & 0 & 0 & 0 & 0 & 0 & 0 & 0 & 0.5 & 0 & 0 & 0.5 & 0 & 0 \\
0 & 0 & 0 & 0 & 0 & 0 & 0 & 0 & 0 & 0 & 0.5 & 0 & 0 & 0.5 & 0 & 0 & 0 & 0 \\
0 & 0 & 0 & 0 & 0 & 0 & 0 & 0 & 0 & 0 & 0 & 0 & 0 & 0.5 & 0 & 0 & 0.5 & 0 \\
0 & 0 & 0 & 0 & 0 & 0 & 0 & 0 & 0 & 0 & 0 & 0.5 & 0 & 0 & 0.5 & 0 & 0 & 0 \\
0 & 0 & 0 & 0 & 0 & 0 & 0 & 0 & 0 & 0 & 0 & 0 & 0 & 0 & 0.5 & 0 & 0 & 0.5
\end{bmatrix}
\bullet
\begin{bmatrix}
S^x(1,1) \\ S^x(1,2) \\ . \\ . \\ . \\ S^x(3,2) \\ S^x(3,3) \\ S^y(1,1) \\ S^y(1,2) \\ . \\ . \\ . \\ S^y(3,2) \\ S^y(3,3)
\end{bmatrix}$$

and the RHS of the same is

$$\frac{1}{d}\begin{bmatrix} -1 & 1 & 0 & 0 & 0 & 0 & 0 & 0 & 0 \\ 0 & -1 & 1 & 0 & 0 & 0 & 0 & 0 & 0 \\ 0 & 0 & 0 & -1 & 1 & 0 & 0 & 0 & 0 \\ 0 & 0 & 0 & 0 & -1 & 1 & 0 & 0 & 0 \\ 0 & 0 & 0 & 0 & 0 & 0 & -1 & 1 & 0 \\ 0 & 0 & 0 & 0 & 0 & 0 & 0 & -1 & 1 \\ -1 & 0 & 0 & 1 & 0 & 0 & 0 & 0 & 0 \\ 0 & 0 & 0 & -1 & 0 & 0 & 1 & 0 & 0 \\ 0 & -1 & 0 & 0 & 1 & 0 & 0 & 0 & 0 \\ 0 & 0 & 0 & 0 & -1 & 0 & 0 & 1 & 0 \\ 0 & 0 & -1 & 0 & 0 & 1 & 0 & 0 & 0 \\ 0 & 0 & 0 & 0 & 0 & -1 & 0 & 0 & 1 \end{bmatrix} \bullet \begin{bmatrix} \phi(1,1) \\ \phi(1,2) \\ \phi(1,3) \\ \phi(2,1) \\ \phi(2,2) \\ \phi(2,3) \\ \phi(3,1) \\ \phi(3,2) \\ \phi(3,3) \end{bmatrix}$$

Thus, both the left hand side and the right hand side of Eq. 2.14 can be exactly written for a $3 \times 3$ grid dimension, in the form of matrix as shown above. It is possible to generalize the above matrix form for any $N \times N$ grid dimension. Thus, a general matrix equation can be written as

$$CS = A\phi \tag{2.15}$$

where, $C$ is the sparse rectangular matrix, having a dimension of $2N(N-1) \times 2N^2$, performing the averaging of the slope values, $S$ is the column matrix for slope measurement, having a dimension of $2N^2 \times 1$, $A$ is the rectangular matrix, having a dimension of $2N(N-1) \times N^2$, performing the phase difference measurements and $\phi$ is a column matrix, having a dimension of $N^2 \times 1$, containing the phase values to be estimated. Now, Eq. 2.15 is multiplied by the transpose of the matrix $A$ (i.e.,$A^T$) to convert the product $A^TA$ into a square matrix, so that

$$A^TCS = A^TA\phi \tag{2.16}$$

Therefore,

$$\phi = (A^TA)^{-1}A^TCS \tag{2.17}$$

However, for most practical situations, there is a possibility that $A^TA$ is not invertible, as it may be singular.

In order to address such a problem, Eq. 2.15 can be solved using Singular Value Decomposition (SVD) method [45, 46, 47] which facilitates computing the pseudo-inverse of a matrix, instead of obtaining the simple matrix inverse [48]. The pseudo-inverse is an alternative way to solve linear least square problem. A generalized inverse or pseudo-inverse of a matrix $A$ is a matrix that has some properties of the inverse of $A$ but not necessarily all of the properties. Usually, there exists the pseudo-inverse for any arbitrary matrix. However, for a matrix having an inverse, the pseudo-inverse and the inverse are the same.

Calculation of SVD is based on a linear algebra theorem [48] which states that a rectangular matrix $A$ can be factorized into the product of three matrices - an orthogonal matrix $U$, a diagonal matrix $D$ and the transpose of an orthogonal matrix $V$, such that

$$A = UDV^T \tag{2.18}$$

where $U$ is an orthogonal $m \times m$ matrix, satisfying $U^TU = I$ and where the columns of $U$ are the eigenvectors of $AA^T$. Similarly, $V$ is an orthogonal $n \times n$ matrix, such that $V^TV = I$ and the columns of $V$ are the eigenvectors of $A^TA$. The matrix $D$ is a diagonal matrix containing singular values and has the same size as $A$. The singular values in $D$ are the square roots of eigenvalues (say, $\lambda$) from $AA^T$ or $A^TA$, denoted as $\sqrt{\lambda_1}$, $\sqrt{\lambda_2}$, $\cdots$, $\sqrt{\lambda_N}$, which are the diagonal entries of the $D$ matrix, arranged in the descending order. The singular values are always real numbers. If the matrix $A$ is a real matrix, then $U$ and $V$ are also real. To solve Eq. 2.14 using SVD, we consider the pseudo-inverse of matrix $A$, given by Eq. 2.18, as

$$A^+ = VD^{-1}U^T \tag{2.19}$$

$$A^+ = V \begin{bmatrix} \frac{1}{\sqrt{\lambda_1}} & . & \cdots & . \\ . & \frac{1}{\sqrt{\lambda_2}} & \cdots & . \\ \vdots & \vdots & \ddots & \vdots \\ . & . & \cdots & \frac{1}{\sqrt{\lambda_N}} \end{bmatrix} U^T$$

Now, from Eq. 2.15 we get

$$CS = A\phi$$

With

$$\phi = A^{+}CS$$

such that

$$\phi = VD^{-1}U^{T}CS \tag{2.20}$$

Hence, Eq. 2.20 gives the required solution using matrix inversion method. The use of matrix inversion method to estimate the wavefront in a zonal wavefront estimation process can be found in the works of W. Zou et al. [Appl. Opt., 39 (2000)], B. R. Hunt [J. Opt. Soc. Am., 69 (1979)], etc.

## 2.7 Modal Wavefront Estimation

The other approach for wavefront estimation is the modal estimation method [12, 49]. It is known as modal estimation as the entire wavefront is described in terms of a set of smoothly varying modes of an orthogonal basis function. Modal wavefront estimation uses wavefront slope measurements to fit the co-efficients of the modes of the orthogonal basis functions. Some examples of such basis functions are the Zernike polynomials[50, 51], the Taylor monomials [52, 53], the Fourier series [42, 54], etc. Out of these the Zernike polynomials can represent a balanced combination of Seidel aberrations such that the modes have the minimum variance and are orthogonal over a circular pupil [55, 56]. Hence, they are the appropriate choice to represent the wavefront of light beams in optical systems and thus, find extensive use in wavefront estimation in Shack Hartmann type wavefront sensors. The wavefront of the beam $\phi(x, y)$ containing $M$ modes of Zernike polynomials may be written [12] as

$$\phi(x, y) = \sum_{i=1}^{M} a_i Z_i(x, y) \tag{2.21}$$

Taking derivatives on both sides of Eq. 2.21 with respect to $x$ and $y$, the wavefront slope may be written for the $l^{th}$ of $m$ total sampling points, as

$$\left.\begin{aligned} \left.\frac{\partial\phi(x,y)}{\partial x}\right|_l &= \sum_{i=1}^{M} a_i \left.\frac{\partial Z_i(x,y)}{\partial x}\right|_l \\ \left.\frac{\partial\phi(x,y)}{\partial y}\right|_l &= \sum_{i=1}^{M} a_i \left.\frac{\partial Z_i(x,y)}{\partial y}\right|_l \end{aligned}\right\} \tag{2.22}$$

where $\left(\frac{\partial\phi}{\partial x}, \frac{\partial\phi}{\partial y}\right)_l$ and $\left(\frac{\partial Z}{\partial x}, \frac{\partial Z}{\partial y}\right)_l$ stand for the measured slope values (i.e., $S^x$ and $S^y$) and the partial derivatives of the Zernike polynomials with respect to $x$ and $y$, respectively, at the $l^{th}$ subaperture. The partial derivatives of the Zernike polynomials with respect to $x$ and $y$ are obtained theoretically at the equivalent locations where the x-slopes and y-slopes are measured experimentally. This results in a one-to-one correspondence between the experimentally measured slope values and the theoretically obtained slope values (derivative of Zernike polynomials). It is to be noted that the Zernike polynomials are discretized at as many number of locations as the number of lenslets in the SHWS.

Thus, Eq. 2.22 can be formulated in the matrix form as

$$S = Aa_i \tag{2.23}$$

where $A$ is a rectangular matrix of dimension $2N^2 \times M$ with the first $N^2$ rows corresponding to $\frac{\partial Z_M}{\partial x}$ and the second $N^2$ rows corresponding to the $\frac{\partial Z_M}{\partial y}$. $S$ is a column matrix containing both the measured x-slopes and y-slopes of dimension $2N^2 \times 1$, and $a_i(i \to 1 : M)$ is a column matrix of dimension $N^2 \times 1$ of Zernike co-efficients to be evaluated. Hence,

$$\begin{bmatrix} S^x(1,1) \\ \vdots \\ S^x(M,M) \\ S^y(1,1) \\ \vdots \\ S^y(M,M) \end{bmatrix} = \begin{bmatrix} \frac{\partial Z_1(x,y)_1}{\partial x} & \frac{\partial Z_2(x,y)_1}{\partial x} & \cdots & \frac{\partial Z_M(x,y)_1}{\partial x} \\ \frac{\partial Z_1(x,y)_1}{\partial y} & \frac{\partial Z_2(x,y)_1}{\partial y} & \cdots & \frac{\partial Z_M(x,y)_1}{\partial y} \\ \vdots & \vdots & \ddots & \vdots \\ \frac{\partial Z_1(x,y)_m}{\partial x} & \frac{\partial Z_2(x,y)_m}{\partial x} & \cdots & \frac{\partial Z_M(x,y)_m}{\partial x} \\ \frac{\partial Z_1(x,y)_m}{\partial y} & \frac{\partial Z_2(x,y)_m}{\partial y} & \cdots & \frac{\partial Z_M(x,y)_m}{\partial y} \end{bmatrix} \cdot \begin{bmatrix} a_1 \\ a_2 \\ a_3 \\ \vdots \\ a_M \end{bmatrix}$$

Since $A$ is a rectangular matrix, Eq. 2.23 is multiplied on both sides by the transpose of $A$ (i.e., $A^T$) to get a product which is a square matrix. The co-efficients $a_i$ are then obtained by taking simple matrix inversion, as

$$a_i \quad = \quad (A^T A)^{-1} A^T S \tag{2.24}$$

Due to similar reason stated earlier, SVD method can also be applied to matrix $A$. This results in matrices $U$ and $V$ so that $A = UDV^T$, where $D$ is the diagonal matrix containing the singular values of matrix $A$. Thus, Eq. 2.23 can then be solved using SVD, as

$$a_i \quad = \quad V D^{-1} U^T S \tag{2.25}$$

Equation 2.24 and Eq. 2.25 gives a set of estimated co-efficients by using simple matrix inversion and SVD, respectively. The set of the co-efficients thus obtained are utilized to generate an appropriate linear combination of Zernike modes that approximates the desired wavefront. The implementation of simple matrix inversion and SVD methods to estimate a wavefront in a modal wavefront estimation process can be found in the works of J. Primot et al. [J. Opt. Soc. Am. A, 7 (1990)] and G. Dai [J. Opt. Soc. Am. A, 13 (1996)], respectively.

## 2.8 Conclusion

In this chapter, we have presented a detailed description on wavefront sensing and wavefront estimation processes. This includes the working principles of the Shack Hartmann wavefront sensor and the Curvature wavefront sensor as far as sensing is concerned. Detailed discussion about the two estimation methods, namely, zonal wavefront estimation and modal wavefront estimation has been presented. Also, we have provided a short introduction to the three important geometries associated with the wavefront estimation process. The concepts introduced in this chapter will be relevant to the chapters to be followed in this thesis.

# CHAPTER 3

# Grating Array Based Zonal Wavefront Sensor

## 3.1 Introduction

In this chapter, we provide an introduction to the grating array based zonal wavefront sensor (GAWS) whose working principle is similar to that of the Shack Hartmann wavefront sensor (SHWS). The chapter begins with the mathematical expressions related to the generation of a user defined wavefront and dynamic control of the +1 order focal spot positions, using a computer generated holography technique, which is at the core of the wavefront sensing method. This is followed by a brief discussion on the various components of the experimental arrangement used for the development of the GAWS setup. The working of the GAWS is illustrated using proof-of-principle experimental arrangement. The chapter also presents experimental results for different grating array dimensions that demonstrate the efficient working of the GAWS. As the GAWS facilitates a faster sensor frame rate and reduces the crosstalk along vertical direction, due to its ability to form 1D array of focal spots, such advantages are also discussed.

## 3.2 A Plane Diffraction Grating

A diffraction grating may be considered as a series of finite number of parallel slits giving rise to alternate transparent and opaque slots, spaced equally [57]. Two adjacent transparent and the opaque slots together, is termed as the period of the grating ($d$) such that the spatial frequency of the grating is given by $f_0 = 1/d$. A diffraction grating can be of various types depending on their geometry, material, usage, etc. In this work, we use an amplitude diffraction grating which is primarily of two types, namely, sinusoidal amplitude grating and binary amplitude grating. An amplitude grating is considered sinusoidal, if the amplitude transmittance values vary sinusoidally between a minimum and a maximum value, say between 0 and 1. However, if the amplitude transmittance values are binary in nature, i.e., either 0 or 1, then the amplitude grating is termed as binary amplitude grating. When a plane monochromatic light of wavelength $\lambda$ is incident normally on the diffraction grating, the grating diffracts light into several beams travelling in different directions, each being a diffracted beam of a certain order. When focused by a lens each order gives rise to a diffraction spot. Although different diffraction orders from a diffraction grating pattern are spatially separated, overlapping between adjacent orders may occur. This may happen if a large amount of deformation is present in the incident beam or the fundamental spatial frequency $f_0$ is not sufficiently large. Thus, to separate the diffraction spots from one another, the period of the grating should be sufficiently small.

## 3.3 Sinusoidal Amplitude Grating

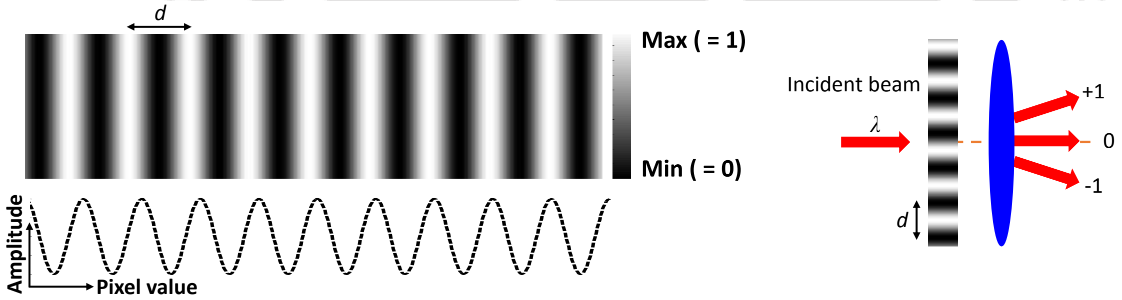

**Figure 3.1:** A sinusoidal diffraction grating pattern and its corresponding amplitude transmittance profile along a line normal to the grating rulings, with $d$ as the grating period. The figure also illustrates the diffraction of light beam into +1, 0 and -1 beams travelling in different directions when a plane monochromatic light beam is normally incident on the diffraction grating.

Let us consider a sinusoidal amplitude grating described using the Cartesian coordinates $(x, y)$ and having a circular aperture. The grating rulings are assumed to be along the $x$-axis, with $f_0$ as the spatial frequency, such that the transmittance function of the sinusoidal grating can be written [58, 59] as

$$g_t(x,y) = \left[\frac{1}{2} + \frac{1}{2}sin(2\pi f_0 x)\right] \tag{3.1}$$

The amplitude transmittance function of the circular aperture of radius $r$ with radial coordinate $\rho$=$\sqrt{x^2+y^2}$ is given by

$$g_a(x,y) = circ(\frac{\rho}{r}) = \begin{cases} 1 & \text{if } \frac{\rho}{r} \leq 1 \\ 0 & \text{if } \frac{\rho}{r} > 1 \end{cases} \tag{3.2}$$

The sinusoidal amplitude grating is lying in front of a lens of focal length $f$ and is illuminated by a plane monochromatic wave with wavelength $\lambda$ and constant amplitude $A$. Thus, the wavefield across the $(x_i, y_i)$ plane, (i.e. the focal plane of the lens), is given [58] by

$$T(x_i,y_i) = \frac{e^{ikf}}{i\lambda f}\int_{-\infty}^{\infty}\int_{-\infty}^{\infty} t(x,y)e^{\frac{-i2\pi}{\lambda f}(xx_i+yy_i)}dx\,dy \tag{3.3}$$

where $e^{ikf}$ is a constant phase delay suffered by all plane wave components travelling between the two parallel planes ($(x,y)$ plane and $(x_i,y_i)$ plane). The double integration in Eq. 3.3 is in fact a 2D Fourier transform (FT) of $g_t(x,y)$ expressed using spatial frequency co-ordinates $f_x = \frac{x_i}{\lambda f}$ and $f_y = \frac{y_i}{\lambda f}$. In other words, the field on the focal plane is the Fourier transform of the field on the grating plane. By using the convolution theorem, Eq. 3.3 can be written as

$$T(x_i,y_i) = \frac{e^{ikf}}{i\lambda f}\mathscr{F}\left[g_t(x,y)\right] * \mathscr{F}\left[g_a(x,y)\right] \tag{3.4}$$

$$T(x_i,y_i) = \frac{e^{ikf}}{i\lambda f}\mathscr{F}\left[\frac{1}{2} + \frac{1}{2}sin(2\pi f_0 x)\right] * \mathscr{F}\left[circ(\frac{\rho}{r})\right] \tag{3.5}$$

where $\mathscr{F}$ and $*$ represents the 2D Fourier transform and convolution operation, respectively. Now, the FT of a Dirac delta function [60] is given by

$$\mathscr{F}\left\{\delta(x)\right\} = \int_{-\infty}^{\infty} \delta(x)e^{-i2\pi f_x x}dx \tag{3.6}$$

From the definition of Dirac delta function and using $f(x) = e^{-i2\pi f_x x}$, we have

$$\int_{-\infty}^{\infty} \delta(x) f(x) dx = f(0) = 1 \tag{3.7}$$

Again from the Shifting property, we have

$$\mathscr{F}\Big\{\delta(x - f_0)\Big\} = e^{-i2\pi f_x f_0} \tag{3.8}$$

Since, FT is a linear operation and if we consider two Dirac delta functions located at $\pm f_0$, then from Eq. 3.8, we get

$$\mathscr{F}\Big\{\delta(x - f_0) - \delta(x + f_0)\Big\} = e^{-i2\pi f_x f_0} - e^{i2\pi f_x f_0} = -2isin(2\pi f_x f_0) \tag{3.9}$$

Therefore,

$$\mathscr{F}\Big\{sin(2\pi f_0 x)\Big\} = \frac{1}{2i}\Big\{\delta(f_x - f_0) - \delta(f_x + f_0)\Big\} \tag{3.10}$$

and

$$\mathscr{F}\left\{\frac{1}{2} + \frac{1}{2}sin(2\pi f_0 x)\right\} = \frac{1}{2}\left[\delta(f_x, f_y) + \frac{1}{2i}\Big\{\delta(f_x - f_0, f_y) - \delta(f_x + f_0, f_y)\Big\}\right] \tag{3.11}$$

On the other hand, the 2D Fourier transform of a circular aperture of radius $r$, is related to the Bessel function of the first kind [58], such that,

$$\mathscr{F}\left\{circ(\frac{\rho}{r})\right\} = \pi r^2 A_r(f_x, f_y) \tag{3.12}$$

where $A_r = \frac{J_1(2\pi r\sqrt{f_x^2+f_y^2})}{\pi r\sqrt{f_x^2+f_y^2}}$, $J_1$ being the Bessel function of first kind. Using Eq. 3.11 and Eq. 3.12, in Eq. 3.5, we have

$$T(x_i, y_i) = \frac{\pi r^2 e^{ikf}}{i2\lambda f}\left[A_r(f_x, f_y) + \frac{1}{2i}\Big\{A_r(f_x - f_0, f_y) - A_r(f_x + f_0, f_y)\Big\}\right] \tag{3.13}$$

Now, in the most general case when the grating rulings make an angle with the $x$-axis, such that $f_0^2 = f_{0x}^2 + f_{0y}^2$ (where $(f_{0x}, f_{0y})$ are the spatial frequencies of the grating along the x-axis and y-axis), one can write Eq. 3.13 as

$$T(x_i, y_i) = \frac{\pi r^2 e^{ikf}}{i2\lambda f}\left[A_r(f_x, f_y) + \frac{1}{2i}\Big\{A_r(f_x - f_{0x}, f_y - f_{0y}) - A_r(f_x + f_{0x}, f_y + f_{0y})\Big\}\right] \tag{3.14}$$

In Eq. 3.14, the first term on the right hand side corresponds to the undiffracted 0 order beam, while the second and third terms correspond to the ±1 diffracted orders. Figure 3.1 shows a sinusoidal amplitude diffraction grating pattern and its corresponding amplitude transmittance profile along a line drawn normal to the grating rulings. It also illustrates the formation of +1, 0 and -1 diffracted beams when a plane monochromatic light beam of wavelength $\lambda$ is incident normally on the diffraction grating. It is clear that the separation of the ±1 diffracted order focal spots (with respect to the zero order focal spot) is a function of the spatial frequencies $(f_{0x}, f_{0y})$ corresponding to the sinusoidal amplitude grating. Further, the ±1 diffracted orders can be used to define any desired phase profile using a computer generated holography technique, which is discussed in the following section.

## 3.4 Computer Generated Holography

A conventional hologram is a record of the interference pattern formed by the superposition of two mutually coherent light beams (one beam is known as the reference beam and the other beam reflected by the object, is known as the object beam) [61]. When the hologram is illuminated by only the reference beam, the diffraction pattern recreates the wavefronts of light beam reflected by the original object. Thus, one may create a 3D image of the object via the reconstruction of the object beam wavefront. Hungarian Physicist, Denis Gabor [62] is regarded as the pioneer of this technique. The holography technique has proved to be a phenomenal invention due to its wide range of applications in various fields cutting across disciplines. However, in the present days it is also possible to synthesize holograms by employing computer controlled mathematical algorithms or graphical descriptions without the need of actual interference between the two beams. This particular technique is referred to as digital holography or computer generated holography (CGH) which was introduced by B. R. Brown and A. Lohmann [63, 64]. The CGH technique, thus provides one with an opportunity of generating an object beam without the presence of the physical object. The implementation of the CGH involves a series of steps which include mathematical representation of the object beam and reference beam, computation of the interference pattern (due to the superposition between the reference beam and the object beam) and finally writing of the pattern onto a mask or diffractive optical element (like spatial light modulator). Realisation of a sinusoidal amplitude grating or a hologram, requires capability to perform a gray scale modulation of the amplitude of the incident beam. However, light modulating devices are often inefficient in performing a perfect gray scale amplitude modulation, while they can efficiently perform a binary amplitude modulation. Thus, the binarised versions of the sinusoidal grating or hologram can be more efficiently and accurately realised. In this thesis we will employ a binary hologram based CGH technique to generate a user defined wavefront which can be dynamically reconfigured using a computer interface. Dynamic control of the wavefront is made possible by the use of a programmable LCSLM to implement the CGH technique. Below we provide a brief discussion on the CGH scheme [29, 30] implemented in this thesis.

## 3.5 Generation of User Defined Wavefront

By using the principle of computer generated holography, a user defined wavefront can be generated [29, 30]. Let, us represent the complex amplitude of the object beam, with unit amplitude as

$$A(x, y) = \mathrm{e}^{[i\{\phi(x,y)+\tau(x,y)\}]} \tag{3.15}$$

Here, $\phi(x, y)$ represents the desired phase function and $\tau(x, y)$ represents a linear tilt function. The tilt function, $\tau(x, y) = f_{0x}x + f_{0y}y$, represents the amount of deflection of the desired beam with respect to the undiffracted zero order beam. The amount of deflection of the desired beam along the horizontal direction and the vertical direction is described by the values of the spatial frequencies, $f_{0x}$ and $f_{0y}$, respectively. Thus, the tilt function, may also be referred to as spatial frequency function. The algorithm defining the transmittance function, $g_t(x, y)$ of the binary hologram to generate the object beam, is given as

$$g_t(x, y) = \begin{cases} 1 & \text{if } \cos[\phi(x, y) + \tau(x, y)] \geq 0 \\ 0 & \text{if } \cos[\phi(x, y) + \tau(x, y)] < 0 \end{cases} \tag{3.16}$$

When a collimated laser beam having unit amplitude is incident on the binary hologram, the complex amplitude profile just after the hologram plane is in fact given by the transmittance function $g_t(x, y)$. The light diffracted by the hologram, when focused by a lens, results in the formation of diffraction spots corresponding to various diffraction orders. The appearance of diffraction orders after the hologram can be explained by performing a Fourier series expansion of the transmittance function of the grating. The Fourier expansion of $g_t(x,y)$ can be written as

$$g_t(x,y)=\frac{1}{2}+\frac{1}{\pi}\left[\begin{array}{l}\left\{e^{i(\phi+\tau)}+e^{-i(\phi+\tau)}\right\}-\frac{1}{3}\left\{e^{i3(\phi+\tau)}+e^{-i3(\phi+\tau)}\right\}\\ +\frac{1}{5}\left\{e^{i5(\phi+\tau)}+e^{-i5(\phi+\tau)}\right\}-\cdots\end{array}\right] \tag{3.17}$$

The first term of Eq. 3.17 corresponds to the undiffracted 0 order beam while the second and the third terms correspond to the ± 1 orders carrying phases $\pm\phi$ and tilt functions $\pm\tau$. It is also seen that there appears higher odd orders such as $\pm 3, \pm 5$, ... in addition to the ± 1 order beam. Each of these orders are diffracted to spatially separated positions as each diffracted order contains a different overall tilt. Thus, the diffraction orders $\pm 1, \pm 3, \pm 5$, ... are located at relative distances of $\pm 1, \pm 3, \pm 5$, ... with respect to the undiffracted zero order. Also, the diffracted orders have relative intensities $1/\pi^2$, $1/9\pi^2$, $1/25\pi^2$,... and carry relative phases $\pm\phi, \pm 3\phi, \pm 5\phi, \ldots$. The location of each of the diffracted order with respect to the undiffracted zero order is a function of the spatial frequencies, $f_{0x}$ and $f_{0y}$ and the order of diffraction. Thus, it is a simple matter to isolate any desired diffraction order from the other orders using an iris diaphragm in the focal plane. A beam with user defined phase profile $\phi$ can be realised by isolating the $+1$ diffraction order and then recollimating the beam using another lens. In this thesis work, we use the phase function $\phi$ to represent a beam with classical aberrations expressed as a linear combination of single index Zernike polynomials [65], such that $\phi(x,y) = \Sigma a_j Z_j(x,y)$ (where $a_j$ represents the RMS amplitude of the $j^{th}$ mode). The table below shows a few of such Zernike polynomials corresponding to some common optical aberrations. To be noted that if we do not consider the user defined phase function, i.e., $\phi(x,y) = 0$, then the hologram simply represents a plane binary diffraction grating pattern. This corresponds to a $+1$ order beam with a plane wavefront, deflected in a particular direction determined by the values of $f_{0x}$ and $f_{0y}$. Therefore in this thesis, the binary diffraction grating is often referred to as binary hologram and vice versa. Figure 3.2(i) shows numerically generated binary amplitude diffraction grating element with spatial frequencies (a) $f_{0x} = 8\pi$, (b) $f_{0x} = 16\pi$, (c) $f_{0x,0y} = 10\pi$ and (d) $f_{0x,0y} = 10\pi$ with $\phi = 2 \times Z_8$. The corresponding focal spots of row (i), are shown in (a)-(d) of row (ii). Figure 3.2(ii)(d) shows a magnified version of only the resulting $+1$ order diffraction spot.

| j | $Z_j(x, y)$ | Name |
|---|---|---|
| 4 | $\sqrt{3}(2(x^2+y^2)-1)$ | Defocus |
| 5 | $\sqrt{6}(x^2-y^2)$ | Primary astigmatism at ±45° |
| 6 | $2\sqrt{6}xy$ | Primary astigmatism at 0° |
| 7 | $\sqrt{8}(3(x^2+y^2)-2)x$ | Primary x coma |
| 8 | $\sqrt{8}(3(x^2+y^2)-2)y$ | Primary y coma |
| 9 | $\sqrt{8}(x^3-3y^2x)$ | x trefoil |
| 10 | $\sqrt{8}(3x^2y-y^3)$ | y trefoil |
| 11 | $\sqrt{5}(6(x^2+y^2)^2-6(x^2+y^2)+1)$ | Primary spherical aberration |
| 12 | $\sqrt{10}(4(x^2+y^2)-3)(x^2-y^2)$ | Secondary astigmatism at $\pm45^0$ |
| 13 | $\sqrt{10}(4(x^2+y^2)-3)(2xy)$ | Secondary astigmatism at $0^0$ |
| 14 | $\sqrt{10}(x^4+y^4-6x^2y^2)$ | — |
| 15 | $\sqrt{10}(4xy(x^2-y^2)$ | — |

**Table 3.1:** Single index Zernike polynomials with index varying from $Z_4 \rightarrow Z_{15}$.

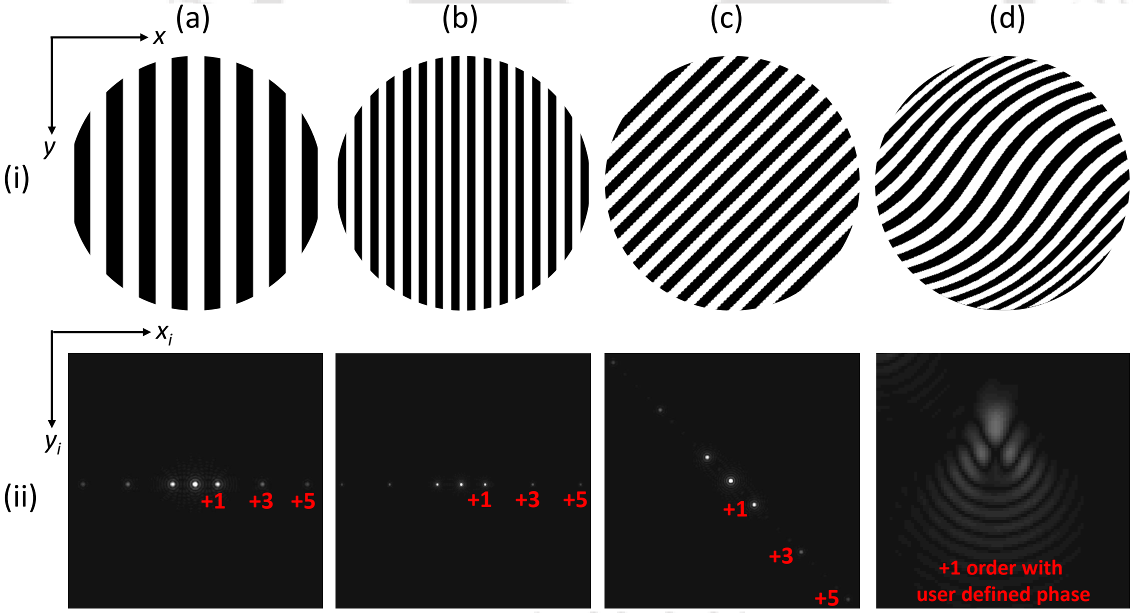

**Figure 3.2:** A binary amplitude diffraction grating with spatial frequencies (i)(a) $f_{0x} = 8\pi$, (i)(b) $f_{0x} = 16\pi$, (i)(c) $f_{0x,0y} = 10\pi$ and (i)(d) $f_{0x,0y} = 10\pi$ along with a phase profile, $\phi = 2 \times Z_8$. The corresponding diffraction spots obtained numerically are shown in (ii)(a)-(ii)(d).

## 3.6 Construction of Grating Array Based Zonal Wavefront Sensor

Due to various limitations associated with a conventional SHWS as discussed in chapter 1, we replace the tiny array of lenslets of the SHWS by an array of binary diffraction grating patterns discussed above, together with a single focusing lens. The grating elements are arranged in a regular 2D structure, similar to the lenslets array structure in the case of SHWS. As discussed already, the location of any of the $\pm n$ diffracted orders is a function of the spatial frequency of the respective grating element. Thus, if the spatial frequencies of each of the grating elements are properly configured, the focal spots corresponding to the $n^{th}$ diffraction order can be made to form a regular array in the case of an unaberrated incident beam. We assume that the size of each grating element is small enough in comparison to the curvature of the incident wavefront $\phi(x, y)$ (incorporated holographically). In such a case, the portion of the incident wavefront across each grating element will offer a slope relative to the plane of the grating element. This will result in a shift of the location of $\pm n$ diffracted order in proportion to the amount of slope received by each grating element, due to the wavefront deformation (or holographically added phase profile) added to the incident beam.

We consider the spatial frequencies of the top left grating element $(1, 1) = (f_{0x}^1, f_{0y}^1)$ and that of the grating element $(i, j) = (f_{0x}^i, f_{0y}^j)$. For all the gratings considered, uniform increments, denoted as $\Delta f_{0x}$ and $\Delta f_{0y}$, are applied between the adjacent grating elements along $i$ (row index) and along $j$ (column index). We then define

$$\begin{aligned} f_{0x}^i &= f_{0x}^1 + (i-1) \times \Delta f_{0x} \\ f_{0y}^j &= f_{0y}^1 + (j-1) \times \Delta f_{0y} \end{aligned} \tag{3.18}$$

if we consider the array to have a rectangular outline. For $\Delta f_{0x} = \Delta f_{0y}$, the resulting diffracted beams of $+1$ order (or any odd orders) will form an array of dimension $N \times N$ (where N is the grating array dimension) with square outline for an ideal incident beam. Such a configuration of the spatial frequency results in the formation of 2D array of $+1$ order focal spots similar to the focal spot array in the case of SHWS. Moreover, the transmittance functions for the same $N \times N$ grating array can be configured to form lesser number of focal spot rows than that in a conventional SHWS[59]. In such a case, the spatial frequency can be defined as,

$$\begin{aligned} f_{0x}^{i} &= f_{0x}^{1} + \left[ (i-1) + \left\{ (j-1) - Q\left( j-1,\, \frac{N}{N_r} \right) \frac{N}{N_r} \right\} N \right] \times \Delta f_{0x} \\ f_{0y}^{j} &= f_{0y}^{1} + Q\left( j-1,\, \frac{N}{N_r} \right) \times \Delta f_{0y} \end{aligned} \tag{3.19}$$

where $N_r$ is the number of rows and $Q(a, b)$ is the quotient of $a/b$. Now, to generate one row of focal spots by setting $N_r = 1$ in Eq. 3.19, results in a constant spatial frequency, $f_{0y}^{j}$ and an uniformly varying spatial frequency, $f_{0x}^{i}$, to form an uniformly separated focal spots. In this thesis, the $+1$ order diffracted beams have been considered owing to their higher intensities compared to the higher orders, although, diffracted beams of any order may serve the purpose of forming the 2D array of focal spots. A diagrammatic representation of the basic operation of wavefront sensing using a 2D array of binary diffraction grating pattern is shown in Fig. 3.3. A collimated light beam incident on the 2D binary grating array $G$ gets diffracted and is then focused by the lens $L$ onto the image plane where a camera $C$ is placed. The spatial frequencies are configured according to Eq. 3.18 to form a regular 2D array of focal spots in the case of an unaberrated or plane incident wavefront. In the presence of such a wavefront represented by $U_1U_2$, the focal spots lie at the centres of the respective detector subapertures, as shown within the blue dashed box in Fig. 3.3. These focal spot positions are called reference positions. The same focal spots are now found to shift from the centre of the detector subaperture on introduction of some deformity into the incident wavefront. Such a beam represented by $A_1A_2$,

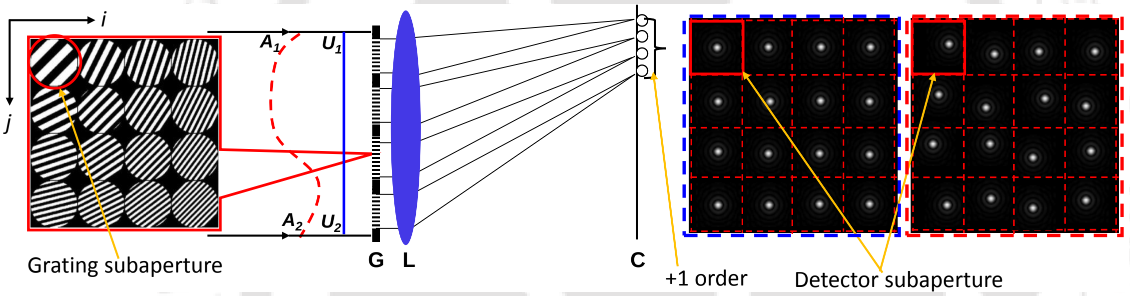

**Figure 3.3:** Schematic diagram of a grating array based zonal wavefront sensor. The 2D view, of the transmittance profile of the grating array containing 4 × 4 number of gratings and the corresponding +1 orders focal spot array of dimension 4 × 4, both in the absence and presence of aberrations, are shown on the extreme left and right of the figure, respectively.

will displace the array of focal spots from the reference positions, as shown within the red dashed box in Fig. 3.3. The shifts of the focal spots with respect to their reference positions give a measure of the local slope values. The phase profile of the entire beam under consideration can be obtained from these measured slope values by using one of the standard wavefront estimation algorithms[12].

## 3.7 Description of Important Components of the GAWS

There are various components that are required to develop the GAWS. A brief description about each of the major components is presented below.

### 3.7.1 Liquid Crystal Spatial Light Modulator

The spatial light modulator (SLM), as suggested by its name is a device [58] to modulate or modify the properties which include amplitude or phase or both amplitude and phase, of an incident beam of light. A number of devices are available which can modulate the properties of the incident light beam. Some of these devices are acousto-optic SLMs, magneto-optic SLMs, deformable mirror SLMs, liquid crystal SLMs, etc. In the present thesis work, we have used electrically addressed liquid crystal SLM (LCSLM) because of their easy implementability and integrability with a PC interface. In the LCSLM, the light transmittance property of an array of liquid crystal (LC) cell can be individually controlled by applying an electric field across the liquid crystal volume of an LC cell.

Liquid crystal is a material which possesses characteristics of both liquids and solids. Although it behaves like a fluid, there exists a regular arrangement of molecules similar to that of a solid. Liquid crystals can be classified into a number of phases based on the difference in optical properties such as birefringence. Primarily there are three types of LC molecules, namely, thermotropic, lyotropic and polymeric. Among them, thermotropic LC has been studied extensively and has found applications in various areas [66]. Again, the thermotropic LCs can exist in three phases, namely, nematic, smectic and cholesteric. Among them nematic LC and smectic LC are mostly used for display purposes on spatial light modulators. One common property of both the types of LC is that on application of an appropriate electric field across the LC volume, the orientation of the long axis of the LC molecule gets modified. The rotated molecules on the other hand effects the complex amplitude of the light beam being transmitted by the LC cell. This enables modifying the property of light beam at different locations of the beam cross section by applying different electric fields across various LC cells.

### 3.7.2 Nematic Liquid Crystal based SLM

A nematic liquid crystal spatial light modulator (NLCSLM) [58] as the name suggests is made up of a two dimensional array of LC cells which contains molecules in the nematic phase. The molecules in the nematic crystal are arranged randomly, yet there exists an order in regards to the orientation of the long axes of the molecules. The nematic LC molecules are placed between two alignment layers, with scratch marks (or the direction of polish) in a mutually perpendicular directions as shown in Fig. 3.4. As evident from the figure, the molecules present in direct contact with the layers are oriented so as to make the long axes parallel to the polish direction. When no field is applied across the LC cell, the molecules in the intermediate region reorient in a helical manner forming a $90^0$ twist starting from the entrance face up to the exit face as shown in Fig. 3.4(a). Due to this molecular arrangement, the incident beam of light (which is polarised parallel to the polish direction) that falls upon the entrance face undergoes a $90^0$ rotation in polarisation after passing through the cell. When an appropriate AC field is applied across the cell, with the help of two conducting electrodes, the $90^0$ twist in the molecular arrangement disappears and all the molecules are aligned in the direction of the applied field as shown in Fig. 3.4(b). It is to be noted that the dipole moment in the case of nematic LC is not a permanent dipole moment, rather an induced dipole moment. Thus, on changing

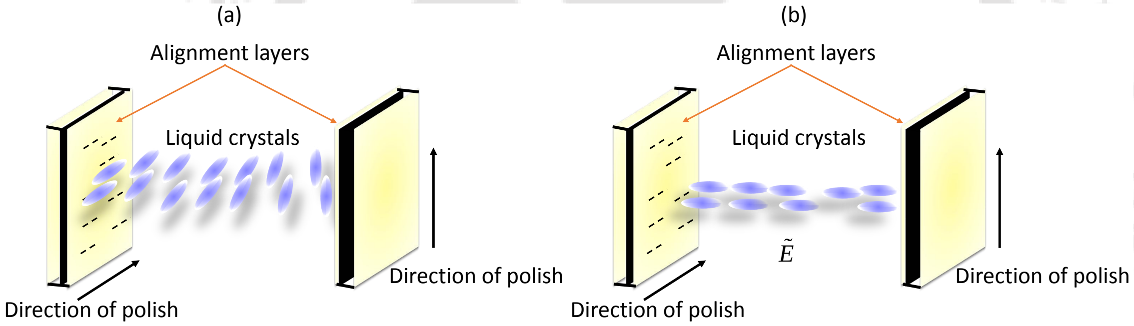

**Figure 3.4:** Molecular arrangements in a twisted nematic liquid crystal cell in (a) the absence of applied electric field and in the (b) presence of applied AC electric field.

the polarity of the applied electric field, the direction of the moment reverses. The LC molecules align in the same direction as the applied electric field regardless of its polarity, as the direction of the torque exerted is independent of the polarity of the applied voltage. The nematic LC molecules respond to the applied field in the time scale of milliseconds, thus giving a refresh rate of ~ 60 Hz to update the entire set of LC cells in the NLCSLM panel.

### 3.7.3 Ferroelectric Liquid Crystal based SLM

The ferroelectric liquid crystal spatial light modulator (FLCSLM) [58] is made up LC cells containing molecules in a certain type of the smectic phase, i.e., chiral smectic $C$ or smectic $C^*$ (also known as ferroelectric liquid crystal). In the smectic $C^*$ phase, the LC molecules are arranged in layers with the long axes of the molecules in each layer constrained to lie at an angle, say, $\Theta$ with respect to the layer normal. Thus, the LC molecules can rotate in a cone giving rise to a helical structure as shown in Fig. 3.5(a). Figure 3.5(b) illustrates the possible molecular orientation of a single ferroelectric liquid crystal (FLC) molecule. It is observed that the smectic $C^*$ phase does not exhibit any ferroelectric property in the macroscopic scale although each layer present in it is individually ferroelectric in nature. The FLC molecules have permanent electric dipole moment which allows them to interact strongly with the applied electric field. This gives rise to two stable molecular arrangements with respect to the layer normal, for each polarity of the applied electric field. The molecular orientation of the FLC molecules at $+\Theta$ and $-\Theta$ with respect to the layer normal, for electric fields of opposite polarity, has been illustrated in Fig. 3.6(a) and Fig. 3.6(b), respectively. Thus, the FLC molecules are bistable in nature and can

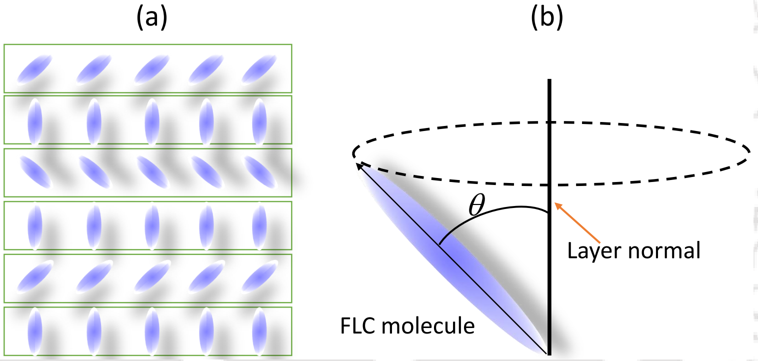

**Figure 3.5:** Ferroelectric liquid crystal molecules in (a) smectic-$C^*$ layered structure and (b) its allowed molecular orientation, in the absence of external applied electric field.

switch between the two states on application of the electric field. The FLC molecules respond to the applied field in a time scale of microseconds, thereby offering a refresh rate of $\sim$ 1.5 KHz to update all the LC cells in the panel in accordance with the digital signal from the computer.

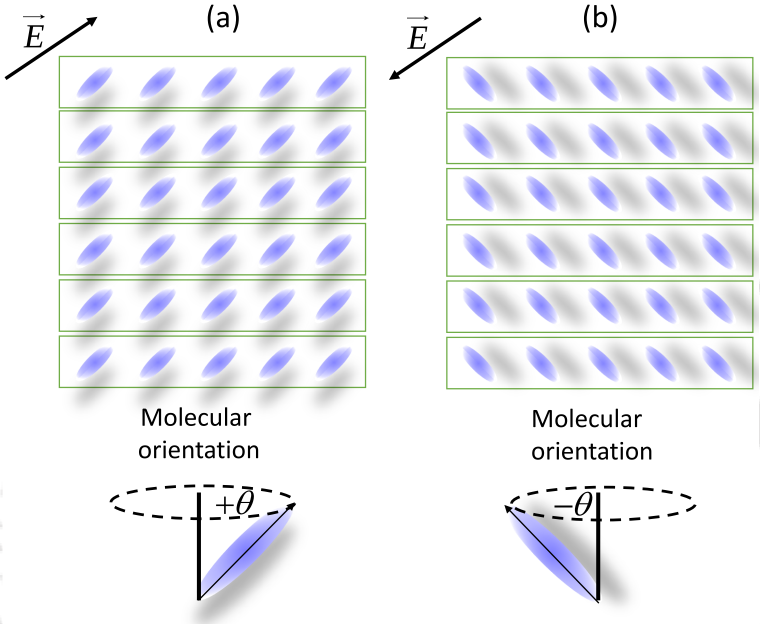

**Figure 3.6:** Ferroelectric liquid crystal molecules oriented at (a) $+\Theta$ to the surface normal for one direction of the applied electric field, and (b) oriented at $-\Theta$ to the surface normal for the other direction of the applied electric field.

In our experiment, we have used two types of high performance reflective type FLCSLM from Forth Dimension Display [67], having series number SXGA-R3 and SXGA-R2. Both the FLCSLMs have the same pixel resolution of $1280 \times 1024$ with a pixel pitch of 13.62 $\mu$m on a 20.68 mm × 18.87 mm area of the panel (active area is 17.43 mm× 13.95 mm). SXGA-R3 and SXGA-R2 are designed to display 24-bit native color depth (i.e., 8-bit for red color, 8-bit for green color and 8-bit for blue color) with a refresh rate of 85 Hz and 60 Hz, respectively. Thus, the panel when configured to display binary patterns can refresh at 2040 Hz and 1440 Hz for single bit patterns, for color refresh rate of 85 Hz and 60 Hz, respectively.

### 3.7.4 Camera

Digital camera is one of the important components of a SHWS or the GAWS, which is used to capture the focal spot arrays. The camera records a digital version of the image corresponding to the intensity distribution of the focal spots by accumulating photoelectrons, produced by the incident light. Two important types of scientific cameras used commonly in a Shack-Hartmann type wavefront sensors are the complementary metal-oxide semiconductor (CMOS) cameras and charge-coupled device (CCD) cameras. As discussed below, the working principle of both the CCD camera and the CMOS camera are different and both have their own advantages and limitations. However, both the cameras accomplish the same objective in a different way, i.e., both of them convert incident light (photons) into electronic charge (electrons). One can choose a particular type of camera based on the specific requirement.

### 3.7.5 Complementary Metal-Oxide-Semiconductor (CMOS) Camera

The CMOS camera [68] is made up of three important components, namely, color filters, pixel sensor array and analog-to-digital convertor (ADC). The array of pixel sensors are further composed of individual light sensors and active amplifiers. The light reaches the pixel sensor through a color filter whose function is to filter the incident beam into three basic colors. After the pixel sensor, a series of transistors present on the CMOS sensor amplify the photon-to-electron charge obtained from the pixel. The ADC converts the analog signal processed by the pixel sensor into digital form so that it becomes process worthy for the rest of the components in the circuit board. In CMOS, each of the pixels is read individually, by a scheme known as window-of-interest readouts. Although, this might reduce the uniformity over the individual sensors but its massively parallel arrangement allows the camera to work at a very high speed.

### 3.7.6 Charged Coupled Device (CCD) Camera

The CCD camera [68, 69] is also primarily made up of three important components, namely, color filter, pixel sensor array and an analog-to-digital converter. Similar to the CMOS sensor, the light captured by CCD is processed by the color filters prior to reaching the pixel array. From there, the analog signals are fed to an amplifier and then on to an analog-to-digital converter. The charge readout (from the read-out register) in a CCD is done row by row and charges in each of the rows are coupled to those which are immediately above it. Thus, when a particular row is read, its charges are immediately removed from the register and the next row follows it. In CCD, a few number of nodes are employed for the transfer of pixel charge into voltage. Thus, row by row reading with a few output nodes, helps in realizing a highly uniform output. The CCD imaging systems are found to be more complex when compared with the CMOS imaging systems. CMOS sensors are physically much smaller and consumes lesser power as all the required circuits and other components are embedded into the individual sensor. CMOS offers higher speed imaging with almost no blooming effect which can be attributed to the responsive character of the sensor as well as its ability to allow window-of-interest readouts [68].

In our experiments, we have used a high-speed camera link CMOS camera [70], manufactured by Basler having model number A504K. The pixel resolution of the camera is 1280×1024 (1.3 megapixels) with a pixel size of 12.0 $\mu$m. It has a maximum full frame rate of 500 fps which can go higher if lesser number of rows are activated. The camera can be triggered via an external synchronization signal or can run in an internally controlled free-run mode. It is compatible with a NI PCIe-1429 image acquisition device via a camera link cable communication interface.

We have also used a high speed USB 3.0 CMOS camera of Thorlab make, [71] with model number DCC3420M. Pixel resolution of the camera is 1280×1024 (1.3 megapixels) with a pixel size of 5.3 $\mu$m. It has a maximum full frame rate of 60 fps delivered via a USB 3.0 cable communication interface. This particular camera can also be triggered via an external synchronization signal or can run in an internally controlled free-run mode. The camera has an area of interest (AOI) function that facilitates high speed operation of the camera.

### 3.7.7 Frame Grabber Card

To enhance the flexibility of data acquisition and increase the frame rate of the Basler (A504K) camera link camera, without compromising on its resolution, we have used a camera link frame grabber card.

In our experiment, we have used a PCIe-1429 frame grabber card [72] manufactured by National Instruments (NI). The frame grabber card can be directly controlled using the National Instruments driver software NI-IMAQ. It is specifically used to acquire images in real time and transfer them directly to the system memory. It can also perform region of interest (ROI) acquisitions on all video modes and frames. This particular ability of the device allows it to collect a specific subset of the acquisition window, thereby speeding up the transfer and processing time for the image. The Basler camera is connected to the NI PCIe-1429 card through the MDR (mini delta ribbon) 26-pin connectors present on the frame grabber card. A serial communication is established to and fro between the NI PCIe-1429 and the camera through two LVDS (low-voltage differential signaling) pairs in the camera link cable. The frame grabber is interfaced with the personal computer using a ×4 PCIe (peripheral component interconnect express) expansion slot of the computer.

### 3.7.8 Laser

Laser is another primary component required for the development of the GAWS setup as it acts as the source of illumination to the array of binary holograms (realized with the LCSLM) to generate an array of diffracted spots.

In our experiments, we have preferred using a red Helium-Neon (He-Ne) laser [73] due to its high stability and coherency to produce a beam with $M^2 < 1.05$. The laser is manufactured by CVI Melles Griot, having part number 25-LHP-991-230. It operates at a wavelength of 633 nm and in the $TEM_{00}$ ($> 90\%$) mode. It has a beam diameter ($1/e^2$) of 0.65 mm with a far field divergence of 1.24 milliradian. The operating temperature is in between -$20^0C$ to $40^0C$. The output power of the laser is 10 mW and it takes less than 15 minutes to warm up, to reach the specified power stability.

We have also used a high power green Diode-Pumped Solid State (DPSS) laser [74]. This laser is also manufactured by CVI Melles Griot having part number 85-GCA-020. It is capable of delivering diffraction limited, $\mathrm{TEM}_{00}$ output with excellent power stability. It emits a wavelength of $532 \pm 1.0$ nm and has beam quality indicated by $M^2<1.2$. The laser has a beam diameter ($1/e^2$) of $1.1 \pm 0.2$ nm with a far field divergence of less than 1.25 milliradian. The operating temperature is in between $10^0C$ to $40^0C$. The output power of the laser is 20 mW and it takes less than 5 minutes to warm up, to reach the specified power stability.

### 3.7.9 Microcontroller Circuit

Another important component associated with the GAWS setup is the peripheral interface controller (PIC) based circuit that helps to generate an appropriate drive signal so that the SLM and the camera works in synchronization with each other.

We have developed a PIC microcontroller based USB communicable circuit board using PIC18F2550 [75] microcontroller (make Microchip) that has 28 pins with 10 bits resolution. For programming the PIC18F2550, an IDE (Integrated Development Environment) is installed that supports the respective microcontroller in conjunction with a compiler that can compile the code written on the IDE. There are many IDE available which support PIC18F microcontrollers. We have used MPLAB ICD2 to program the code written in C-language which is then converted into machine language using the compiler. The user code in the machine language can be written into the microchip via a USB communication. The PIC18F2550 microcontroller board receives a TTL signal from the FLCSLM which goes high only when display of pattern is in progress in the panel. The user code instructs the microchip to process the TTL signal and generate a trigger signal. This trigger signal is then fed to the camera to ensure that the camera acquisition takes place, at a suitable frame rate and at the moment when the required binary hologram or grating pattern is displayed.

## 3.8 Experimental Arrangement of the GAWS

We implement the grating array based zonal wavefront sensor by setting up an experimental arrangement whose schematic is shown in Fig. 3.7. We first use a green DPSS laser whose specifications have been mentioned earlier. A lens combination of $L_1$ and $L_2$ is used to expand and collimate the laser beam. The binary grating array pattern or the hologram generated in a LabVIEW program using a computer generated holography technique [29, 30] is written onto an FLCSLM. The incident beam diameter is made sufficiently large so that a square area of approximately 1.45 cm$\times$ 1.45 cm of the FLCSLM panel is illuminated uniformly. Lens $L_3$ collects the light diffracted by the binary hologram displayed on the FLCSLM and an iris diaphragm ID isolates the array of +1 diffracted orders from the various higher orders. The +1 order beams are then focused onto the camera using the lens $L_4$. We have used the USB 3.0 CMOS camera, to record the +1 diffracted orders.

### 3.8.1 Experimental Implementation

Some of the experimental results obtained using the above experimental arrangement is illustrated below. Here, we also perform numerical simulation using the

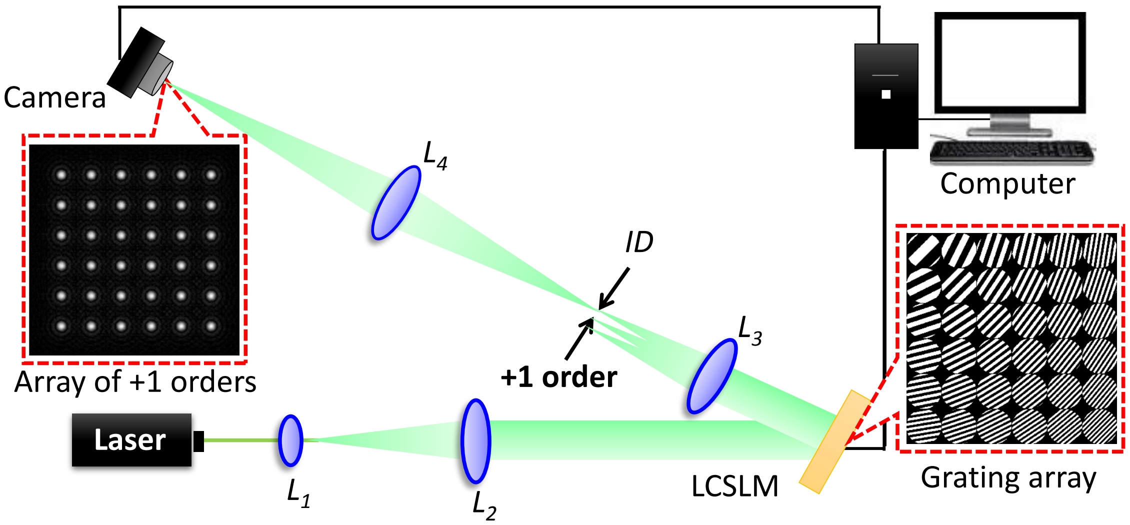

**Figure 3.7:** Schematic diagram of the experimental arrangement to implement the grating array based zonal wavefront sensor using a liquid crystal spatial light modulator.

grating array to compute an array of +1 order focal spots. Numerical simulations are performed in MATLAB by taking Fourier Transform operations over the binary grating patterns. Figures 3.8(i)(a)→ Fig. 3.8(i)(c), show the arrays of +1 order focal spots of dimensions 4×4, 6×6 and 8×8 obtained numerically, while Fig. 3.8(ii)(a)→ Fig. 3.8(ii)(c), show the corresponding experimentally obtained focal spot arrays. The fact, that the numerical and experimental results are in mutual agreement, goes on to establish the point that the GAWS is working reasonably well. The grating array dimensions are varied between 4×4, 6×6 and 8×8, keeping the incident wavefront dimension constant. Hence, with increasing grating array dimension, the size of each grating element and the consecutive +1 order focal spot separation decreases. This result demonstrates the capability of the setup to dynamically switch between various grating dimensions. It is observed that each of the detector subaperture for grating dimensions of 4×4, 6×6 and 8×8 contain different number of pixels. However, the total computational time required to locate the centroid positions remains constant for each of the grating array dimensions.

As discussed earlier, the CGH scheme implemented using the FLCSLM facilitates realising a single +1 order beam in the case of a single hologram or an array of +1 order beams in the case of an array of holograms, where the phase profile of the +1 order beam is user defined. If the grating subapertures are assumed to constitute the resultant aperture of the incident beam over which the aberration function is described, it is possible to generate +1 orders using an unaber-

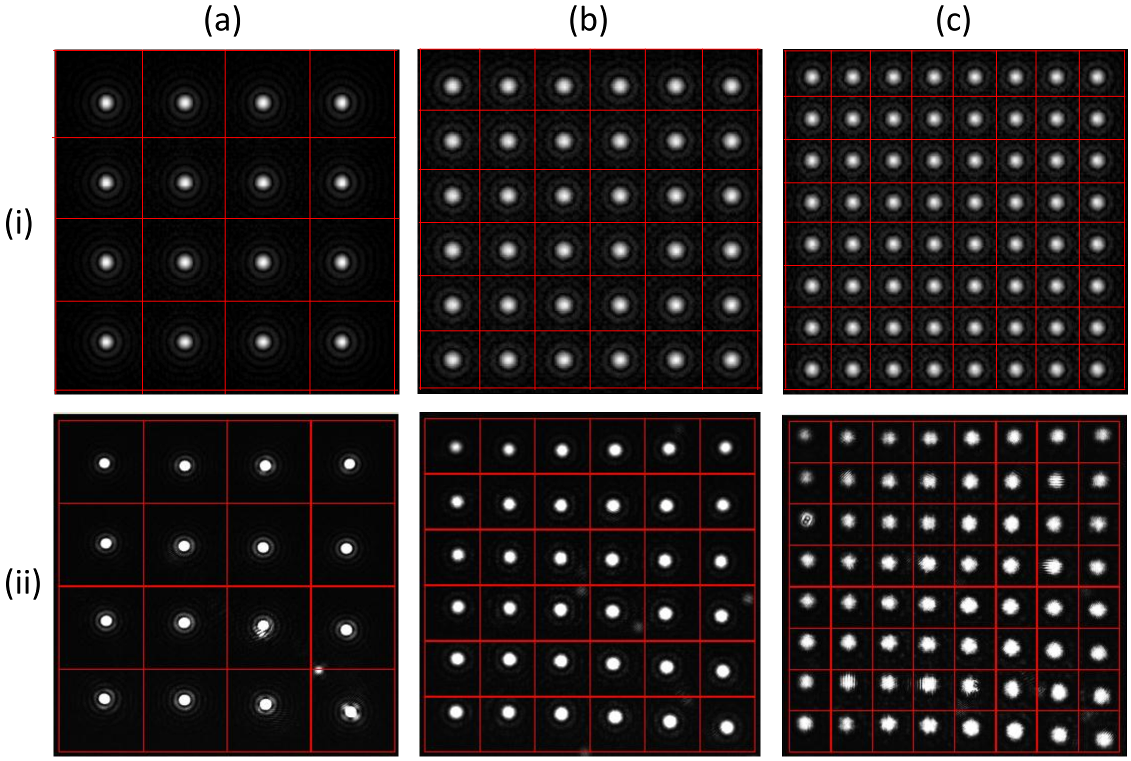

**Figure 3.8:** Focal spot array formed by the +1 order diffracted beams, corresponding to the grating pattern of dimensions (a) 4×4, (b) 6×6 and (c) 8×8, obtained (i) numerically, and (ii) experimentally.

rated incident beam which can be assumed to be holographically aberrated with the same aberration function. We demonstrate holographic introduction of Zernike mode aberration in an experiment using two different grid dimensions, i.e., 4×4 and 6×6. A linear combination of 8 Zernike modes as shown in Table 3.1 have been added holographically as applied phase to the reference beam [65], such that $\phi(x, y) = 1.5Z_4 - 1Z_5 - 0.8Z_6 + 0.5Z_7 + 0.8Z_8 - 0.5Z_9 + 0.6Z_{10} - 0.3Z_{11}$. The CMOS camera records the focal spot arrays twice. Once, in the beginning when the +1 orders carry the phase information of the reference beam and later when the incident beam is holographically deformed with the desired applied phase $\phi(x, y)$. The shifts of the focal spots are obtained from the two images and the horizontal and vertical slopes are calculated from the focal spot shifts along the horizontal and vertical directions, respectively. From these measured slope information, the incident wavefront is estimated using both the zonal estimation algorithm given by Southwell [12] and a modal estimation method, discussed in section 2.7 of chapter 2. Figure 3.9 shows a snapshot of the software programme developed in LabVIEW to implement the GAWS scheme.

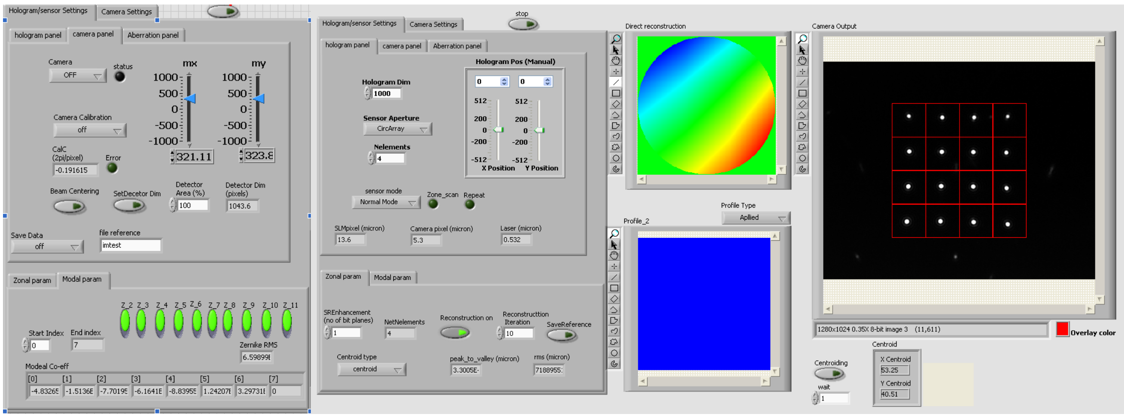

Camera: OFF
mx: 321.11
my: 323.8
Camera Calibration: off
CalC (2pi/pixel): -0.191615
Detector Area (%): 100
Detector Dim (pixels): 1043.6
Save Data: off
file reference: imtest
Start Index: 0
End index: 7
Zernike RMS: 6.59899
Modeal Co-eff: [0] -4.83265 [1] -1.5136E [2] -7.70195 [3] -6.1641E [4] -8.83955 [5] 1.24207E [6] 3.29731E [7] 0

Hologram Dim: 1000
Sensor Aperture: CircArray
Nelements: 4
Hologram Pos (Manual): 0, 0
sensor mode: Normal Mode
SLMpixel (micron): 13.6
Camera pixel (micron): 5.3
Laser (micron): 0.532
SREnhancement (no of bit planes): 1
NetNelements: 4
Reconstructtion Iteration: 10
Centroid type: centroid
peak_to_valley (micron): 3.3005E-
rms (micron): 7188955

Profile Type: Aplied
1280x1024 0.35X 8-bit image 3 (11,611)
Centroid
X Centroid: 53.25
Y Centroid: 40.51
wait: 1

**Figure 3.9:** Snap shot of the GUI corresponding to the GAWS computer programme developed in LabVIEW.

### 3.8.2 Results and Discussion

Figure 3.10 shows the applied and estimated phase profiles using modal estimation method and zonal estimation method for grating array dimensions of 4×4 and 6×6. The false color images of the applied phase profile $\phi(x, y)$ and its corresponding point spread function (PSF) in the camera plane are illustrated in rows (i) and (ii) of column (a). The bar diagrams in row (i) and (ii) of column (b) represent the root mean square (RMS) amplitudes of the 8 Zernike modes applied and detected using the modal estimation method for grating dimensions of 4×4 and 6×6, respectively. The plots of the estimated phase profiles using the modal estimation method, for grating array dimensions of 4×4 and 6×6, are shown in rows (i) and (ii) of column (c), respectively. The plots of bilinear interpolated phase profiles using zonal estimation method (Southwell algorithm), for grating array dimensions of 4×4 and 6×6, are shown in rows (i) and (ii) of column (d), respectively. All the plots in Fig. 3.10 are in radian units. The RMS value of the difference between the applied phase profile and the estimated phase profile is then used to estimate the errors in the measured phase profiles. The RMS error in the case of modal estimation is found to be 0.029 $\mu$m and 0.015 $\mu$m, whereas the same in the case of zonal estimation is found to be 0.341 $\mu$m and 0.285 $\mu$m, for grating array dimensions of 4×4 and 6×6, respectively. It is observed that the RMS error in the case of modal estimation method is much smaller in comparison to the zonal estimation method. Additionally, both the RMS error values are found to decrease with the increase in the dimension of the grating arrays.

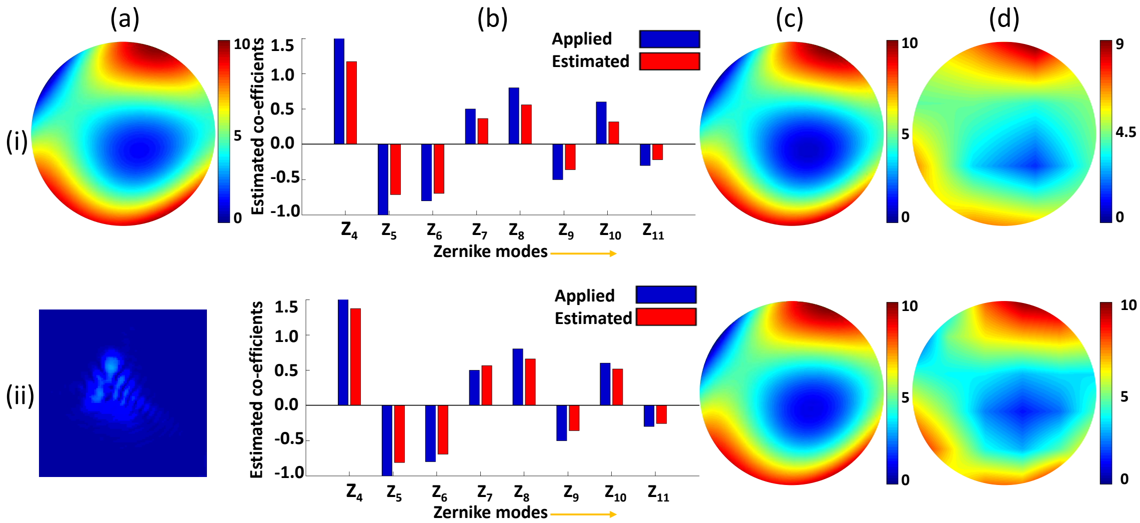

**Figure 3.10:** False color images representing the (a)(i) applied phase profile $\phi(x, y)$ and its (a)(ii) corresponding point spread function on the camera plane. The bar diagrams in (b)(i) and b(ii) show the RMS amplitudes of the 8 Zernike modes applied and detected using the modal estimation method for grating dimensions of 4×4 and 6×6, respectively. Figure (c)(i) and (c)(ii) represents the estimated phase profiles using the modal estimation method, in the case of 4×4 and 6×6 grating pattern, respectively, whereas (d)(i) and (d)(ii) represents the estimated phase profiles using the zonal estimation method, in the case of 4×4 and 6×6 grating pattern, respectively. The axis labels appearing in all the images have the unit of radian.

From the above experimental results it is clear that the GAWS is able to estimate the incident wavefront reasonably well and also offers easy and dynamic reconfiguration of the spatial frequencies of the grating elements. Moreover, it provides an option to dynamically switch between various grating array dimensions and offer flexibility over choosing the detector subaperture area.

## 3.9 High Speed Grating Array Based Zonal Wavefront Sensing

The SHWS has limited temporal resolution owing to the limited frame rate of the detector or camera used to capture the focal spots [76, 77]. This is because in a conventional SHWS, the focal spot array outline follows the outline of the lenslets array and the number of rows in the subaperture detector array is same as the number of rows of the lenslets array. This puts a limit on the achievable frame rate of the camera as almost all the rows of the camera should remain active. Since, the camera used is facilitated with AOI functionality, the reduction in height of the camera sensor array could have enabled it to work at a higher speed [78] than the full frame speed of the same camera, without affecting the sensor′s other performances.

### 3.9.1 Experimental Implementation

We generate a 1D array of focal spots by setting $N_r = 1$ in Eq. 3.19 as described in section 3.6. Figure 3.11 shows the transmittance function of a representative grating array of dimension $4 \times 4$ obtained using Eq. 3.19. Its corresponding 1D row of focal spots obtained numerically and experimentally are shown in Fig. 3.11(b) and Fig. 3.11(c), respectively. This result demonstrates that irrespective of the outline of the grating array, arbitrary outline of the effective camera area can be achieved.

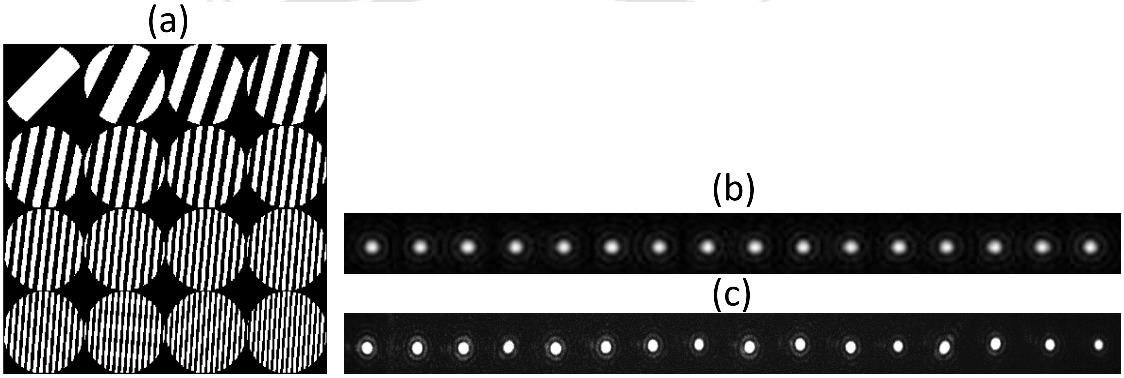

**Figure 3.11:** (a) Patterns representing the transmittance functions of the grating arrays of dimension $4 \times 4$ to produce +1 order focal spot array comprising only one row obtained, (b) numerically and (c) experimentally.

The high speed working of the camera and the sensor is realized using SXGA-R3 FLCSLM, whose specifications have been discussed earlier. As discussed earlier, the FLCSLM contains a panel which can display 24 single bit images per color image it receives. The FLCSLM is configured with proper sequence file (a firmware deciding the duration and order of display of various bit-planes) in order to split the input color image (written onto the FLCSLM) into 24 binary (i.e. single bit) images using a color image refresh rate of 85 Hz. In order to verify the high speed operation of the camera, we display 8 consecutive binary hologram arrays in the FLCSLM by sending a single color image. Each single bit image of the color image is in fact an array of binary holograms corresponding to an incident beam holographically aberrated with a certain Zernike mode aberration. The trigger signal derived from the FLCSLM synchronisation signal is sent to the camera to capture the focal spots for each 1 bit-plane, displayed for a duration of $125\mu$s. Thus, it enables the GAWS to capture focal spot arrays at a frame of at least ∼ 2 KHz, as only a few lines (i.e. $< 200$) of the camera are made active to capture the 1D array of focal spots. It is to be mentioned here that we use the Basler A504K camera having full frame speed of about ∼ 500 Hz. Each of the 8 single bit-planes in the color image sent to the FLCSLM introduces one of the Zernike modes of RMS amplitude 0.5 radian, from mode index $Z_4 \rightarrow Z_{11}$, into the incident beam. Figure 3.12(a) shows the PSF of the unaberrated incident beam. The eight consecutive frames of the camera (corresponding to $B_0, B_1, B_2, ...B_7$ bit-planes of the FLCSLM) used to capture the PSF of the incident beam aberrated with various Zernike modes (i.e. $Z_4 \rightarrow Z_{11}$) are shown in Fig. 3.12(b)→ Fig. 3.12(i), respectively. The focal spot arrays corresponding to the aberrated beam and the unaberrated beam can be employed to obtain the focal spot shifts which in turn can be used to estimate the wavefront that is holographically introduced.

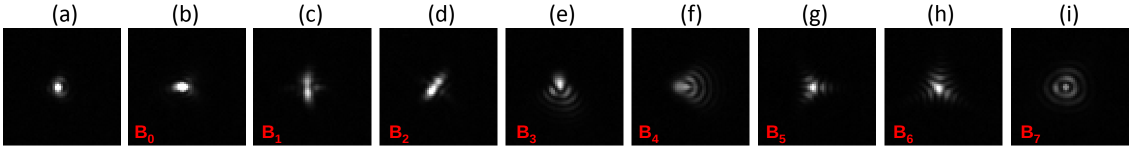

**Figure 3.12:** PSFs of the (a) unaberrated incident beam and (b)→ (i) the incident beam aberrated with each of the 8 different Zernike modes, from mode index $Z_4 \rightarrow Z_{11}$, respectively.

### 3.9.2 Results and Discussion

Here we use binary hologram array of dimension $4 \times 4$ designed to give rise to a focal spot array of dimension $1 \times 16$, for a plane incident wavefront. A color image representing a set of binary holograms and the corresponding 1D array of +1 order focal spots aberrated with 5 such Zernike modes ($Z_6 \rightarrow Z_{11}$, from top to bottom) are shown in Fig. 3.13(a) and Fig. 3.13(b), respectively. The gray scale plots of the applied phase profiles of the incident beam corresponding to the eight consecutive bit-planes are shown in Fig. 3.14(i)(a)→ Fig. 3.14(i)(h). The respective phase profiles estimated using modal estimation method are shown in Fig. 3.14(ii)(a)→ Fig. 3.14(ii)(h). The modal estimation is carried out using 8 Zernike modes ($Z_4 \rightarrow Z_{11}$) and the RMS values for the Zernike modes $Z_4 \rightarrow Z_{11}$ are found to be 0.4236, 0.3314, 0.1999, 0.3992, 0.3865, 0.2645, 0.3160, and 0.5286, respectively. All the plots shown are self-normalised and the estimated Zernike co-efficients are in the unit of radian.

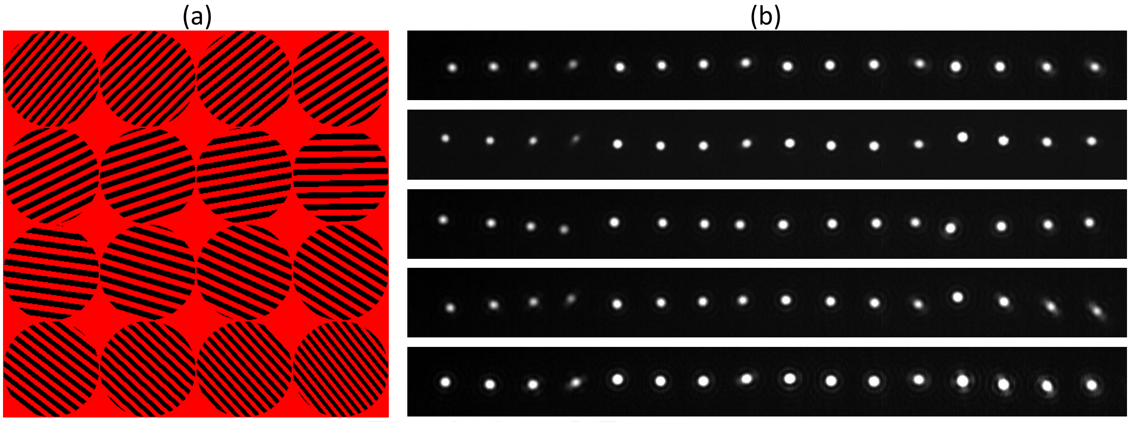

**Figure 3.13:** (a) A representative color image comprising 8 binary hologram arrays, (b) +1 order focal spot arrays corresponding to five different incident beam phase profiles.

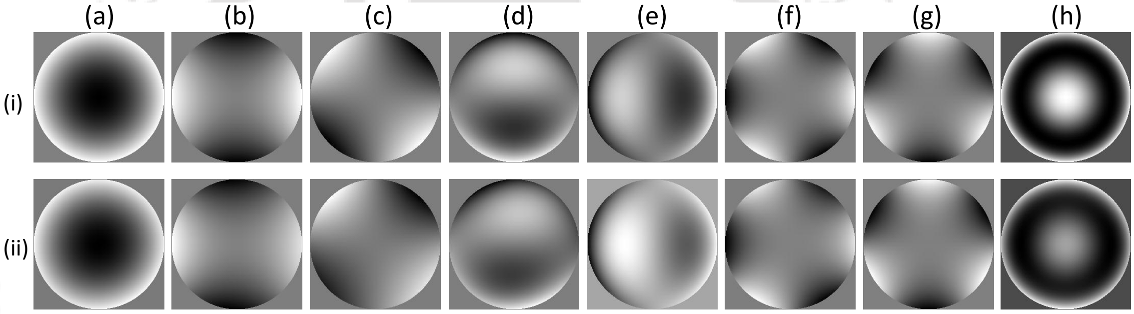

**Figure 3.14:** Sequence of (i)(a)→ (i)(h) applied phase profiles for eight consecutive frames and (ii)(a)→ (ii)(h) the corresponding estimated phase profiles.

## 3.10 Reduction in Crosstalk due to the 1D Array of Focal Spots

The term crosstalk refers to the event in a zonal wavefront sensor when the focal spot corresponding to one detector subaperture enters a nearby detector subaperture. This may be caused by the large local curvature of the incident wavefront across a particular lens aperture, in the case of a SHWS. The SHWS is very sensitive to the crosstalk as two or more focal spots in one detector subaperture will lead to wrong estimation of the focal spot centroid. Fortunately, construction of 1D array of focal spots [59] in a GAWS helps in reducing the amount of crosstalk in the vertical direction [79].

### 3.10.1 Experimental Implementation

An experiment similar to the one as discussed in section 3.8 has been carried out in order to demonstrate the minimization of crosstalk in a $1 \times N^2$ dimension of focal spot in comparison to $N \times N$ dimension of focal spot. The GAWS is used to estimate the wavefront of a holographically aberrated incident laser beam. Here, we have illustrated a particular result wherein we have considered $N = 4$ and incorporated -1.8 radian RMS amplitude of Zernike mode $Z_7$ into the reference beam, as it has a large curvature or slope along the vertical direction. Equation 3.18 and Eq. 3.19 have been used to generate binary hologram arrays of dimension $4 \times 4$ to result in $+1$ order focal spot arrays of dimension $4 \times 4$ and $1 \times 16$, respectively. Figure 3.15(a) and Fig. 3.15(c) show the reference arrays of focal spots of dimension $4 \times 4$ and $1 \times 16$, whereas Fig. 3.15(b) and Fig. 3.15(d) show their corresponding shifted arrays of focal spots due to the applied phase profile in the incident beam.

**Figure 3.15:** The $+1$ order focal spot array of dimension $4 \times 4$ (a) without any holographically added aberration and (b) with holographically added aberration (-1.8 $Z_7$). $1 \times 16$ array of $+1$ order focal spots in the (c) unaberrated case and (d) aberrated case.

### 3.10.2 Results and Discussion

The row (i) of column (a) in Fig. 3.16 shows the false color image of the applied phase profile $Z_7$ of RMS amplitude -1.8 radian. The plots of the estimated phase profile using the modal estimation method for focal spot dimensions of $4 \times 4$ and $1 \times 16$ are shown in rows (i) and (ii) of column (b). The modal wavefront estimation is carried out using 8 Zernike modes, $Z_4 \rightarrow Z_{11}$. The bar diagram in rows (i) and (ii) of column (c) represent the root mean square amplitudes of the 8 Zernike modes detected, for focal spot array dimensions of $4 \times 4$ and $1 \times 16$, respectively. All the plots in Fig. 3.16 are in radian units. The RMS value of differences between the applied phase profile and the estimated phase profile helps in the estimation of the errors in the measured phase profiles. For focal spot array dimensions of $4 \times 4$ and

$1 \times 16$, the RMS error is found to be 0.0295 $\mu$m and 0.0211 $\mu$m, respectively. Thus, the formation of 1D array of focal spots leads to an improvement in the wavefront measurement accuracy, owing to the reduction in the crosstalk.

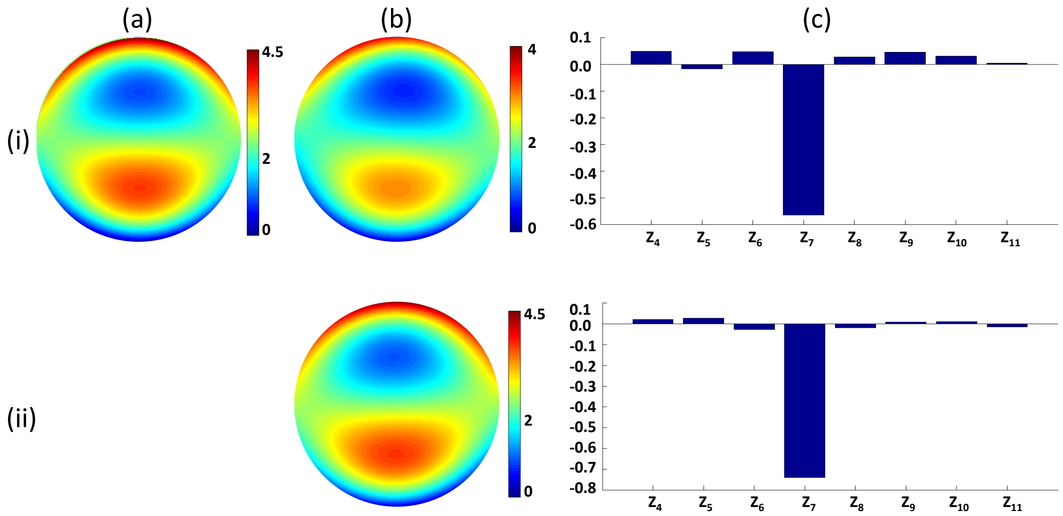

**Figure 3.16:** False color images representing the (a)(i) applied phase profile -1.8 $Z_7$. Figures (b)(i) and (b)(ii) represent the estimated phase profiles using modal estimation method, in the case of $4 \times 4$ and $1 \times 16$ focal spot array, respectively. The bar diagrams in (c)(i) and c(ii) show the RMS amplitudes of the 8 Zernike modes detected for focal spot array dimensions of $4 \times 4$ and $1 \times 16$, respectively. The axis labels appearing in all the images have the unit of radian.

## 3.11 Conclusion

In this chapter, we have shown via a thorough theoretical description as to how the periodicity and orientation of a binary diffraction grating decides the location of any desired diffraction order in the detector plane. We have also shown how an array of binary holograms or gratings can be configured such that one of the diffracted order gives rise to an array of focal spots in a way very similar to the Shack-Hartmann lenslet array. The construction of a grating array based zonal wavefront sensor using such an array of binary diffraction grating patterns has been described and its working has been demonstrated experimentally. Some of the advantages associated with the wavefront sensor, such as the dynamic reconfigurability between various grating array dimensions, high speed wavefront sensing and reduced crosstalk along vertical direction are discussed in detail with experimental results to substantiate the findings.

# CHAPTER 4

# Zonal Wavefront Estimation with Improved Algorithm for Shack Hartmann type Wavefront Sensors

## 4.1 Introduction

In this chapter, we put forward an improved zonal wavefront estimation algorithm, applicable for Shack Hartmann type wavefront sensors. The proposed algorithm is an improvement over the well-known W. H. Southwell algorithm, where phase at a specific point is described in terms of horizontal and vertical slope, and phase values. We show the mathematical expressions developed for the improved algorithm, alongwith the mathematical expressions of the Southwell algorithm. Experimental results are presented that demonstrate the improvement in wavefront estimation using the proposed algorithm, in comparison to the Southwell algorithm.

## 4.2 Review of the Related Work

Wavefront estimation in a zonal wavefront sensor [12] as discussed in chapter 2, involves two important steps. The first step is to obtain the slope values from the measured centroid positions, whereas the second step involves estimation of the wavefront from these measured slope values. However, estimation of the wavefront requires an estimation geometry along with an estimation algorithm. Three well known wavefront estimation geometries are, the Southwell geometry [12], the Fried geometry [20] and the Hudgin geometry [19], used to estimate the wavefront from the measured slope values. Of the three geometries, as far as robustness and error propagations are concerned, Southwell geometry is considered to be the best [21]. In the Southwell geometry, the phase value at each grid point is described in terms of the vertical and horizontal slopes at the symmetrically located adjacent grid points.

Although the Southwell geometry has been the popular geometry for wavefront estimation, a review of the literature reveals that several attempts were made to further increase the accuracy of wavefront estimation using the Southwell geometry. This includes a dither-based sensor proposed [22] to remove the inconsistency in wavefront estimation. Wavefront estimation accuracy can also be improved by using iterative compensation [23] method to remove the imperfection in the Southwell geometry. Both the methods have shown significant improvement in accuracy, yet the improvement has been achieved only at the cost of processing time. An alternative method was proposed by Visser et al.,[80] that suggests the use of estimation algorithm involving nonlinear multivariate splines in order to improve the accuracy in the estimated phase profile over the entire beam. However, this method provides better result than the Southwell geometry only in high signal to noise ratio (SNR) regimes (i.e. when $\mathrm{SNR} > 0.6$). Recently, the concept of truncation error in integration equations was introduced to reduce the estimation error in the Southwell geometry [24]. The truncation error can be minimised by incorporating more number of slopes in the integral equation based on the Taylor theorem. However, the method considered only the vertical and the horizontal slope values in the integral equation and the Taylor expansion was performed at an imaginary point rather than the actual grid points. Very recently, Guang et al. [81] proposed a higher-order iterative compensation method, to improve the estimation accuracy and convergence rate of the Southwell algorithm by employing two higher-order difference algorithms called S2 and S3. However, such a method utilises S2 and S3 algorithms to obtain the slope values from the wavefront estimated initially, using the conventional least square method. Thus, the process of estimation is time consuming and accurate wavefront estimation is achieved at the cost of other propagating errors (like slope measurement error) as it depends solely on the initial estimated wavefront. In this chapter, we propose an algorithm to improve the accuracy in wavefront estimation by incorporating diagonal slope and phase values into the estimation algorithm in addition to the vertical and horizontal slope and phase values [82].

## 4.3 Theoretical Considerations

We denote 9 discrete phase value points also referred to as grid points, represented by nine black dots and, by row indices $(i-1)\rightarrow(i+1)$ and column indices $(j-1)\rightarrow(j+1)$, as shown in Fig. 4.1(a). In the Southwell algorithm, the mean horizontal or vertical slope at an intermediate point between two adjacent grid points in the horizontal or vertical direction is expressed in terms of the corresponding phase differences as shown in Fig. 4.1(b). Thus, if $\phi(i,j)$, $S^x(i,j)$ and $S^y(i,j)$ represents the phase, the horizontal slope and the vertical slope, respectively, at the location $(i,j)$, then the relation between phase and slope values in the case of Southwell algorithm can be written [12] as

$$\left.\begin{aligned}
\frac{d}{2}\left[S^x(i,j+1)+S^x(i,j)\right] &= \left[\phi(i,j+1)-\phi(i,j)\right]\\
\frac{d}{2}\left[S^x(i,j-1)+S^x(i,j)\right] &= \left[\phi(i,j)-\phi(i,j-1)\right]\\
\frac{d}{2}\left[S^y(i+1,j)+S^y(i,j)\right] &= \left[\phi(i+1,j)-\phi(i,j)\right]\\
\frac{d}{2}\left[S^y(i-1,j)+S^y(i,j)\right] &= \left[\phi(i,j)-\phi(i-1,j)\right]
\end{aligned}\right\} \tag{4.1}$$

where $d$ is the separation between two adjacent grid points in the vertical or horizontal direction. This gives

$$\begin{aligned}
\phi(i,j) \quad = \quad & \frac{\phi(i,j+1)+\phi(i,j-1)+\phi(i+1,j)+\phi(i-1,j)}{4}\\
& +\frac{d}{4}\left[S^x(i,j-1)-S^x(i,j)+S^y(i-1,j)-S^y(i,j)\right]
\end{aligned} \tag{4.2}$$

Equation 4.2 represents the Southwell algorithm that estimates the phase at a grid point $(i,j)$ from the phase and slope information at 4 adjacent grid points.

Let us now consider a 2D function $\phi(x,y)$ to represent the phase in the $XY$ plane and a loop $C$ surrounding the point $O$ as shown in Fig. 4.2(a). By using the fundamental theorem of gradient operator ($\overrightarrow{\nabla}$) [83] and considering an arbitrary point $P(x,y)$ on the loop $C$, we can write [82],

$$\int_{P}^{O} \overrightarrow{\nabla}\phi(x,y)\bullet\overrightarrow{dl_P} = \phi(O)-\phi(P) \tag{4.3}$$

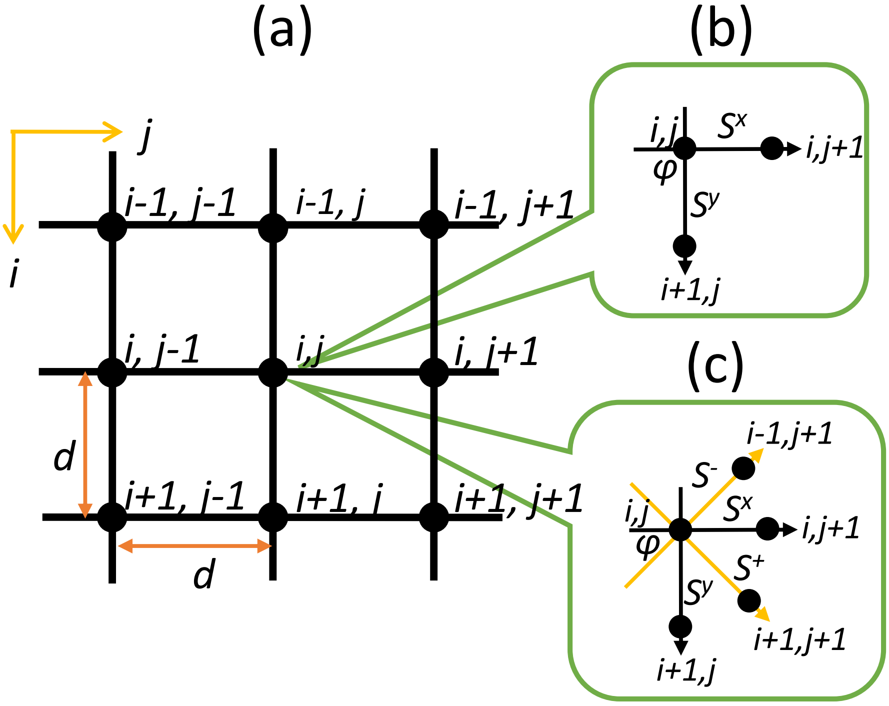

**Figure 4.1:** (a) Nine adjacent grid points (with $d$ as the separation between two adjacent horizontal or vertical grid points) corresponding to a rectangular Shack-Hartmann geometry and its corresponding estimation algorithm for (b) the Southwell geometry and (c) the improved geometry, where $S^x$, $S^y$, $S^+$ and $S^-$ vectors represents the horizontal slope, the vertical slope, the front diagonal slope and the back diagonal slope, respectively. The dots represent the locations of the phase points to be estimated.

where, $\overrightarrow{dl_P}$ represents the infinitesimal displacement vector along $\overrightarrow{PO}$. Integrating both sides of Eq. 4.3, we get,

$$\phi(O) = \frac{\int\limits_C \phi(P) dl_C}{\int\limits_C dl_C} + \frac{\int\limits_C \left( \int\limits_P^O \overrightarrow{\nabla\phi}(x,y) \bullet \overrightarrow{dl}_P \right) dl_C}{\int\limits_C dl_C} \tag{4.4}$$

where, $dl_C$ is the line element along the loop $C$. From the above equation it is clear that the phase at $O$ is the summation of mean phase on the loop and the mean of the integration over the product of phase gradient and the infinitesimal displacement vector over each line joining the loop and the point $O$. Now, if we represent the loop $C$ by $N$ number of discrete points and consider $dl$, the distance between $O$ and any arbitrary point $P$ on the loop to be very small, then Eq. 4.4 can be written as

$$\phi(O) = \left\{ \frac{\sum_{n=1}^{N} \phi(P)}{N} \right\} + \left\{ \frac{\sum_{n=1}^{N} \left\{ \overrightarrow{\nabla\phi}(P) \bullet \frac{\vec{dl}}{2} + \overrightarrow{\nabla\phi}(O) \bullet \frac{\vec{dl}}{2} \right\}}{N} \right\} \tag{4.5}$$

It is evident from Eq. 4.5, that phase at the point $O$ (i.e., $\phi(O)$) can be more accurately represented if the value of $dl$ is infinitely small and the value of $N$ is infinitely large. Thus, a more accurate phase estimation can be obtained at any grid point inside the loop by incorporating more number of sampling points into the loop, for an infinitesimal displacement vector joining a point on the loop and with the point inside the loop.

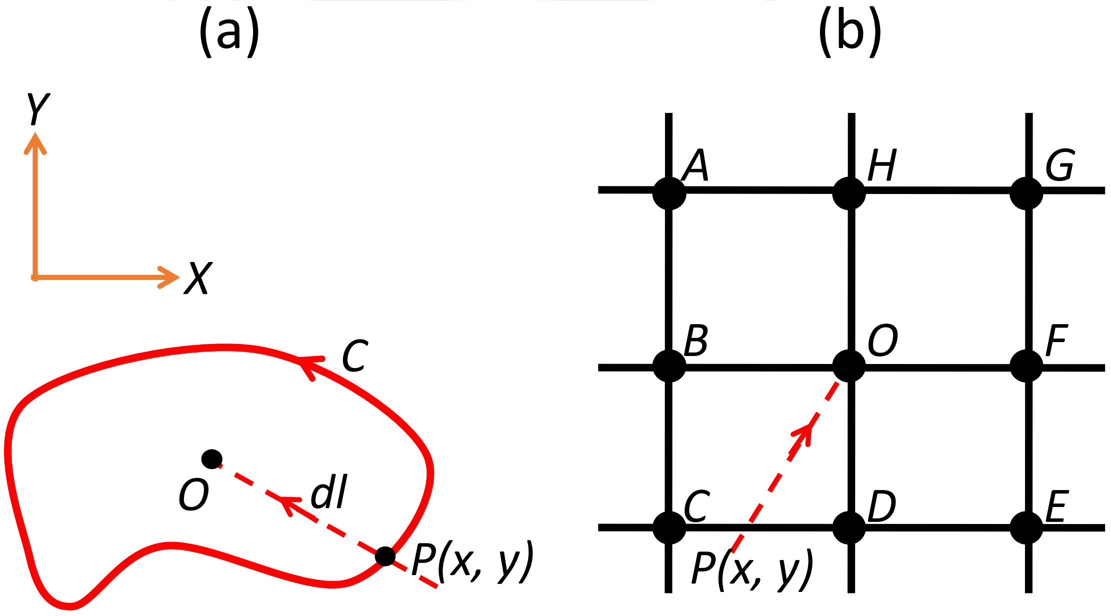

**Figure 4.2:** (a) A closed loop $C$ surrounding the point O. $d\vec{l}_P$ is the infinitesimal displacement vector along $\vec{PO}$ and $dl_C$ is the line element along the loop $C$. (b) The closed loop $ABCDEFGH$ formed by the eight adjacent grid points surrounding the grid point $O$.

Thus, the expression of phase at the location $(i, j)$ shown in the Southwell algorithm in Eq. 4.2, is in fact an alternative form of Eq. 4.5 for the loop $ABCDEFGH$ as shown in Fig. 4.2(b). Besides, the phase at $O$ is estimated accurately provided that the distance $d$ is made smaller and a large number of points in the loop are incorporated in the phase estimation.

In view of the above discussion, we propose an improved algorithm which describes the phase at $(i, j)$ with the inclusion of four additional points in the loop viz., the grid points $(i-1, j-1)$, $(i+1, j-1)$, $(i+1, j+1)$ and $(i-1, j+1)$. To accomplish this, two additional slope measurements are incorporated for each grid point, namely, the front diagonal (denoted as $S^{+}$) and the back diagonal (denoted as $S^{-}$) slopes, described as

$$\left.\begin{aligned} S^{+}(i,j) &= \frac{S^{x}(i,j)+S^{y}(i,j)}{\sqrt{2}} \\ S^{-}(i,j) &= \frac{S^{x}(i,j)-S^{y}(i,j)}{\sqrt{2}} \end{aligned}\right\} \tag{4.6}$$

Thus, in the proposed algorithm, phase value at $O$ is expressed in terms of the phase and slope values at the 8 surrounding grid points, i.e., $A$, $B$, $C$, $D$, $E$, $F$, $G$ and $H$.

## 4.4 Phase Estimation Algorithm

Once again, we consider the nine grid points shown in Fig. 4.1(a) to describe the proposed algorithm as shown in Fig. 4.1(c) where both the front diagonal and back diagonal adjacent slope and phase values in addition to horizontal and vertical points are incorporated. The relation between phase and slope values considering the diagonal grid points in the case of the improved algorithm can be written as

$$\left.\begin{aligned} \frac{d}{\sqrt{2}}\left[S^{+}(i,j)+S^{+}(i+1,j+1)\right] &= [\phi(i+1,j+1)-\phi(i,j)] \\ \frac{d}{\sqrt{2}}\left[S^{+}(i-1,j-1)+S^{+}(i,j)\right] &= [\phi(i,j)-\phi(i-1,j-1)] \\ \frac{d}{\sqrt{2}}\left[S^{-}(i,j)+S^{-}(i-1,j+1)\right] &= [\phi(i-1,j+1)-\phi(i,j)] \\ \frac{d}{\sqrt{2}}\left[S^{-}(i+1,j-1)+S^{-}(i,j)\right] &= [\phi(i,j)-\phi(i+1,j-1)] \end{aligned}\right\} \tag{4.7}$$

Writing $S^{+,-}$ using Eqs. 4.6 we have,

$$\phi(i,j) = \begin{cases} \phi(i+1,j+1) - \frac{d}{2}\left[S^{x}(i,j)+S^{y}(i,j)+S^{x}(i+1,j+1)+S^{y}(i+1,j+1)\right] \\ \phi(i-1,j-1) + \frac{d}{2}\left[S^{x}(i,j)+S^{y}(i,j)+S^{x}(i-1,j-1)+S^{y}(i-1,j-1)\right] \\ \phi(i-1,j+1) - \frac{d}{2}\left[S^{x}(i,j)-S^{y}(i,j)+S^{x}(i-1,j+1)-S^{y}(i-1,j+1)\right] \\ \phi(i+1,j-1) + \frac{d}{2}\left[S^{x}(i,j)-S^{y}(i,j)+S^{x}(i+1,j-1)-S^{y}(i+1,j-1)\right] \end{cases} \tag{4.8}$$

Combining Eq. 4.2 and Eq. 4.8 we get,

$$\begin{aligned}
\phi(i,j) &= \frac{1}{8}[\phi(i,j+1)+\phi(i,j-1)+\phi(i-1,j)+\phi(i+1,j)+\phi(i+1,j+1) \\
&+\phi(i-1,j+1)+\phi(i-1,j-1)+\phi^{(}i+1,j-1)]+\frac{d}{16}[-S^x(i,j+1) \\
&+S^x(i,j-1)-S^y(i+1,j)+S^y(i-1,j)-S^x(i+1,j+1) \\
&-S^y(i+1,j+1)+S^x(i-1,j-1)+S^y(i-1,j-1)-S^x(i-1,j+1) \\
&+S^y(i-1,j+1)+S^x(i+1,j-1)-S^y(i+1,j-1)] \qquad (4.9)
\end{aligned}$$

Thus, the improved algorithm is represented by Eq. 4.9 which effectively estimates the phase at any arbitrary grid point $(i,j)$ in terms of 8 adjacent slope and phase values. The above expression does not apply to grid points at the edge or at the corner of the array of the grid points. A general expression for $\phi(i,j)$ which takes into account all grid points (centre as well as periphery) in the array can be written as,

$$\begin{aligned}
\phi(i,j) &= \frac{1}{k_{i,j}} \sum_{(u,v)=(i-1,j-1)}^{(u,v)=(i+1,j+1),(u,v)\neq(i,j)} \sigma(u,v)\phi(u,v) \\
&+\frac{d}{2k_{i,j}}\Big[\sum_{u=i-1}^{u=i+1}\sigma(u,j-1)S^x(u,j-1)-\sum_{u=i-1}^{u=i+1}\sigma(u,j+1)S^x(u,j+1) \\
&+\sum_{v=j-1}^{v=j+1}\sigma(i-1,v)S^y(i-1,v)-\sum_{v=j-1}^{v=j+1}\sigma(i+1,v)S^y(i+1,v)\Big] \qquad (4.10)
\end{aligned}$$

where

$$\sigma(u,v)=\begin{cases} 1 & \text{if } (u,v) \text{ is in the array} \\ 0 & \text{if } (u,v) \text{ is outside the array} \end{cases} \qquad (4.11)$$

and

$$k_{i,j}=\begin{cases} 3 & \text{if } (i=1, \text{ and } j=1 \text{ or } N) \text{ or } (i=N, \text{ and } j=1 \text{ or } N) \\ 5 & \text{if } (i=1 \text{ or } N, \text{ and } j=2\rightarrow N-1) \\ & \text{or } (j=1 \text{ or } N, \text{ and } i=2\rightarrow N-1) \\ 8 & \text{if } (i=2\rightarrow N-1 \text{ and } j=2\rightarrow N-1) \end{cases} \qquad (4.12)$$

In a similar manner, the generalized form for the Southwell algorithm given by Eq. 4.2 can be written as

$$\begin{aligned}\phi(i,j) &= \frac{1}{k_{i,j}}\Big[\sigma(i-1,j)\phi(i-1,j)+\sigma(i,j-1)\phi(i,j-1)+\sigma(i+1,j)\phi(i+1,j)\\ &\quad +\sigma(i,j+1)\phi(i,j+1)\Big]+\frac{d}{2k_{i,j}}\Big[\sigma(i,j-1)S^x(i,j-1)\\ &\quad -\sigma(i,j+1)S^x(i,j+1)+\sigma(i-1,j)S^y(i-1,j)\\ &\quad -\sigma(i+1,j)S^y(i+1,j)\Big] \qquad (4.13)\end{aligned}$$

where $\sigma(u,v)$ has the same form as in Eq. 4.11, and

$$k_{i,j}=\begin{cases} 2 & \text{if } (i=1, \text{ and } j=1 \text{ or } N) \text{ or } (i=N, \text{ and } j=1 \text{ or } N)\\ 3 & \text{if } (i=1 \text{ or } N, \text{ and } j=2\rightarrow N-1)\\ & \text{or } (j=1 \text{ or } N, \text{ and } i=2\rightarrow N-1)\\ 4 & \text{if } (i=2\rightarrow N-1 \text{ and } j=2\rightarrow N-1)\end{cases} \qquad (4.14)$$

Thus, the estimated phase values for a beam with rectangular cross section or over a rectangular portion of the beam are obtained from Eq. 4.10 and Eq. 4.13. However, for a situation where the beam has a circular cross section and has a diameter less than or equal to the horizontal or vertical length of the sensor area, a small modification of the equations is necessary. Let, us consider $R$ to be the radius of the circular beam cross section with its centre co-coinciding with the centre of the sensor area and $d_{u,v}$ to be the distance of the grid point $(u,v)$ from the common centre. In such a case of a circular beam cross section, Eq. 4.12 for the proposed algorithm takes the form

$$k_{i,j}=\sum_{(u,v)=(i-1,j-1)}^{(u,v)=(i+1,j+1),\,(u,v)\neq(i,j)}\sigma(u,v) \qquad (4.15)$$

while, Eq. 4.14 for the Southwell algorithm takes the form

$$k_{i,j}=\sigma(i,j-1)+\sigma(i-1,j)+\sigma(i,j+1)+\sigma(i+1,j) \qquad (4.16)$$

where for both the algorithms

$$\sigma(u,v)=\begin{cases}1 & \text{if } d_{u,v}\leq R\\ 0 & \text{if } d_{u,v}>R\end{cases} \qquad (4.17)$$

Phase values can be estimated with the use of Eq. 4.10 or Eq. 4.13 via different iterative methods such as Jacobi, Gauss-Seidel, or successive over relaxation [12]. In the present work, however, only the Jacobi′s method has been considered for the sake of computational simplicity.

## 4.5 Experimental Implementation of the Algorithms

An experimental arrangement comprising a grating array based zonal wavefront sensor as shown in Fig. 4.3 is used to implement the Southwell and the proposed wavefront estimation algorithm, discussed above. The incident beam from the He-Ne laser is expanded and collimated using a lens combination of $L_1$ and $L_2$, before it is allowed to fall on the LCSLM (SXGA-R2) panel that displays the binary grating array pattern. The light diffracted by the grating pattern is collected by a third lens $L_3$. Another lens $L_4$ along with an iris diaphragm $ID$ is used to separate the +1 order beams from the other diffracted orders. A grating array of dimension $6 \times 6$ is written onto the FLCSLM. The resulting focal spot array of the same dimension obtained in the detector (Basler A504K CMOS camera) plane is shown within the red dashed box in the Fig. 4.3. We use computer generated holography technique [29, 30] to modify the grating patterns so as to holographically add or subtract various aberrations into the incident wavefront. The arrangement also enables replacing the array of gratings with just one large grating so as to give rise to only one +1 order focal spot in the detector plane for the same combination of incident and holographically added aberrations.

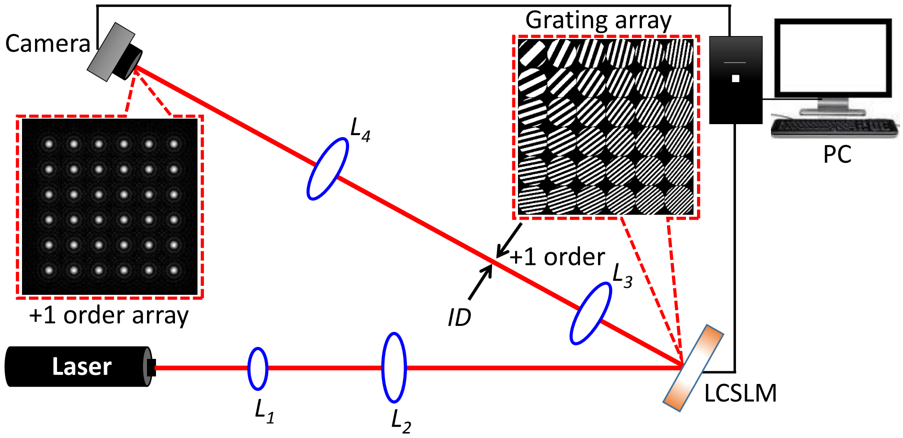

**Figure 4.3:** Schematic diagram of the grating array based zonal wavefront sensor.

## 4.6 Results and Discussion

As mentioned already, the experiment is performed using the grating array of dimension $6 \times 6$ described over $1024 \times 1024$ number of pixels of the LCSLM. In order to represent various aberrations to be added or subtracted holographically, single indexed Zernike mode polynomials (denoted as $Z_j$) [65] as shown in Table 3.1 of chapter 3 are considered. With the use of an expanded laser beam that overfills the grating array having a rectangular outline, it can be assumed that the 2D functions representing the Zernike mode polynomial too has a rectangular outline. Although the phase values are determined over $6 \times 6$ locations of the beam, the same is extended upto $1024 \times 1024$ pixels using bilinear interpolation which is of the same size as that of the input Zernike mode aberrations. Initially the Zernike mode $Z_4$ of RMS amplitude $= 1$ rad is incorporated into the incident beam. The wavefront estimation is performed employing the shifts of the focal spot array, using both Southwell algorithm represented by Eq. 4.13 and our proposed algorithm represented by Eq. 4.10. We use Jacobi′s iterative method to solve both the set of equations, where all the $N^2$ phase points are evaluated simultaneously without updating the phase values at the grid points sequentially, for a given iteration. The phase values of the incident and the estimated wavefronts are scaled between 0 and 1 so that the two can be easily compared. The modulus of the difference between the normalised phase profile of the input wavefront and its corresponding estimated wavefront as obtained using the Southwell algorithm and the proposed algorithm, respectively, after the sixth iteration are shown as surface plots in Fig. 4.4(a) and Fig. 4.4(b). It is evident that the proposed algorithm has the ability to estimate the wavefront with more resemblance to the input wavefront, especially in the interior region. Both the algorithms are employed to estimate the phase values for the iteration number varying between 1 and 100. The mean square deviation between the estimated phase values and the input phase values for the $6 \times 6$ grid points for each iteration number (denoted as $t$) is shown in Fig. 4.4(c). The mean square deviation plots clearly establish the superiority of the proposed algorithm.

In order to test the capability of the proposed algorithm to estimate higher order wavefront deformations, two higher order Zernike mode polynomials, namely, $Z_{14}$ and $Z_{15}$ are considered. Figure 4.5(a) and Fig. 4.5(b) show surface plots of modulus of the difference between the normalized phase profile of the input wavefront, i.e. Zernike mode $Z_{14}$, and the corresponding estimated wavefronts using

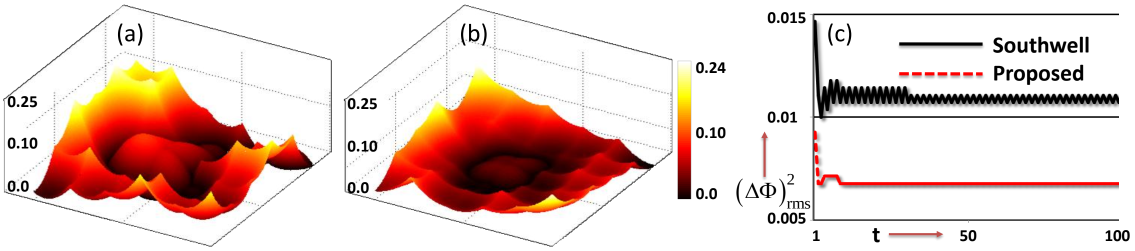

**Figure 4.4:** The modulus of the difference between the normalized phase profiles of the input wavefront ($Z_4$), and its corresponding estimated wavefront using (a) the Southwell algorithm and (b) the proposed algorithm, after six iterations, employing Jacobi's method, represented as surface plots. The common color bar for both the figures is attached to (b). (c) The mean square ($\Delta\phi^2_{rms}$) deviations between the input phase values and the estimated phase values using both the algorithms with iteration number ($t$), for the $6 \times 6$ grid points are shown as line plots. The solid black line and the red dashed line corresponds to the Southwell algorithm and the proposed algorithm, respectively. The vertical axes in (a), (b) and (c) have the unit of radian.

the Southwell algorithm and the proposed algorithm, respectively, after the sixth iteration. It is noticed that the proposed algorithm is able to estimate the central portion of the wavefront in a much better way relative to the Southwell algorithm. The mean square deviations between the phase values at the grid points, estimated using the two algorithms, are also obtained for iterations varying between 1 and 100. The mean square deviation plots for varying number of iterations are shown in Fig. 4.5(c). The modulus of the difference between the normalised phase profiles of the input wavefront, i.e. Zernike mode $Z_{15}$, and the corresponding estimated wavefront obtained using the Southwell algorithm and the proposed algorithm after the sixth iteration are shown in Fig. 4.6(a) and Fig. 4.6(b), respectively. The corresponding mean square plots for the iteration number varying between 1 and 100 are shown in Fig. 4.6(c). Once again it is observed that likewise the previous two cases, the proposed algorithm is capable of estimating the input wavefront more accurately in the interior part of the beam. Noteworthy, that in the Fig. 4.4→Fig. 4.6 the mean square deviation associated with the plots in (a) and (b) is not necessarily the same as that in plot (c) as the latter is obtained without the bilinear interpolation. Additionally, plot (c) in Fig. 4.4→Fig. 4.6 brings forward another important observation that amongst the three input wavefront profiles, the Zernike modes $Z_4$ and $Z_{15}$ are estimated more accurately relative to the Zernike mode $Z_{14}$, by both the algorithms. Nevertheless, the proposed algorithm performs remarkably better in the estimation of wavefront for both the lower order and higher order phase profiles as compared to the Southwell algorithm. The relative improvement of the proposed algorithm in wavefront estimation as compared to Southwell algorithm in terms of mean square deviation error is found to be about 42% and 24% in the case of Zernike modes $Z_4$ and $Z_{15}$, respectively, whereas it is found to be only 10% in the case of $Z_{14}$. The variation in the performance of the proposed algorithm for different applied Zernike modes (i.e., $Z_4$, $Z_{14}$ and $Z_{15}$) is attributed to the variation in the standard deviations of each of the Zernike modes. The proposed algorithm shows better performance for the Zernike modes $Z_4$ and $Z_{15}$, relative to the Zernike mode $Z_{14}$ as the standard deviation is minimum in the case of $Z_4$ and maximum in the case of $Z_{14}$. From plots (c) in Fig. 4.4→Fig. 4.6, we further observe that wavefront estimation accuracy in the case of Southwell algorithm fluctuates with iterations, whereas such fluctuations are non-existent in the case of the proposed algorithm.

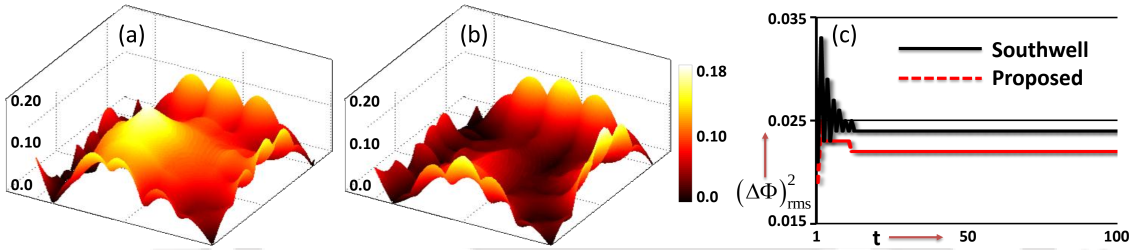

**Figure 4.5:** The modulus of the difference between the normalized phase profiles of the input wavefront ($Z_{14}$), and its corresponding estimated wavefront using (a) the Southwell algorithm and (b) the proposed algorithm, after six iterations, employing Jacobi's method, represented as surface plots. The common color bar for both the figures is attached to (b). (c) The mean square ($\Delta\phi^2_{rms}$) deviations between the input phase values and the estimated phase values using both the algorithms with iteration number ($t$), for the $6\times6$ grid points are shown as line plots. The solid black line and the red dashed line corresponds to the Southwell algorithm and the proposed algorithm, respectively. The vertical axes in (a), (b) and (c) have the unit of radian.

Another experiment was performed to observe the relative performance of both the algorithms for the detection of other Zernike mode aberrations. It was done by sequentially incorporating 0.5 radian RMS amplitude of various Zernike mode aberrations, $Z_j$, with $j = 4 \rightarrow 15$, into the incident beam. The mean square deviation in the estimated phase values at the grid points for each Zernike mode aberration is obtained using both the estimation algorithms after the first and hundredth iterations. It is further observed that there exists a small variation in the mean square deviation for different camera frames of the focal spot array, for the same algorithm and iteration and, with the same input wavefront profile. Therefore, instead of re-

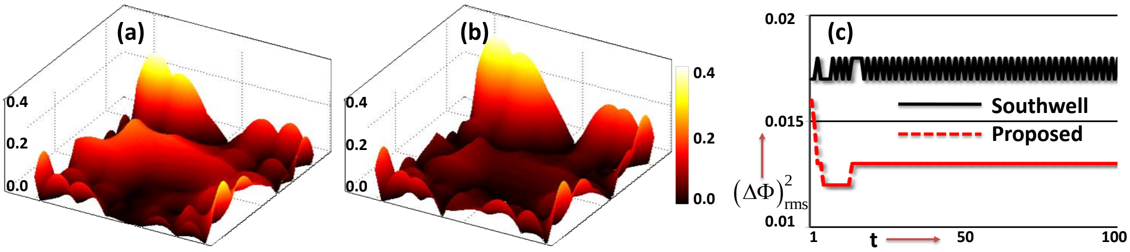

**Figure 4.6:** The modulus of the difference between the normalized phase profiles of the input wavefront ($Z_{15}$), and its corresponding estimated wavefront using (a) the Southwell algorithm and (b) the proposed algorithm, after six iterations, employing Jacobi′s method represented as surface plots. The common color bar for both the figures is attached to (b). (c) The mean square ($\Delta\phi^2_{rms}$) deviations between the input phase values and the estimated phase values using both the algorithms with iteration number ($t$), for the $6 \times 6$ grid points are shown as line plots. The solid black line and the red dashed line corresponds to the Southwell algorithm and the proposed algorithm, respectively. The vertical axes in (a), (b) and (c) have the unit of radian.

| **Algorithm** | **Iteration** ($t$) | $Z_4$ | $Z_5$ | $Z_6$ | $Z_7$ | $Z_8$ | $Z_9$ | $Z_{10}$ | $Z_{11}$ | $Z_{12}$ | $Z_{13}$ | $Z_{14}$ | $Z_{15}$ |
|---|---|---|---|---|---|---|---|---|---|---|---|---|---|
| **Proposed** | 1 | 0.03775 | 0.04061 | 0.07298 | 0.0068 | 0.01621 | 0.01173 | 0.01723 | 0.03464 | 0.01851 | 0.00543 | 0.00885 | 0.01175 |
| **Southwell** | 1 | 0.04794 | 0.0553 | 0.08467 | 0.00745 | 0.0172 | 0.01791 | 0.02122 | 0.03808 | 0.02087 | 0.00559 | 0.01164 | 0.01801 |
| **Proposed** | 100 | 0.01452 | 0.02147 | 0.01423 | 0.00523 | 0.00336 | 0.00585 | 0.00441 | 0.0199 | 0.0216 | 0.00565 | 0.00498 | 0.00517 |
| **Southwell** | 100 | 0.01541 | 0.02307 | 0.02057 | 0.00555 | 0.00389 | 0.00592 | 0.00596 | 0.02051 | 0.0233 | 0.0058 | 0.00535 | 0.00622 |

**Table 4.1:** Table shows the minimum of mean square deviations ($\Delta\phi_{rms}$) after the first and hundredth iteration, using the Southwell algorithm and the proposed algorithm to detect 0.5 rad RMS amplitude of various Zernike mode, $Z_j$, with $j = 4 \rightarrow 15$.

lying on just one camera frame we considered five camera frames to estimate five sets of mean square deviation values. Table. 4.1 shows the minimum of the five mean square deviation values after the first and hundredth iteration, respectively, using the two estimation algorithms. It is seen that for each Zernike mode aberration and iteration considered, the proposed algorithm provides more accuracy in the wavefront estimation.

To make yet another study on the performance of the algorithms, an unknown aberration was introduced into the incident beam by slightly displacing one of the beam expanding lenses placed in front of the grating array (i.e., lens $L_2$). Figure 4.7(a)(i) shows the $+1$ order focal spot, corresponding to a single large grating pattern prior to displacing the lens, while the same spot after distorting the wavefront is shown in Fig. 4.7(a)(ii). The phase profile of the unknown distorted wavefront is estimated from the shifts of the focal spot array corresponding to a $4 \times 4$ grating array using both the algorithms after 1, 2, 3, 4, 5, 10, 20, 50 and 100 numbers of iterations. A compensatory phase profile, which is the opposite of the wavefront estimated, is then holographically incorporated into the input beam in order to recover the original phase profile. An enhancement of the +1 order focal spot peak intensity corresponding to the single large grating pattern indicates the correctness of the estimated wavefront. The +1 order focal spots (the left image inside the solid red box corresponds to the proposed algorithm while the right image inside the dashed blue box corresponds to the Southwell algorithm) after the incorporation of the compensatory phase profiles and after iteration number 2, 10 and 100 are shown in Fig. 4.7(b), Fig. 4.7(c) and Fig. 4.7(d), respectively. A line plot indicating the intensity along a line across each focal spot is also shown below the focal spot in Fig. 4.7. In addition, we have plotted the peak intensity values of the +1 order focal spots obtained using the two algorithms for iteration numbers, $t = 1$, 2, 3, 4, 5, 10, 20, 50 and 100 and the same is shown in Fig. 4.8. It is observed that the proposed algorithm offers superior estimation in comparison to the Southwell algorithm even for unknown wavefront as indicated by the relatively higher peak intensities of the focal spot for all the iterations using the proposed algorithm. Further from Fig. 4.8, it is observed that the proposed algorithm shows far better performance in comparison to the Southwell algorithm for lesser iteration numbers. However, for large number of iterations, the difference in the performance by the two algorithms does not differ by a significant amount.

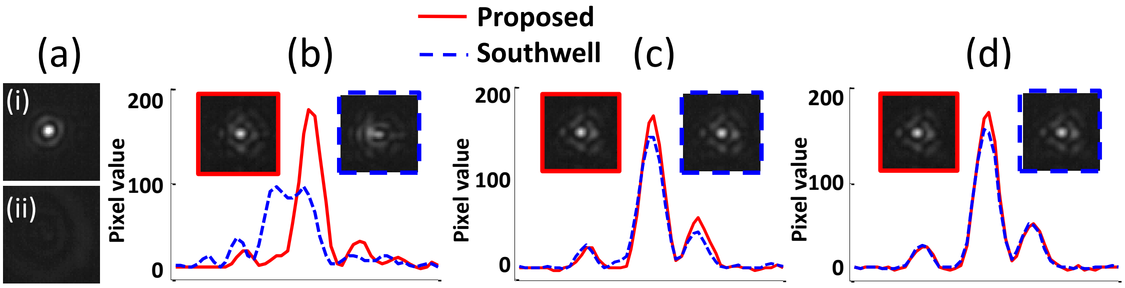

**Figure 4.7:** The grey scale plot of (a) the +1 order focal spot from a single large grating pattern in (i) the unaberrated and (ii) the aberrated case. The images of the +1 order focal spots after the incorporation of the compensatory wavefronts (images inside the solid red box and inside the dashed blue box corresponding to the Southwell algorithm and proposed algorithm, respectively) for iteration number (b) 2, (c) 10 and (d) 100. Also, the line plots through the centres of the corresponding focal spots is shown in (b)-(d). The X-axis and Y-axis for all the line plots are in camera pixel unit and the intensity value in arbitrary unit, respectively.

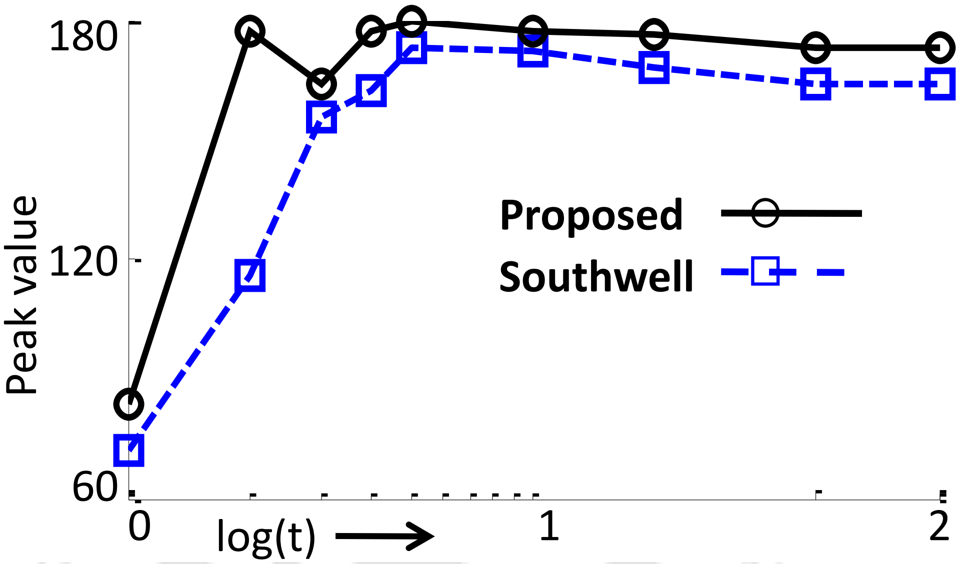

**Figure 4.8:** Plots showing the peak intensity in arbitrary units, of the +1 order focal spots estimated using Southwell algorithm and the proposed algorithm for iteration numbers, $t = 1, 2, 3, 4, 5, 10, 20, 50$ and $100$ (expressed in the log scale). The black solid line and the blue dashed line corresponds to the proposed algorithm and the Southwell algorithm, respectively.

## 4.7 Conclusion

In this chapter, we have introduced an improved version of the Southwell algorithm, to be used for zonal wavefront estimation in the Shack-Hartmann type wavefront sensors. We have incorporated diagonal slope and phase information in addition to the vertical and horizontal information for phase estimation at each grid point. Appropriate mathematical expressions have been developed for the proposed algorithm along with that of the Southwell algorithm. We have presented experimental results that demonstrate significant improvement in the wavefront estimation, using the proposed algorithm, in comparison to the Southwell algorithm.

## CHAPTER 5

# Investigation of Important Sources of Error in an Improved Zonal Wavefront Estimation Algorithm

## 5.1 Introduction

In this chapter, we investigate two important sources of error associated with the improved [82] zonal wavefront estimation algorithm, proposed in chapter 4 vis-a-vis the popular Southwell algorithm. The two important sources of error taken up for investigation are the slope measurement error and algorithm discretization error. Here, we provide an analytical work out to quantify both the slope measurement error and algorithm discretization error, for both the Southwell algorithm and the improved algorithm. Experimental results included in this chapter demonstrate the dependency of these theoretically obtained errors with the experimentally obtained root mean square (RMS) errors.

## 5.2 Review of the Related Work

A detailed description of the wavefront estimation process was provided for the first time by Saunders in 1961 [84] and later by Rimmer in 1974 [85]. They were followed by the works of Hudgin [19], Fried [20] and Southwell [12] describing their popular estimation algorithms. As we are aware that the SHWS converts the measured slope values into wavefront phase values using an estimation algorithm, only an appropriate estimation algorithm can properly interpret the measured slope values resulting in effective wavefront estimation. The performance of an estimation algorithm is characterised by the different types of errors that are associated with it. Thus, it is important to investigate these errors as when they become considerably large, they go on to decide the applicability of the given algorithm. So far Southwell algorithm has been considered to be one of the best as far as error propagation is concerned [21]. As discussed earlier, in the Southwell algorithm, the phase value at each grid point is described in terms of both the vertical and horizontal slope and the phase values at the symmetrically located adjacent grid points. Recently, we proposed an improved wavefront estimation algorithm [82] based on the Southwell algorithm, which was introduced in the previous chapter. This modified form of the algorithm expresses phase at each grid point not only using the horizontal and vertical adjacent phase and slope values, but also using the diagonal phase and slope values at the adjacent locations. It was shown experimentally that the improved algorithm was capable of estimating both the known as well as unknown wavefront deformations introduced into the incident beam, more accurately in comparison to the Southwell algorithm. Thus, the improved algorithm can be considered as a superior alternative to the conventional estimation algorithms for a Shack-Hartmann type zonal wavefront sensor. However, to assess the performance of the improved estimation algorithm in a comprehensive manner, it is essential to investigate various numerical errors associated with the algorithm. Primarily, there are two important sources of error [12, 21, 24, 86, 87] in a wavefront estimation process, namely slope measurement error (SME) and algorithm discretization error (ADE). The slope measurement error [88], also known as detector centroiding error is generated due to the presence of noise in slope measurements. The algorithm discretization error [89] is the inherent error associated with the process of approximating an exact mathematical procedure onto a discrete geometry.

## 5.3 Theoretical Considerations

Before moving to the calculation of errors, let us briefly discuss the salient expressions associated with the Southwell algorithm and the improved algorithm. Likewise in chapter 4, we denote the phase, the horizontal slope and the vertical slope at the location $(i, j)$, as $\phi(i, j)$, $S^x(i, j)$, $S^y(i, j)$, respectively. The relation between phase and slope values in the case of Southwell algorithm as shown in Fig. 5.1(a) and (b) together can be written [12] as

$$\left.\begin{aligned}
\frac{d}{2}\left[S^x(i,j+1)+S^x(i,j)\right] &= \left[\phi(i,j+1)-\phi(i,j)\right]\\
\frac{d}{2}\left[S^x(i,j-1)+S^x(i,j)\right] &= \left[\phi(i,j)-\phi(i,j-1)\right]\\
\frac{d}{2}\left[S^y(i+1,j)+S^y(i,j)\right] &= \left[\phi(i+1,j)-\phi(i,j)\right]\\
\frac{d}{2}\left[S^y(i-1,j)+S^y(i,j)\right] &= \left[\phi(i,j)-\phi(i-1,j)\right]
\end{aligned}\right\} \tag{5.1}$$

where $d$ represents the separation between two adjacent grid points in the vertical or horizontal direction. Thus,

$$\begin{aligned}
\phi(i,j) \;=\; & \frac{1}{4}\left[\phi(i-1,j)+\phi(i,j-1)+\phi(i+1,j)+\phi(i,j+1)\right]\\
& +\frac{d}{8}[S^x(i,j-1)-S^x(i,j+1)+S^y(i-1,j)-S^y(i+1,j)]
\end{aligned} \tag{5.2}$$

Equation 5.2 represents the Southwell algorithm where the grid point $(i,j)$ is surrounded by 4 adjacent grid points. Similarly, in the improved algorithm [82] as shown in Fig. 5.1(a) and (c) together, the relation between phase and slope values (considering only the diagonal points) can be written as

$$\begin{aligned}
&\tfrac{d}{2}[S^x(i,j)+S^y(i,j)+S^x(i+1,j+1)+S^y(i+1,j+1)] = [\phi(i+1,j+1)-\phi(i,j)]\\
&\tfrac{d}{2}[S^x(i,j)+S^y(i,j)+S^x(i-1,j-1)+S^y(i-1,j-1)] = [\phi(i,j)-\phi(i-1,j-1)]\\
&\tfrac{d}{2}[S^x(i,j)-S^y(i,j)+S^x(i-1,j+1)-S^y(i-1,j+1)] = [\phi(i-1,j+1)-\phi(i,j)]\\
&\tfrac{d}{2}[S^x(i,j)-S^y(i,j)+S^x(i+1,j-1)-S^y(i+1,j-1)] = [\phi(i,j)-\phi(i+1,j-1)]
\end{aligned} \tag{5.3}$$

Combining Eq. 5.1 and Eq. 5.3 we get,

$$\begin{aligned}
\phi(i,j) \;=\; & \frac{1}{8}[\phi(i,j+1)+\phi(i,j-1)+\phi(i-1,j)+\phi(i+1,j)\\
& +\phi(i+1,j+1)+\phi(i-1,j+1)+\phi(i-1,j-1)+\\
& \phi(i+1,j-1)]+\frac{d}{16}[-S^x(i,j+1)+S^x(i,j-1)-\\
& S^y(i+1,j)+S^y(i-1,j)-S^x(i+1,j+1)-S^y(i+1,j+1)\\
& +S^x(i-1,j-1)+S^y(i-1,j-1)-S^x(i-1,j+1)+\\
& S^y(i-1,j+1)+S^x(i+1,j-1)-S^y(i+1,j-1)]
\end{aligned} \tag{5.4}$$

Equation 5.4 represents the improved algorithm where the grid point $(i, j)$ is surrounded by 8 adjacent grid points. To estimate the wavefront using least square fit technique, a compact relationship between the measured slope values and the discrete unknown phase values is obtained in the form of a matrix equation [12]. The matrix formulation for Southwell algorithm, can be written using Eq. 5.1 as

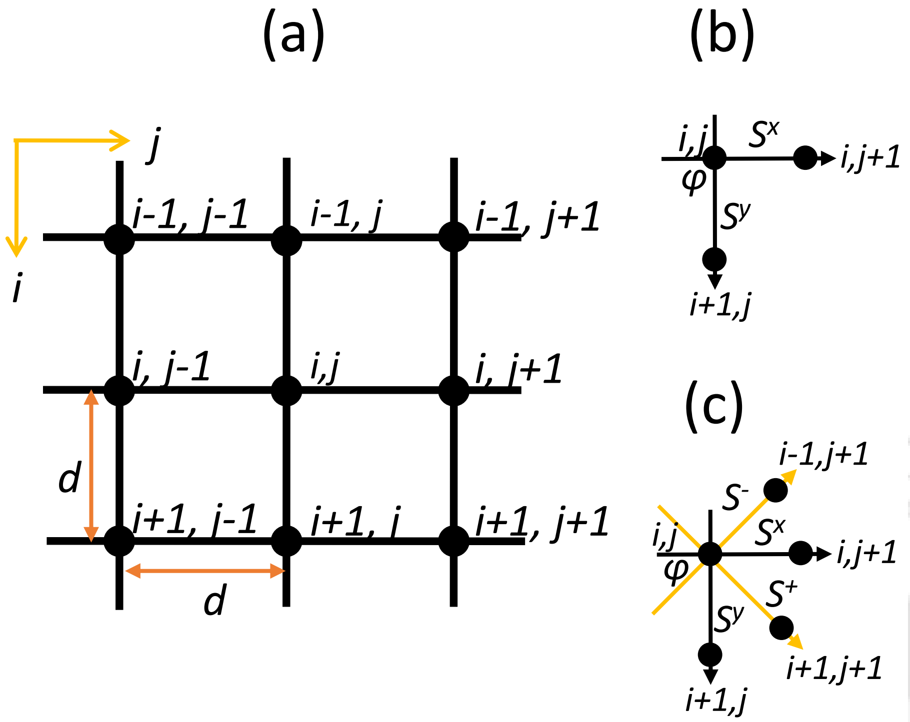

**Figure 5.1:** Zonal wavefront (a) estimation geometry and its associated estimation algorithm for (b) the Southwell algorithm and (c) the improved algorithm where the horizontal slope, vertical slope, front diagonal slope and back diagonal slope vectors are represented by $S^x$, $S^y$, $S^+$ and $S^-$, respectively. The black dots represent the locations of the phase points to be estimated.

$$S_S = A_S \phi_S \tag{5.5}$$

Similarly, the matrix formulation for the improved algorithm can be obtained by using Eq. 5.1 and Eq. 5.3, as

$$S_I = A_I \phi_I \tag{5.6}$$

Here $A$ is a sparse rectangular matrix, obtained from the respective algorithm, with a dimension of $2N(N-1) \times N^2$ in the case of Southwell algorithm and $(2N-2)(2N-$

$1) \times N^2$ in the case of proposed algorithm; $\phi$ is a column matrix of the wavefront to be estimated having $N^2$ elements in the case of both the algorithms, while $N$ being the grid dimension. Rewriting the left hand side of Eq. 5.5 and Eq. 5.6, we get,

$$S_S = \frac{1}{2} d C_S P_S \tag{5.7}$$

$$S_I = \frac{1}{2} d C_I P_I \tag{5.8}$$

where, $C$ is a sparse rectangular matrix of dimension $2N(N-1) \times 2N^2$ in the case of Southwell algorithm and $(2N-2)(2N-1) \times 4N^2$ in the case of improved algorithm, performing the addition of slope measurement of the neighboring grid; $P$ is a column matrix for slope measurement having $2N^2$ elements for the Southwell algorithm and $4N^2$ elements for the proposed algorithm.

## 5.4 Sources of Error

A wavefront estimation algorithm should have certain fundamental characteristics [12, 90]. These characteristics play an important role during selection of the estimation algorithm. One such criteria is the slower propagation of error to the wavefront estimation data, generated due to the noise in the slope measurement data. Since all real measurements are inherently affected by noise, the chosen algorithm must be effective in reducing the adverse effects of the noise in the measured data. Another important criteria is the unbiasness of the algorithm such that in the presence of any arbitrary additive noise, the actual wavefront is constructed as an average. Thus, in order to meet the aforementioned characteristics in a wavefront estimation algorithm, it is important to take into account the two important sources of errors, namely the slope measurement error or detector centroid error, and the algorithm discretization error, that significantly affects the wavefront estimation process.

The accuracy of SHWS depends on correct measurement of the focal spot centroid positions. The detector centroid error is responsible for creating discrepancies in the focal spot shift measurements and, hence is also known as slope measurement error. This slope measurement error propagates through the entire estimation algorithm and eventually results in error in the measured wavefront. Thus, it requires an error propagation co-efficient to quantify the associated errors in the wavefront estimation process. The error propagation co-efficient can be defined [21, 90] as the ratio of variance of the wavefront estimation error $\sigma_{we}^2$ to the variance of the wavefront measurement error $\sigma_{me}^2$. The wavefront estimation error refers to the error that is due to the induced wavefront error $\epsilon_i$, whereas wavefront measurement error refers to the error that is due to the wavefront slope measurement noise $\epsilon_{mn}$. A survey of the available relevant literature suggests the work of Zou and Rolland [21], who have extensively studied the slope measurement error in all the three available algorithms.

The presence of algorithm discretization error also affects the wavefront estimation accuracy. Since all estimation geometries are discrete in nature, algorithm discretization error arises during the process of solving the phase-slope equations of an estimation algorithm when it is adopted onto a discrete grid geometry. To define it more precisely, if we describe a function using the Taylor series expansion, the discretization procedure adopted during the development of a finite-difference relationship, when computed on discrete grid points, inevitably introduces an error. This error may be referred to as local truncation error of the Taylor series expansion which is produced due to the approximation of a continuous function. The same error can be termed as the algorithm discretization error in a wavefront estimation process. Thus, discretization error determines how well the finite-difference relationship, on a discrete geometry, approximates the continuous function. There are very limited number of articles available in the literature on algorithm discretization error, associated with a wavefront estimation algorithm. Nevertheless, in the case of Southwell algorithm it was shown [24] with the aid of the Taylor series expansion that at an intermediate imaginary point between two phase points, there exists an algorithm discretization error of $\mathcal{O}(\mathbf{d^3})$ (where $d$ is the distance between two adjacent grid points).

### 5.4.1 Slope Measurement Error

A centroid calculation is carried out within each subaperture detector area in a Shack-Hartmann type wavefront sensor, to determine the centre of mass of each of the focal spots. Let, us denote the $x$ and $y$ co-ordinate of the centroid locations, of the reference array of focal spots and the shifted array of focal spots by $[X_r(i,j), Y_r(i,j)]$ and $[X_s(i,j), Y_s(i,j)]$, respectively. Here, $(i,j)$ represents the row and column indices of the square array of lenslets. The displacement measurement of the shifted array with respect to the reference array, along horizontal and vertical directions result in two arrays of $x$-slope and $y$-slope denoted by $S^x$ and $S^y$, respectively. These measured slope values are related to the phase $\phi(x, y)$ in the presence of additive slope measurement noise $(\varepsilon^x_{sn}, \varepsilon^y_{sn})$ as

$$\begin{bmatrix} S^x(i,j) \\ S^y(i,j) \end{bmatrix} = \frac{1}{f} \begin{bmatrix} \Delta x(i,j) \\ \Delta y(i,j) \end{bmatrix} = \begin{bmatrix} \frac{\partial\phi(x,y)}{\partial x} + \varepsilon^x_{sn}(i,j) \\ \frac{\partial\phi(x,y)}{\partial y} + \varepsilon^y_{sn}(i,j) \end{bmatrix} \tag{5.9}$$

where $(x, y)$ represents the spatial co-ordinates of the wavefront, $\Delta x(i, j) = X_s(i, j) - X_r(i, j)$, $\Delta y(i, j) = Y_s(i, j) - Y_r(i, j)$ and $f$ is the focal length of each lenslet. These measured slope values carry the measurement noise or detector centroid noise which can be quantified in terms of the error propagation co-efficient. Here, we have carried out a detailed theoretical analysis of the error propagation due to slope measurement noise in the case of the improved algorithm based on the formulation given by Zou and Rolland [21]. Considering zero noise, Eq. 5.6 can be written as

$$S^0_I = A_I \phi^0_I \tag{5.10}$$

where, $S^0_I$ represents the true slope values of the improved algorithm. If the slope measurement contains a random additive noise $\varepsilon_{mn}$, then it leads to induced wavefront estimation error $\varepsilon_i$, such that

$$S_I = S^0_I + \varepsilon_{mn} \tag{5.11}$$

$$\phi_I = \phi^0_I + \varepsilon_i \tag{5.12}$$

where $\phi^0_I$ is the true phase value of the improved algorithm. Thus, in the presence of noise Eq. 5.10 becomes

$$A_I(\phi^0_I + \varepsilon_i) = S^0_I + \varepsilon_{mn} \tag{5.13}$$

$$A_I \varepsilon_i = \varepsilon_{mn} \tag{5.14}$$

The least square solution of Eq. 5.14 can be written as

$$\varepsilon_i = A_I^+ \varepsilon_{mn}$$

$$\varepsilon_i \varepsilon_i^T = A_I^+ \varepsilon_{mn} \varepsilon_{mn}^T (A_I^+)^T \tag{5.15}$$

where, $^+$ and $^T$ are the pseudo-inverse and transpose of the matrix concerned, respectively. Considering the relationship between $S_I$ and $P_I$ as given by Eq. 5.8, the wavefront measurement noise ($\varepsilon_{mn}$) and the wavefront slope noise ($\varepsilon_{sn}$) must satisfy

$$\varepsilon_{mn} = \frac{1}{2} d C_I \varepsilon_{sn} \tag{5.16}$$

Therefore, from Eq. 5.15, we get

$$\begin{aligned} \varepsilon_i \varepsilon_i^T &= \frac{d^2}{4} A_I^+ (C_I \varepsilon_{sn})(C_I \varepsilon_{sn})^T (A_I^+)^T \\ \varepsilon_i \varepsilon_i^T &= \frac{d^2}{4} A_I^+ C_I (\varepsilon_{sn} \varepsilon_{sn}^T) C_I^T (A_I^+)^T \end{aligned} \tag{5.17}$$

where, $\varepsilon_{sn}\varepsilon_{sn}^T$ for $m$ ($m$ is the total grid dimension, i.e., $m = N \times N$) total slope measurement points is given [91] by

$$\varepsilon_{sn}\varepsilon_{sn}^T = \begin{pmatrix} \varepsilon_1^2 & \varepsilon_1\varepsilon_2 & \cdots & \varepsilon_1\varepsilon_m \\ \varepsilon_2\varepsilon_1 & \varepsilon_2^2 & \cdots & \varepsilon_2\varepsilon_m \\ \vdots & \vdots & \ddots & \vdots \\ \varepsilon_m\varepsilon_1 & \varepsilon_m\varepsilon_2 & \cdots & \varepsilon_m^2 \end{pmatrix}$$

If we assume that the slope noise are independent, uncorrelated and have zero mean with the same variance $\sigma_s^2$, the ensemble statistical average of the slope noise can be written as

$$\langle (\varepsilon_{sn})_k (\varepsilon_{sn})_l \rangle = \sigma_s^2 \delta_{kl} = \begin{cases} 0 & \text{for } k \neq l \\ \sigma_s^2 & \text{for } k = l \end{cases}$$

$$\langle \varepsilon_{sn} \varepsilon_{sn}^T \rangle = \sigma_s^2 I \tag{5.18}$$

where $I$ is the identity matrix of dimension $m \times m$ and $\delta_{kl}$ is the Kronecker delta. Therefore, Eq. 5.17 gives,

$$\langle \varepsilon_i \varepsilon_i^T \rangle = \frac{d^2\sigma_s^2}{4} A_I^+ C_I C_I^T (A_I^+)^T \tag{5.19}$$

From the definition of Euclidian norm [92], we have

$$\parallel \varepsilon_i \parallel_2 = (trace\langle \varepsilon_i \varepsilon_i^T \rangle)^{\frac{1}{2}} \tag{5.20}$$

where $\parallel \varepsilon_i \parallel_2$ is the Euclidian norm of vector $\varepsilon_i$ and $\langle \bullet \rangle$ denotes the averaging operator. The mean variance of the wavefront estimation error, $\sigma_{we}^2$ is given as

$$\sigma_{we}^2 = \frac{(\parallel \varepsilon_i \parallel_2)^2}{m} = \frac{1}{m} trace\langle \varepsilon_i \varepsilon_i^T \rangle \tag{5.21}$$

Now, use of Eq. 5.19 yields

$$\sigma_{we}^2 = \frac{d^2\sigma_s^2}{4m} trace[A_I^+ C_I C_I^T (A_I^+)^T] \tag{5.22}$$

Similarly, the wavefront measurement error $\sigma_{me}^2$ is given as

$$\sigma_{me}^2 = \frac{(\parallel \varepsilon_{mn} \parallel_2)^2}{m} = \frac{1}{m} trace\langle \varepsilon_{mn} \varepsilon_{mn}^T \rangle \tag{5.23}$$

From Eq. 5.16 and Eq. 5.18, we get,

$$\langle \varepsilon_{mn} \varepsilon_{mn}^T \rangle = \frac{d^2}{4} C_I C_I^T \langle \varepsilon_{sn} \varepsilon_{sn}^T \rangle$$

$$\langle \varepsilon_{mn} \varepsilon_{mn}^T \rangle = \frac{d^2\sigma_s^2}{4} C_I C_I^T \tag{5.24}$$

Thus, Eq. 5.23 yields,

$$\sigma_{me}^2 = \frac{d^2\sigma_s^2}{4m} trace[C_I C_I^T] \tag{5.25}$$

From the definition of error propagation co-efficient for the improved algorithm, and using Eq. 5.22 and Eq. 5.25, we get

$$\eta_I = \frac{\sigma_{we}^2}{\sigma_{me}^2} \tag{5.26}$$

$$\eta_I = \frac{trace[A_I^{+} C_I C_I^T (A_I^{+})^T]}{trace[C_I C_I^T]} \tag{5.27}$$

Using similar arguments, we can show that the error propagation co-efficient for the Southwell algorithm can be written as

$$\eta_S = \frac{trace[A_S^{+} C_S C_S^T (A_S^{+})^T]}{trace[C_S C_S^T]} \tag{5.28}$$

Thus, Eq. 5.27 and Eq. 5.28 can be used to quantify the amount of error propagation in the improved algorithm as well as in the Southwell algorithm, respectively.

We consider lenslets array or grating array dimensions of $4\times4$, $6\times6$ and $8\times8$ to compute the error propagation co-efficients. For the Southwell algorithm it is found to be 0.1052, 0.0798 and 0.0649, whereas for the improved algorithm, the same is found to be 0.0356, 0.0242 and 0.0186, for grating array dimensions of $4 \times 4$, $6 \times 6$ and $8 \times 8$, respectively. From this result it is evident that there is a significant improvement in error propagation in the case of the improved algorithm relative to the Southwell algorithm.

### 5.4.2 Algorithm Discretization Error

If a function $f$ and its first $n+1$ derivatives are continuous on an interval $[x_i, x_{i+1}]$, then from the definition of the Taylor series [93], the value of the function at $x_{i+1}$ is given by

$$\begin{aligned} f(x_{i+1}) &= f(x_i) + f^1(x_i)(x_{i+1} - x_i) + \frac{f^2(x_i)}{2!}(x_{i+1} - x_i)^2 \\ &+ \frac{f^3(x_i)}{3!}(x_{i+1} - x_i)^3 + \cdots \end{aligned} \tag{5.29}$$

Thus, the Taylor series provides a mean to predict the value of the function at a point $x_{i+1}$ in terms of the values of the function and its derivatives at another point $x_i$. Now, taking $x_{i+1}$ - $x_i = d$, ($d$ being the step size or the distance between two neighboring grid points) Eq. 5.29 can be re-written as

$$f(x_{i+1}) = f(x_i) + f^1(x_i)d + \frac{f^2(x_i)}{2!}d^2 + \frac{f^3(x_i)}{3!}d^3 + \cdots \tag{5.30}$$

In the improved estimation algorithm, both the phase and slope values are calculated at the same grid point. Hence, considering improved algorithm shown in Fig. 5.1 (c) and applying Taylor series expansion, the horizontal slope values ($S^x$)

along $(i, j+1)$, $(i, j-1)$ and vertical slope values $(S^y)$ along $(i+1, j)$, $(i-1, j)$ can be written as

$$\left.\begin{aligned}
S^x(i,j+1) &= S^x|_{(i,j)} + d\frac{\partial S^x}{\partial x}|_{(i,j)} + \frac{d^2}{2!}\frac{\partial^2 S^x}{\partial x^2}|_{(i,j)} + \frac{d^3}{3!}\frac{\partial^3 S^x}{\partial x^3}|_{(i,j)} + \frac{d^4}{4!}\frac{\partial^4 S^x}{\partial x^4}|_{(i,j)} + \cdots \\
S^x(i,j-1) &= S^x|_{(i,j)} - d\frac{\partial S^x}{\partial x}|_{(i,j)} + \frac{d^2}{2!}\frac{\partial^2 S^x}{\partial x^2}|_{(i,j)} - \frac{d^3}{3!}\frac{\partial^3 S^x}{\partial x^3}|_{(i,j)} + \frac{d^4}{4!}\frac{\partial^4 S^x}{\partial x^4}|_{(i,j)} - \cdots \\
S^y(i+1,j) &= S^y|_{(i,j)} + d\frac{\partial S^y}{\partial y}|_{(i,j)} + \frac{d^2}{2!}\frac{\partial^2 S^y}{\partial y^2}|_{(i,j)} + \frac{d^3}{3!}\frac{\partial^3 S^y}{\partial y^3}|_{(i,j)} + \frac{d^4}{4!}\frac{\partial^4 S^y}{\partial y^4}|_{(i,j)} + \cdots \\
S^y(i-1,j) &= S^y|_{(i,j)} - d\frac{\partial S^y}{\partial y}|_{(i,j)} + \frac{d^2}{2!}\frac{\partial^2 S^y}{\partial y^2}|_{(i,j)} - \frac{d^3}{3!}\frac{\partial^3 S^y}{\partial y^3}|_{(i,j)} + \frac{d^4}{4!}\frac{\partial^4 S^y}{\partial y^4}|_{(i,j)} - \cdots
\end{aligned}\right\} \tag{5.31}$$

Similarly, the front diagonal slope values $(S^+)$ along $(i+1, j+1)$, $(i-1, j-1)$ and back diagonal slope values $(S^-)$ along $(i-1, j+1)$, $(i+1, j-1)$ can be written as

$$\left.\begin{aligned}
S^+(i+1,j+1) &= S^+|_{(i,j)} + d(\frac{\partial S^+}{\partial x} + \frac{\partial S^+}{\partial y})|_{(i,j)} + \frac{d^2}{2!}(\frac{\partial S^+}{\partial x} + \frac{\partial S^+}{\partial y})^2|_{(i,j)} + \frac{d^3}{3!}(\frac{\partial S^+}{\partial x} \\
&\quad + \frac{\partial S^+}{\partial y})^3|_{(i,j)} + \frac{d^4}{4!}(\frac{\partial S^+}{\partial x} + \frac{\partial S^+}{\partial y})^4|_{(i,j)} + \cdots \\
S^+(i-1,j-1) &= S^+|_{(i,j)} - d(\frac{\partial S^+}{\partial x} + \frac{\partial S^+}{\partial y})|_{(i,j)} + \frac{d^2}{2!}(\frac{\partial S^+}{\partial x} + \frac{\partial S^+}{\partial y})^2|_{(i,j)} - \frac{d^3}{3!}(\frac{\partial S^+}{\partial x} \\
&\quad + \frac{\partial S^+}{\partial y})^3|_{(i,j)} + \frac{d^4}{4!}(\frac{\partial S^+}{\partial x} + \frac{\partial S^+}{\partial y})^4|_{(i,j)} - \cdots \\
S^-(i-1,j+1) &= S^-|_{(i,j)} + d(\frac{\partial S^-}{\partial x} - \frac{\partial S^-}{\partial y})|_{(i,j)} + \frac{d^2}{2!}(\frac{\partial S^-}{\partial x} - \frac{\partial S^-}{\partial y})^2|_{(i,j)} + \frac{d^3}{3!}(\frac{\partial S^-}{\partial x} \\
&\quad - \frac{\partial S^-}{\partial y})^3|_{(i,j)} + \frac{d^4}{4!}(\frac{\partial S^-}{\partial x} - \frac{\partial S^-}{\partial y})^4|_{(i,j)} + \cdots \\
S^-(i+1,j-1) &= S^-|_{(i,j)} - d(\frac{\partial S^-}{\partial x} - \frac{\partial S^-}{\partial y})|_{(i,j)} + \frac{d^2}{2!}(\frac{\partial S^-}{\partial x} - \frac{\partial S^-}{\partial y})^2|_{(i,j)} - \frac{d^3}{3!}(\frac{\partial S^-}{\partial x} \\
&\quad - \frac{\partial S^-}{\partial y})^3|_{(i,j)} + \frac{d^4}{4!}(\frac{\partial S^-}{\partial x} - \frac{\partial S^-}{\partial y})^4|_{(i,j)} - \cdots
\end{aligned}\right\} \tag{5.32}$$

Using Eq. 5.31 and Eq. 5.32 and retaining terms only up to the third power (as inclusion of terms up to the third power exactly describes the improved estimation algorithm), we get

$$\left.\begin{aligned}
&S^x(i,j-1) - S^x(i,j+1) = -2d\frac{\partial S^x}{\partial x}|_{(i,j)} - \frac{2d^3}{3!}\frac{\partial^3 S^x}{\partial x^3}|_{(i,j)} \\
&S^y(i-1,j) - S^y(i+1,j) = -2d\frac{\partial S^y}{\partial y}|_{(i,j)} - \frac{2d^3}{3!}\frac{\partial^3 S^y}{\partial y^3}|_{(i,j)} \\
&S^+(i-1,j-1) - S^+(i+1,j+1) = -2d(\frac{\partial S^+}{\partial x} + \frac{\partial S^+}{\partial y})|_{(i,j)} - \frac{2d^3}{3!}(\frac{\partial S^+}{\partial x} + \frac{\partial S^+}{\partial y})|_{(i,j)} \\
&S^-(i+1,j-1) - S^-(i-1,j+1) = -2d(\frac{\partial S^-}{\partial x} - \frac{\partial S^-}{\partial y})|_{(i,j)} - \frac{2d^3}{3!}(\frac{\partial S^-}{\partial x} - \frac{\partial S^-}{\partial y})|_{(i,j)}
\end{aligned}\right\} \tag{5.33}$$

Summing all the relations of Eq. 5.33 and replacing $S^x|_{(i,j)}$, $S^y|_{(i,j)}$, $S^+|_{(i,j)}$ and $S^-|_{(i,j)}$ on the R.H.S. with $\frac{\partial \phi}{\partial x}|_{(i,j)}$, $\frac{\partial \phi}{\partial y}|_{(i,j)}$, $(\frac{\partial \phi}{\partial x} + \frac{\partial \phi}{\partial y})|_{(i,j)}$ and $(\frac{\partial \phi}{\partial x} - \frac{\partial \phi}{\partial y})|_{(i,j)}$, respectively, we get

$$\frac{d}{2}[Slope^{8adj.points}] = -3d^2\ (\tfrac{\partial^2\phi}{\partial x^2} + \tfrac{\partial^2\phi}{\partial y^2})\ |_{(i,j)}\ -\tfrac{1}{3}\mathcal{O}(\mathbf{d^4}) \tag{5.34}$$

where $Slope^{8adj.points}$ represents summation of all the slope values on the left hand sides of Eq. 5.33. Now, in a similar manner expanding the phase values $\phi(i,j)$ using Taylor series expansion at $(i,j+1)$, $(i,j-1)$, $(i+1,j)$, $(i-1,j)$, $(i+1,j+1)$, $(i-1,j-1)$, $(i-1,j+1)$ and $(i+1,j-1)$ and referring to the resultant 8 adjacent phase points as $Phase^{8adj.points}$ we have,

$$\begin{aligned}
Phase^{8adj.points} &= 8\phi(i,j) + 3d^2\ (\tfrac{\partial^2\phi}{\partial x^2} + \tfrac{\partial^2\phi}{\partial y^2})\ |_{(i,j)}\ +\tfrac{1}{4}\mathcal{O}(\mathbf{d^4})\\
8\phi(i,j) = Phase^{8adj.points} &- 3d^2\ (\tfrac{\partial^2\phi}{\partial x^2} + \tfrac{\partial^2\phi}{\partial y^2})\ |_{(i,j)}\ -\tfrac{1}{4}\mathcal{O}(\mathbf{d^4})
\end{aligned} \tag{5.35}$$

From Eq. 5.34 and Eq. 5.35, we have,

$$\begin{aligned}
8\phi(i,j) - \frac{d}{2}[Slope^{8adj.points}] &= Phase^{8adj.points} + \frac{1}{12}\mathcal{O}(\mathbf{d^4})\\
\phi(i,j) = \frac{Phase^{8adj.points}}{8} &+ \frac{d}{16}[Slope^{8adj.points}] + \frac{1}{96}\mathcal{O}(\mathbf{d^4})
\end{aligned} \tag{5.36}$$

Thus, making substitutions for $Phase^{8adj.points}$ and $Slope^{8adj.points}$, phase at the grid point $(i,j)$ can be written as

$$\begin{aligned}
\phi(i,j) \ =\ & \frac{1}{8}[\phi(i,j+1) + \phi(i,j-1) + \phi(i-1,j) + \phi(i+1,j)\\
& +\phi(i+1,j+1) + \phi(i-1,j+1) + \phi(i-1,j-1) +\\
& \phi(i+1,j-1)] + \frac{d}{16}[-S^x(i,j+1) + S^x(i,j-1) -\\
& S^y(i+1,j) + S^y(i-1,j) - S^x(i+1,j+1) -\\
& S^y(i+1,j+1) + S^x(i-1,j-1) + S^y(i-1,j-1)\\
& -S^x(i-1,j+1) + S^y(i-1,j+1) + S^x(i+1,j-1)\\
& -S^y(i+1,j-1)] + \frac{1}{96}\mathcal{O}(\mathbf{d^4})
\end{aligned} \tag{5.37}$$

Equation 5.37 is exactly similar to Eq. 5.4 that represents the improved algorithm, barring the truncation error term having order $\mathcal{O}(\mathbf{d^4})$.

Instead, if the Taylor series expansion is applied only along the horizontal and vertical directions, i.e., for grid points $(i,j+1)$, $(i,j-1)$, $(i+1,j)$ and $(i-1,j)$, we get

$$\begin{aligned}\phi(i,j) &= \frac{1}{4}\left[\phi(i-1,j)+\phi(i,j-1)+\phi(i+1,j)+\phi(i,j+1)\right]\\ &+\frac{d}{8}[S^x(i,j-1)-S^x(i,j+1)+S^y(i-1,j)\\ &-S^y(i+1,j)]+\frac{1}{12}\mathcal{O}(\mathbf{d^4})\end{aligned} \tag{5.38}$$

Equation 5.38 is exactly similar to Eq. 5.2 that represents the popular Southwell algorithm, barring the truncation error term having the order $\mathcal{O}(\mathbf{d^4})$.

It is evident from the above relation that the improved algorithm offers the same order of accuracy as that of the Southwell algorithm when Taylor series expansion is carried out at the actual grid points. However, the co-efficient of algorithm discretization error in the case of the improved algorithm is smaller by a factor of 8 in comparison to the same of the Southwell algorithm. The above expression also gives us an indication that the algorithm discretization error can be minimized by decreasing the inter grid separation, i.e., the value of $d$.

## 5.5 Experimental Implementation

We have carried out an experiment similar to the one as described in section 3.8.1 of chapter 3, to calculate the amount of error propagation in both the Southwell and improved algorithms. For the experimental arrangement, we make use of the green DPSS laser, SXGA-R2 FLCSLM and USB 3.0 CMOS camera, whose specifications have been mentioned earlier. The same computer generated holography technique [29, 30] as discussed previously is used to apply a linear combination of 2 Zernike modes, shown in Table 3.1 of chapter 3, as applied phase [65], $\phi(x,y) = 0.8Z_4$-$0.3Z_{10}$, to the reference beam. Programmability of the sensor enables to switch between various grating array dimensions of $4\times4$, $6\times6$ and $8\times8$. It is to be noted here that as the beam diameter remains the same while the grating array dimension is increased, the grid separation ($d$) decreases with the increase in grating array dimension. We then use the focal spot shift measurements to estimate the applied phase profile using zonal estimation method employing both Southwell algorithm and improved algorithm.

## 5.6 Results and Discussion

The rows (i) and (ii) of column (a) in Fig. 5.2 show the false color images of the applied phase profile $\phi(x, y)$ and its corresponding point spread function in the detector plane, respectively. The plots of the estimated phase profile based on Southwell algorithm for grating array dimensions of $4 \times 4$, $6 \times 6$ and $8 \times 8$ are shown in columns (b), (c) and (d) of row (i), while the plots of the estimated phase profile based on improved algorithm for grating array dimensions of $4 \times 4$, $6 \times 6$ and $8 \times 8$ are shown in columns (b), (c) and (d) of row (ii). All the plots shown in Fig. 5.2 are in radian units and the estimated phase points are extended to the same dimension as the applied phase, i.e., $1024 \times 1024$, using bilinear interpolation. We then compute the errors in the measured phase profiles by obtaining the root mean square (RMS) value of the difference between the applied phase profile and the corresponding estimated phase profile. The RMS error for the Southwell algorithm is found to be 0.164 $\mu$m, 0.151 $\mu$m and 0.139 $\mu$m, whereas for the improved algorithm the RMS error is found to be 0.121 $\mu$m, 0.107 $\mu$m and 0.096 $\mu$m, for grating array dimensions of $4 \times 4$, $6 \times 6$ and $8 \times 8$, respectively.

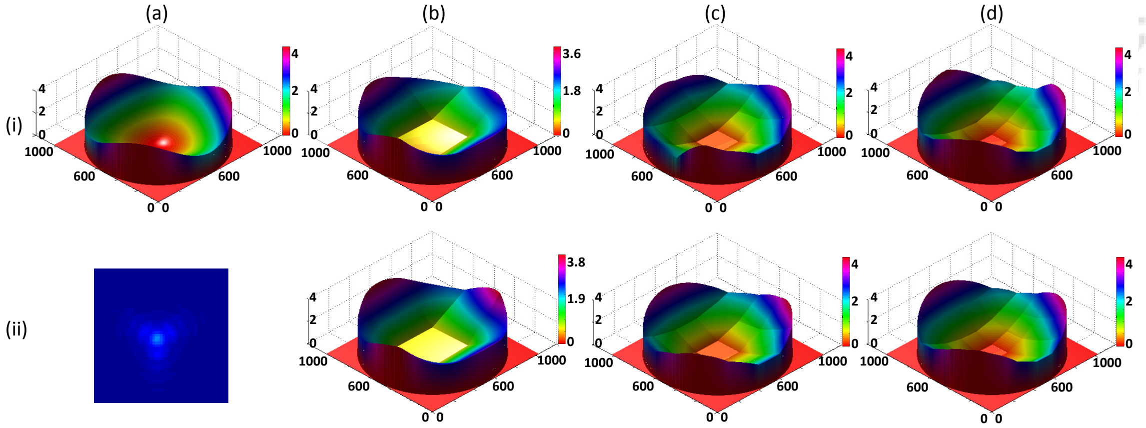

**Figure 5.2:** False color images representing the (a)(i) applied phase profile $\phi(x, y)$ and its (a)(ii) corresponding point spread function on the detector plane. Surface plots of estimated phase profile using (i)(b)-(i)(d) Southwell algorithm and (ii)(b)-(ii)(d) improved algorithm considering grating dimensions of $4 \times 4$, $6 \times 6$ and $8 \times 8$, respectively. The axis labels appearing in all the images have the unit of radian.

It is observed that the experimentally obtained RMS error decreases with the increasing grating array dimensions. This experimentally obtained RMS error is basically a contribution from the two major error terms discussed above, namely the slope measurement error and the algorithm discretization error. It is observed in section 5.4.1 that the error propagation co-efficient decreases with increasing grating array dimensions, for both Southwell and improved algorithms. Besides, the algorithm discretization error also decreases considerably with increasing grating array dimensions, as the value of $d$ is approximately, 0.80 mm, 0.53 mm and 0.40 mm for grating array dimensions of $4 \times 4$, $6 \times 6$ and $8 \times 8$, respectively and it varies as fourth power of $d$. Thus, the net contribution from both these two errors, with the increase in the array dimension, is to decrease the overall error in the estimated wavefront. Further, from sections 5.4.1 and 5.4.2 we see that both the errors are smaller in the case of the improved algorithm relative to the Southwell algorithm. The experimental results shown above is thus a validation of the theoretical results presented in this chapter.

## 5.7 Conclusion

In this chapter, we have theoretically analyzed the two important sources of error associated with the improved wavefront estimation algorithm and made a comparative study of the same with reference to the Southwell algorithm. We have derived the expressions for slope measurement error and used the same to calculate the error propagation co-efficients for various grating array dimensions, such as $4 \times 4$, $6 \times 6$ and $8 \times 8$. We have also developed the expressions for algorithm discretization error for the two algorithms. Our expressions show that even though the algorithm discretization error for the two algorithms has the same order $\mathcal{O}(\mathbf{d^4})$, the improved algorithm has a co-efficient which is 8 times smaller than the same for the Southwell algorithm. Thus, both the sources of error has less pronounced effect on the wavefront estimation if one employs the improved algorithm instead of the Southwell algorithm. The theoretical expressions also suggest that both the errors decrease as the grating array dimension of the sensing scheme increases. The results of the experiment performed also validates the theoretical expressions developed in this chapter.

## CHAPTER 6

# Grating Array Based Zonal Wavefront Sensor with Enhanced Spatial Resolution

## 6.1 Introduction

In this chapter, we introduce a scheme which can effectively improve the spatial resolution of the grating array based zonal wavefront sensor (GAWS) to a significant extent. The proposed scheme of spatial resolution enhancement is elaborately described, where we make use of a fast response ferroelectric liquid crystal spatial light modulator (FLCSLM). A quick display of several laterally shifted binary grating patterns is made possible due to the fast response of the FLCSLM device. The proposed scheme shows the enhancement in spatial resolution at a frame rate equivalent to the standard refresh rate of the video signal or even at a faster rate. We illustrate a proof-of-concept experiment to implement the proposed spatial resolution enhancement scheme. We also provide numerical simulation results that demonstrate and quantify the enhancement in spatial resolution.

## 6.2 Spatial Resolution Enhancement

Spatial resolution of the Shack-Hartmann type zonal wavefront sensor is one of the important parameter that determines the applicability of the sensor in a number of fields like optical metrology, ophthalmology, ground based telescopes, etc.

In addition to these, enhanced spatial resolution is also required for making real time corrections in wavefront distortions caused by atmospheric turbulence or other quickly varying phase profiles.

The concept of spatial resolution is graphically illustrated in Fig. 6.1, where we plot a sinusoidal function $y = asin(bx + c)$, where a, b and c are constants. The original sine wave as shown in Fig. 6.1(a) is described using sufficient number (here 31) of sampling points. Now, if we go on decreasing the number of sampling points describing the wave, then the original wave is very poorly represented. It is clear from Fig. 6.1(b)→Fig. 6.1(e) that the original wave function as shown in Fig. 6.1(a) can be more accurately represented if the number of points defining the wave is sufficient or the sampling point separation is small.

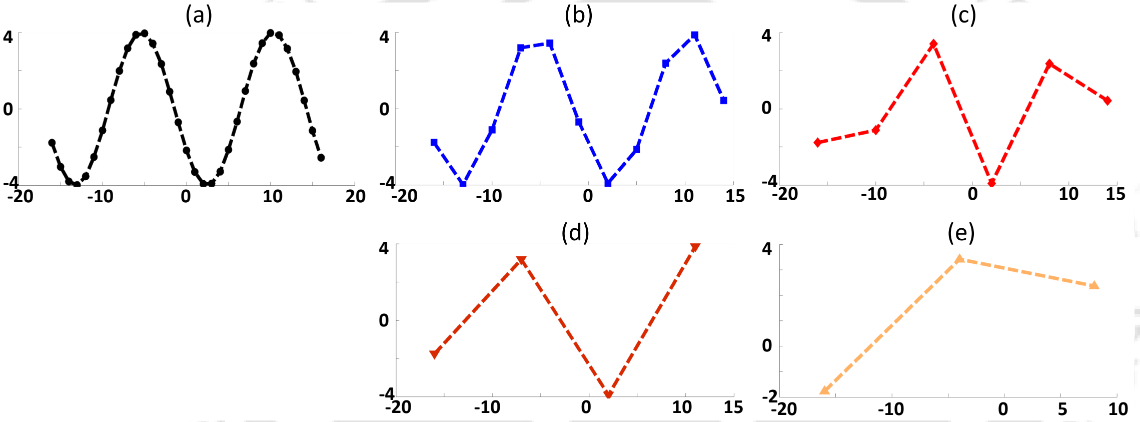

**Figure 6.1:** Graphical representation of a (a) sinusoidal wave function having more number of sampling points, whereas (b)-(e) shows similar wave function represented with relatively lesser sampling points. The horizontal and vertical axes in all the figures represent the position co-ordinate (x) and its corresponding y-value, respectively, in arbitrary unit.

## 6.3 Review of the Related Work

In the case of a conventional Shack Hartmann wavefront sensor the number of lenses used in the lenslets array dictates the spatial resolution associated with the sensor. A fixed number of lenses of a specific size used in the sampling of the incident wavefront adds rigidity to the spatial resolution associated with such sensors. The simplest way to enhance the spatial resolution of the conventional sensor would be to reduce the diameter of the lenslets used. However, this will increase the size of the diffraction-limited focal spot. Alternatively, the diameter of the lens subaperture can be reduced together with the reduction in the focal length of the lens. However, this will demand a digital camera with higher spatial resolution and also, a reduction in the focal length will reduce the sensitivity of the wavefront sensor.

So far, a number of researchers have reported various ways to increase the spatial resolution of the conventional SHWS. The spatial resolution of a SHWS can be enhanced by introducing a number of translations in the incident wavefront in two orthogonal directions relative to the lens array [94] and capturing the focal spot array in the camera for each translated position. Wavefront estimation can also be performed with enhanced spatial resolution by sequential projection of different parts of the wavefront onto a focusing lens followed by a digital camera [95, 96]. Both the aforementioned methods reduce the frame rate of the sensor and introduce inaccuracies especially in repeated measurements as they involve mechanical movement of the beam or the sensor. Lenslets with a rectangular subaperture with their axes tilted relative to the axes of the lenslets array to realise an array of Fresnel lenses [97] also introduce an enhancement in spatial resolution of the SHWS. However, the arrangement leads to the generation of crosstalk between two diagonally adjacent subapertures. An alternative method used in the implementation of the lenslets array of the SHWS involves the use of a liquid crystal spatial light modulator (LCSLM) [98], which allows non-mechanical translation of the lenslets array relative to the beam [99]. Although this arrangement increases the spatial resolution; however, it comes at the cost of sensor frame rate, as a full frame camera image is to be captured for each translation of the array. The sensor frame rate is also limited by the slow LCSLM refresh rate during the display of the grey-level patterns. The estimation of a wavefront with enhanced resolution is also reported [100] by using a combination of a rotating birefringent crystal in between two polarizers or by using an LCSLM-based variable wave-plate in the path of an appropriately polarized incident beam [101]. Both the schemes mentioned above exploit the wavefront dependent rotation of the E-vector of an elliptically polarized beam to estimate the wavefront. However, they suffer from a slow frame rate as each of the methods involves either a number of mechanical rotations or the capture of a large number of images. An effective way of estimating the wavefront of a beam is by using a lateral shearing interferometer [102]. The method can provide higher spatial resolution [103] for beams with an amplitude profile assumed to be uniform at least up to the shearing amount. It is however, not effective for light beams having quickly varying amplitude profiles.

In contrast to the state of the arts discussed above, the scheme proposed in this chapter is capable of estimating an incident wavefront with enhanced resolution [104] without compromising significantly on the sensor frame rate.

## 6.4 Methodology

In the proposed scheme, we employ a fast response FLCSLM device to display the binary hologram arrays. The FLCSLM facilities the display of color images each having 24 bit-planes at a refresh rate equivalent to that of the standard video signal. As seen in Fig. 6.2, out of the 24 bit-planes, the first 8 bit-planes (i.e., frames $B_0 \rightarrow B_7$) represent blue color, second 8 bit-planes (i.e., frames $G_0 \rightarrow G_7$) represent green color and the third 8 bit-planes (i.e., frames $R_0 \rightarrow R_7$) represent red color. A time dithering technique is used which makes it possible for each single bit of information to be displayed for a duration equal to $(1/24)^{th}$ the duration of one color image. As one single bit-plane can represent a single binary grating array, it is possible that 24 separate binary grating array patterns are represented by a single color image. Thus, using the FLCSLM, 1440 grating arrays can be displayed in one second for a color image refresh rate of 60 Hz. In this scheme, we employ the 24 bit-planes of each color image to facilitate the display of equal number of laterally shifted binary diffraction grating arrays. The lateral shift of the grating pattern can be either in the horizontal direction or in the vertical direction, or in both the directions. The focal spot array for each laterally shifted grating patterns is to be captured. This can be achieved by configuring the grating patterns to generate fewer or only a single row of focal spots [59] (in the unaberrated case) in the detector plane so that there is an enhancement in the detector frame rate [78].

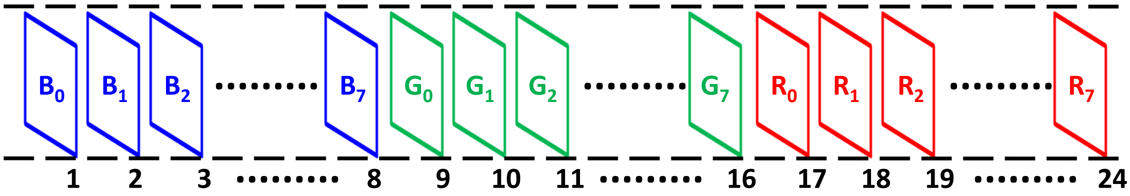

**Figure 6.2:** The 24 bit-planes that represent a color image to be displayed on the FLC-SLM.

Figure 6.3 is an illustration of the outline of sixteen representative adjacent grating elements in which the bigger circle indicate the grating subaperture and the smaller filled circle indicate the geometrical centre. The black filled circles correspond to the grating patterns in the first bit-plane (denoted as 1 bp where 1 is the bit-plane index). The translation of the centre of the top-left grating element (along horizontal and vertical directions) is done using 8 bit-planes with the corresponding positions indicated by eight filled colored circles. In the case of Fig. 6.3, it is assumed that 9 bit-planes (i.e., 1 bp to 9 bp) will make a sequential display of 9 binary grating arrays each laterally shifted from the others. Another important assumption related to our proposed scheme is that the grating element is not allowed to cross the outline described by the original grating array (i.e., corresponding to 1 bp). Thus, using 9 bit-planes, a grating array of initial dimension $4 \times 4$ results in a cumulative zone dimension of $10 \times 10$. This results in estimating the wavefront from $10^2$ number of slope measurements as against from $4^2$ number of slope measurements. The cumulative zone dimension obtained as a function of initial grating array dimension of $N \times N$ and net number of bit-planes, denoted as $b = n^2$, where n is an integer, can be written as $\left[(N-1)\sqrt{b}+1\right] \times \left[(N-1)\sqrt{b}+1\right]$.

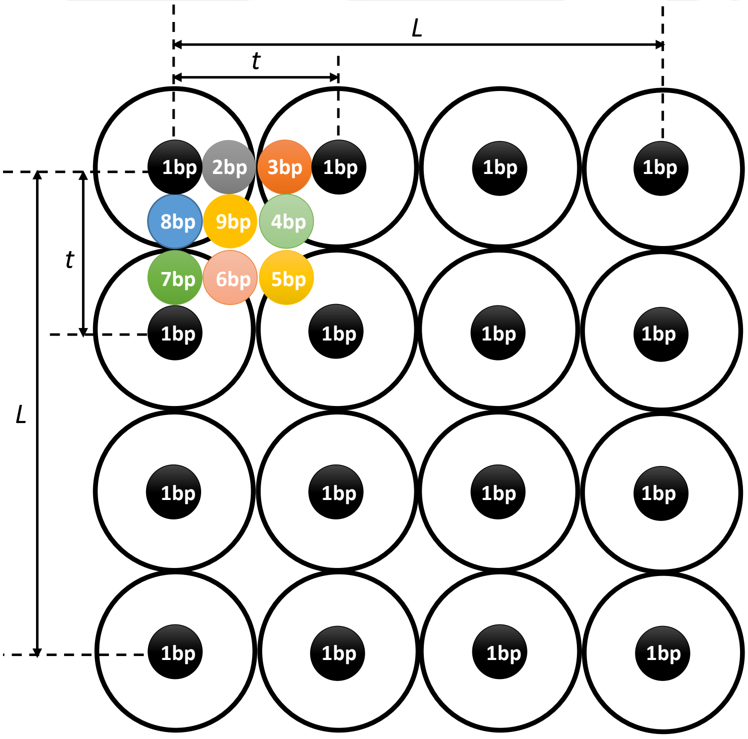

**Figure 6.3:** Representative model showing the effective hologram scan positions with an initial dimension of $4 \times 4$ using 9 bit-planes.

Thus, for $b > 1$ the sensor frame rate $F_s$ in the proposed scheme, is defined as $\frac{1}{\tau_b}$, where $\tau_b$ is the net display time for $b$ number of bit-planes. This is possible as

| | | | **Cumulative Zone Dimension** | | | | |
|---|---|---|---|---|---|---|---|
| **Sl. No.** | **Bit-planes ($b$)** | **Frequency ($F_s$)** | **N = 2** | **N = 3** | **N = 4** | **N = 6** | **N = 8** |
| 1. | 4 | 360 Hz | 3×3 | 5×5 | 7×7 | 11×11 | 15×15 |
| 2. | 9 | 160 Hz | 4×4 | 7×7 | 10×10 | 16×16 | 22×22 |
| 3. | 16 | 90 Hz | 5×5 | 9×9 | 13×13 | 21×21 | 29×29 |
| 4. | 25 | 58 Hz | 6×6 | 11×11 | 16×16 | 26×26 | 36×36 |
| 5. | 36 | 40 Hz | 7×7 | 13×13 | 19×19 | 31×31 | 43×43 |
| 6. | 49 | 30 Hz | 8×8 | 15×15 | 22×22 | 36×36 | 50×50 |
| 7. | 64 | 23 Hz | 9×9 | 17×17 | 25×25 | 41×41 | 57×57 |
| 8. | 81 | 18 Hz | 10×10 | 19×19 | 28×28 | 46×46 | 64×64 |
| 9. | 96 | 15 Hz | 11×11 | 21×21 | 31×31 | 51×51 | 71×71 |

**Table 6.1:** Table showing the cumulative grating array dimension obtained following the proposed scanning method as a function of $N$ initial grating array dimension considered and $b$ number of bit-planes employed.

the proposed scheme has the capability to capture all $b$ focal spot arrays either in a single camera frame or in multiple camera frames within the stipulated time $\tau_b$, which is again due to the enhanced camera frame rate with the reduction in the number of focal spot rows. However, for $b = 1$, $F_s$ will be same as the camera frame rate. In Table 6.1, we show some of the exemplary cumulative zone dimensions obtained as a function of $N$, $b$ and $F_s$

## 6.5 Experimental Implementation

Figure 6.4 shows the schematic diagram of the experimental arrangement involved in the implementation of proposed spatial resolution enhancement of a GAWS setup. A lens combination of $L_1$ and $L_2$ is used to expand and collimate the beam from the green diode-pumped solid state (DPSS) laser, emitting at $\lambda$=532 nm, before it is incident on the FLCSLM panel that displays the binary grating array pattern.

We make use of the SXGA-R2 FLCSLM having refresh rate of 60 Hz. The light diffracted by the grating pattern displayed on the FLCSLM is collected by a third lens $L_3$. Another lens $L_4$ along with an iris diaphragm ID is used to separate the +1 order beams from the other diffracted orders. An in-house developed electronic control unit synchronizes the FLCSLM display and the camera exposure time. We use the same computer generated holography technique [29, 30] described previously to design the grating array pattern. It is to be noted that each grating element is basically a binary hologram that can carry a user defined phase profile in the corresponding +1 order diffracted beam. The spatial frequencies of each of the

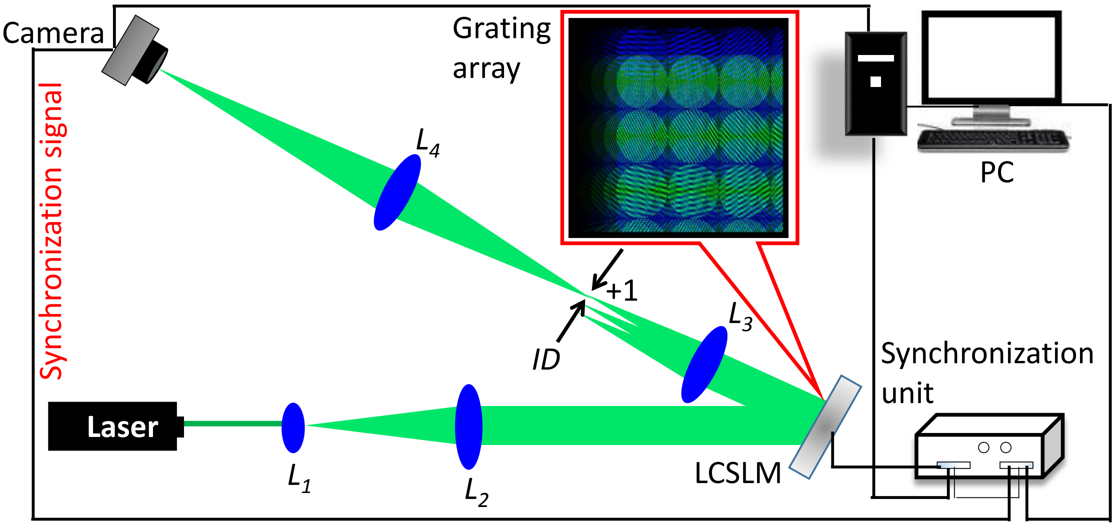

**Figure 6.4:** The experimental arrangement of the grating array based zonal wavefront sensor to implement the spatial resolution enhancement technique.

grating element in the array are configured according to Eq. 3.19 of chapter 3 to produce a one-dimensional array of +1 order beams that corresponds to an incident beam aberrated with a certain amount of a Zernike mode aberrations [65]. Initially, $b$ number of binary hologram arrays are digitally constructed with lateral shifts as per the scheme shown in Fig. 6.3. These $b$ number of binary hologram arrays are then combined to construct as many bit-planes of a single 24 bit color image for a case where $b \leq 24$ and more than one 24 bit color images for $b > 24$. The 24 bit color images are then sent to the FLCSLM panel so that each of $b$ number of bit-planes are sequentially displayed.

Figure 6.5(a)-Fig. 6.5(c) show the color images containing laterally shifted grating patterns with $b = 4$, 9, and 16, respectively, with the original grating array having a dimension 3 × 3. Each grating array is designed to generate only one row of +1 order focal spots, in the unaberrated case. Figure 6.5(d)-Fig. 6.5(f) show the cumulative +1 order focal spots due to the entire $b$ number of shifted grating arrays for $b = 4$, 9 and 16, respectively. Grating array corresponding to each of $b$ bit-planes is incorporated with a vertical tilt so that the resulting +1 order focal spot arrays in the detector plane are vertically shifted. This enables capturing the focal spots of all the laterally shifted grating array patterns in one camera frame only. The same number of shifted arrays in the case of the conventional SHWS would have required capturing of a number of images equal to the number of shifted arrays. Thus, the proposed scheme facilitates capturing of focal spots of shifted arrays at a rate faster

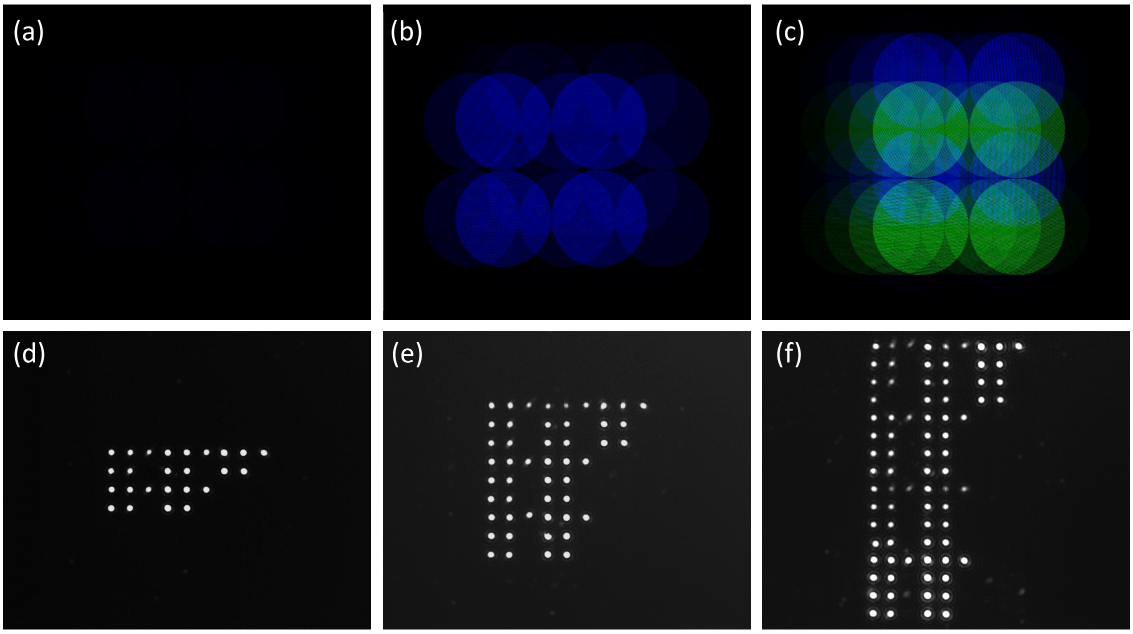

**Figure 6.5:** Color images containing the laterally shifted grating array patterns of initial dimension 3 × 3, using (a) 4 bit-planes, (b) 9 bit-planes and (c) 16 bit-planes of a color image, and its corresponding focal spots having (d) 4 rows, (e) 9 rows and (f) 16 rows, obtained experimentally.

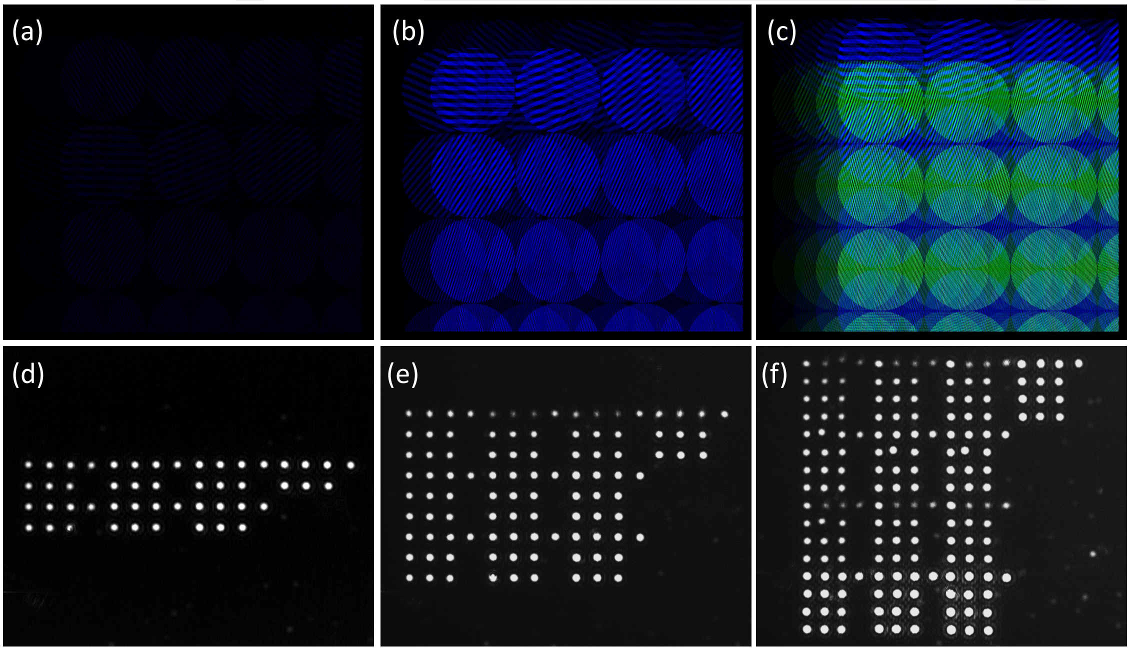

**Figure 6.6:** Color images containing the laterally shifted grating array patterns of initial dimension 4 × 4, using (a) 4 bit-planes, (b) 9 bit-planes and (c) 16 bit-planes of a color image, and their corresponding focal spots having (d) 4 rows, (e) 9 rows and (f) 16 rows, obtained experimentally.

than the conventional sensor even using a low frame rate camera. It is noticed that some of the focal spot rows have less than 9 focal spots in them. The missing focal spots correspond to the grating elements which have crossed the outline of the original grating array. Figure 6.6(a)-Fig. 6.6(c) show the color images containing the laterally shifted grating array patterns corresponding to $b$ = 4, 9 and 16, respectively, for a grating array of original dimension $4 \times 4$. The resulting +1 order focal spot arrays as captured by the camera are shown in Fig. 6.6(d)-Fig. 6.6(f).

## 6.6 Results and Discussion

Color images are constructed by combining laterally shifted binary grating array patterns considering initial dimension of $4 \times 4$, and $b$ = 1, 4, 9 and 16. The $b$ = 1 estimation is denoted as low spatial resolution (LSR) and $b$ = 4, 9, and 16 are denoted as high spatial resolution (HSR). Wavefronts are estimated by employing the improved wavefront estimation algorithm, discussed in section 4.4 of chapter 4. Initially, the incident laser beam is aberrated with a Zernike mode $Z_4$ of RMS amplitude 1 radian. Figure 6.7(i)(a) shows the false color image of the applied phase profile, and Fig. 6.7(i)(b)-Fig. 6.7(i)(e) show the corresponding estimated phase profiles in the LSR and HSR cases. Figure 6.7(ii) shows the line plots of the phase profiles in Fig. 6.7(i) along the line shown in Fig. 6.7(i)(a).

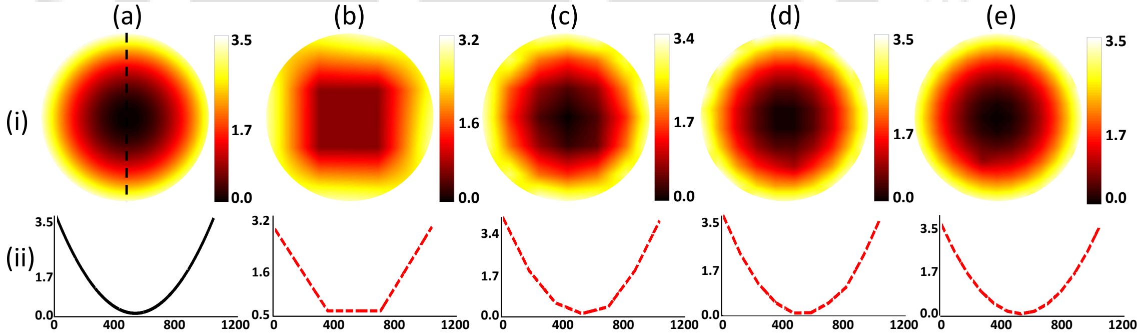

**Figure 6.7:** False color images representing the (i)(a) applied phase profile of Zernike mode $Z_4$ and its corresponding estimated phase profile (i)(b) for the LSR case, and in the HSR cases (i)(c) with bit-planes = 4, (i)(d) with bit-planes = 9 and (i)(e) with bit-planes = 16. The line plots of all the images shown in (i)(a) along the dashed line is illustrated in (ii) (a)-(e). The axis labels appearing in all the images have the unit of radian.

We then aberrate the incident beam using a linear combination of 3 different Zernike modes, such that the resultant phase profile of the beam is expressed as

| Sl. No. | Zernike Mode Applied | RMS Error (in micron) | | | |
|---|---|---|---|---|---|
| | | b = 1 | b = 4 | b = 9 | b = 16 |
| 1. | $Z_4$ | 0.068 | 0.041 | 0.026 | 0.019 |
| 2. | $Z_c$ | 0.083 | 0.056 | 0.035 | 0.027 |

**Table 6.2:** Table showing the measured rms error for both the LSR (i.e., $b = 1$) and HSR (i.e., $b = 4$ 9, and 16) cases due to the incorporation of Zernike modes, $Z_4$ and the combination $Z_c$.

$Z_c$=-0.6$Z_6$+0.5$Z_7$-0.3$Z_{11}$. Figure 6.8(i)(a) shows the false color images of the applied phase profile $Z_c$. The corresponding estimated phase profile in the LSR case (i.e., $b$=1) is shown in column (b) of Fig. 6.8(i), and the profiles in the case of HSR corresponding to $b = 4$, 9 and 16 are shown in columns (c), (d) and (e), respectively, of Fig. 6.8(i). The line plots of all the phase profiles along the dashed line in Fig. 6.8(i)(a) are shown in Fig. 6.8(ii)(a)-Fig. 6.8(ii)(e). All the plots in Fig. 6.7 and Fig. 6.8 are expressed in radian units and the estimated phase profiles are presented after bilinearly interpolating the phase points to the same dimension as the applied phase profile, i.e. 1024 × 1024. The differences between the applied phase profile and the corresponding estimated phase profiles are used to compute the root mean square (RMS) errors of wavefront estimation. Table 8.1 shows the RMS errors of wavefront estimation obtained for the LSR (i.e., $b$=1) case as well as for the HSR (i.e., $b$ = 4, 9 and 16) cases.

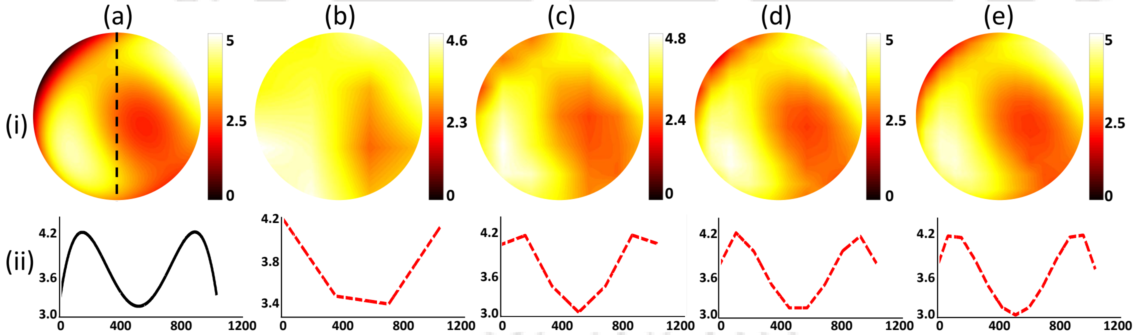

**Figure 6.8:** False color images representing the (i)(a) applied phase profile of Zernike combination $Z_c$ and its corresponding estimated phase profile (i)(b) for the LSR case, and in the HSR cases (i)(c) with bit-planes = 4, (i)(d) with bit-planes = 9 and (i)(e) with bit-planes = 16. The line plots of all the images shown in (i)(a) along the dashed line is illustrated in (ii) (a)-(e). The axis labels appearing in all the images have the unit of radian.

The use of $b$ = 4, 9 and 16, in the HSR cases, has increased the number of phase estimation points to 49, 100 and 169, respectively, in comparison to 16 phase estimation points in the LSR case. A comparison of both the surface plots and line plots shown in Fig. 6.7 and Fig. 6.8 in the LSR case (i.e., $b = 1$), with that in the HSR (i.e., $b = 4$, 9 and 16) cases reveals that the spatial wavefront features are more accurately represented in the HSR case. It is further noticed that the increasing number of bit-planes in the HSR cases leads to a reduction in the RMS error of wavefront estimation.

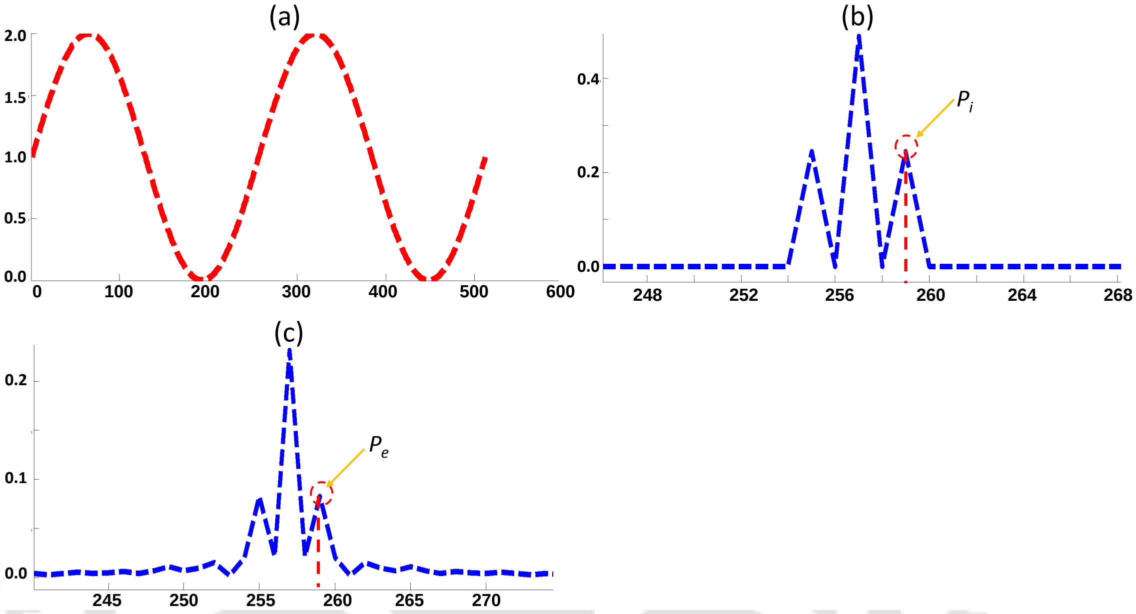

**Figure 6.9:** The sine-like (a) incident wavefront and its (b) corresponding Fourier transform, while (c) represents the Fourier transform of the estimated wavefront employing $b = 4$ and initial dimension of $4 \times 4$. The horizontal and vertical axes, in figure (a) represents the pixel size (say, p) and the phase value (say, a) of the sine-like incident wavefront in the hologram plane, respectively. The horizontal and vertical axes, both in figure (b) and (c) have the unit of 1/p and 1/a, respectively, in the Fourier plane.

We also perform a numerical simulation to quantify the improvement in spatial resolution of the proposed scheme. We consider an incident wavefront to have a sine-like wave profile with spatial frequency described using the unit of $\nu_0 = \frac{1}{D}$, where $D$ is the diameter of a single grating subaperture. Figure 6.9(a) shows such sine-like incident wavefront with $\nu_0 = 0.5$. An array of $4 \times 4$ grating patterns are digitally constructed which are then aberrated with the sine-like incident wavefront. The array of +1 order focal spots are obtained by taking the Fourier transform of the corresponding aberrated grating array pattern of dimension $4 \times 4$. The laterally shifted grating array patterns are realised as per the scheme described in Fig. 6.3 corresponding to $b = 1$, 4, 9 and 16. The focal spot shifts corresponding to the aberrated incident wavefront are computed to estimate the incident wavefront as per the description given in section 4.4 of Chapter 4. The Fourier transform of the incident wavefront is performed and the peak value of the first harmonic in the frequency plane, at the location $\nu_{sf}$, is recorded as $P_i$. Similarly, the peak value at the same location, $\nu_{sf}$ in the frequency plane of the estimated wavefront is recorded and the same is denoted as $P_e$. Representative results of such operation for the incident wavefront and the estimated wavefronts corresponding to $b = 4$, are shown in Fig. 6.9(b) and Fig. 6.9(c), respectively. We then evaluate the ratio $R = \frac{P_e(\nu_{sf})}{P_i(\nu_{sf})}$, that determines the magnitude of sine-like wavefront present in the estimated wavefront corresponding to $b = 1$, 4, 9 and 16 for each sine wave of spatial frequency $\nu_{sf}$. The line plots of the ratio $R$ against the spatial frequency $\nu_{sf}$ of the incident sine-like wavefront is shown in Fig. 6.10. From the graph, it is clear that the magnitude of the sine-like wavefront present in the estimated phase profile increases with the increase in $b$. For instance, the increase in the strength of the spatial frequency for $b = 16$ (HSR case) is more than 2.5 times the strength for $b = 1$ (LSR case). However, the overlap of the laterally shifted grating array patterns result in a low-pass filtering effect, which eventually decreases the absolute strength of the spatial frequency, as $\nu_{sf}$ increases. It may be possible to recover some of the higher spatial frequency components by performing a deconvolution [105] of the overlap of the known grating subapertures. The process of deconvolution will help in compensating the degradation of the focal spots caused, due to the overlap of various grating subapertures with the increase in spatial frequency $\nu_{sf}$.

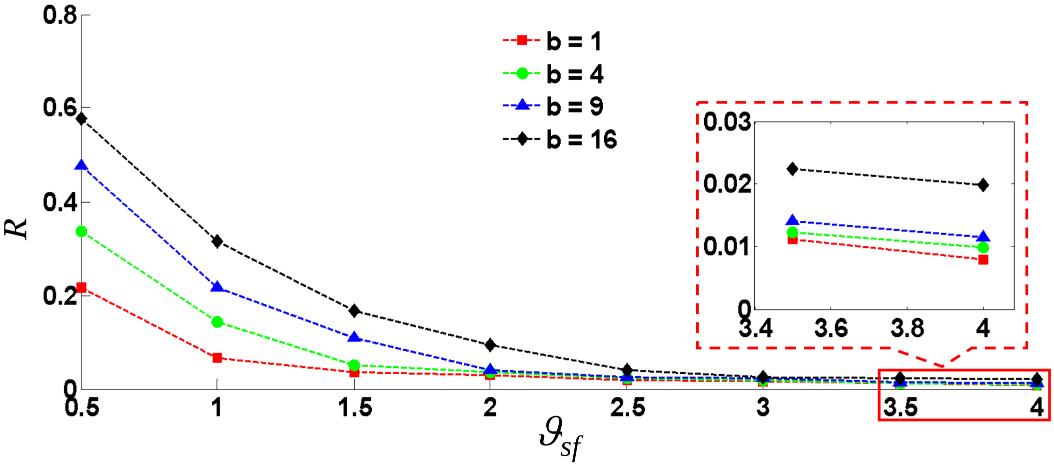

**Figure 6.10:** Plots of the ratio $R$ versus the spatial frequency $\nu_{sf}$, in the unit of $\nu_0 = \frac{1}{D}$ ($D$ being the diameter of a single grating subaperture) of the sine wave-like incident wavefront corresponding to $b = 1$, 4, 9, and 16.

## 6.7 Conclusion

In this chapter, a scheme to enhance the spatial resolution of a grating array based zonal wavefront sensor is introduced by using a sequence of binary grating patterns shifted laterally, realised with the help of the 24 bit-planes display of an FLCSLM. The grating arrays are programmably configured to generate a camera-specific focal spot array so that the camera can capture all the focal spot arrays of the complete sequence without being affected by the typical frame rate of the camera. Thus, wavefronts can be measured with enhanced spatial resolution and without compromising much on the sensor frame rate. The working of the proposed scheme is demonstrated experimentally for $b = 1$, 4, 9 and 16. Enhancement in the spatial resolution and the subsequent decrease in the RMS error of wavefront estimation are observed with the increase in the number of bit-planes used. Experimental results demonstrate that the proposed scheme can detect spatial wavefront features that would have been missed by the conventional method. The relative enhancement in the spatial resolution with increasing number of bit-planes has also been demonstrated and quantified by the numerical simulations shown in the present chapter.

# CHAPTER 7

# Grating Array Based Zonal Wavefront Sensing with Improved Centroid Detection Accuracy

## 7.1 Introduction

In this chapter, we propose a scheme to improve the accuracy of centroid detection in the grating array based zonal wavefront sensor (GAWS) by using more than one digital camera via a beam splitting mechanism. We provide a brief description about the generation of multiple sub-arrays of focal spots which are to be captured by using multiple cameras. We illustrate a proof-of-concept experiment to implement the proposed scheme of enhanced centroid detection accuracy. We present experimental results that demonstrate describing each of the focal spots over a larger detector subaperture area. The proposed scheme shows improvement in centroid detection accuracy for different grating array dimensions, without any post acquisition processing of the data. We also show that the same experimental arrangement can enhance the dynamic range of the sensor and reduce the possibility of crosstalk between adjacent zones. Further, we also demonstrate the capability of the proposed scheme to estimate an incident wavefront more accurately, due to the improvement in centroid detection accuracy.

## 7.2 Centroid Detection Accuracy

The accuracy of a Shack-Hartmann type zonal wavefront sensor to measure the incident wavefront depends on the accuracy [106, 107] with which each focal spot in the detector plane is located. The focal spot position can be obtained by using any of the centroid detection algorithms [108]. However, the centre of mass algorithm is considered to be the standard and widely used centroid detection algorithm, on the basis of the robustness, fast and easy implementation [109, 110]. In the centre of mass algorithm, a focal spot position is detected by taking the ratio of sum of the product of co-ordinates of all pixels (defining the spot) and their corresponding intensity values, to the total intensity value within a detector subaperture area [111]. Therefore, it is also known as the statistical averaging algorithm. It is to be noted that such an expression to find the centre of mass has already been discussed in section 2.3.1 of chapter 2. However, the performance of the centre of mass algorithm is found to be dependent on the distribution of the detector noise. It is found to be more sensitive towards noise when the focal spot area (within the full width at half maximum) is relatively small in comparison to the detector subaperture area [112]. Such a sensitivity to noise on the other hand is a consequence of the discrete and limited sampling of the intensity distribution of the focal spot captured by the detector. However, it is possible to increase the accuracy in the detection of centroid position by increasing the number of detector pixels within each focal spot. In other words, if the focal spot is defined over a fairly large number of pixels considering a larger detector subaperture area, the centroid detection accuracy can be comparatively improved.

## 7.3 Review of the Related Work

As mentioned earlier, the accuracy in focal spot centroid detection is a key factor to decide the accuracy of wavefront estimation in a Shack-Hartmann type wavefront sensor. Thus, it is another important aspect that needs to be considered, which is also evident from the number of related scientific literatures in the recent times. To improve the centroid detection accuracy in a SHWS, the focal spots are expected to be defined with a full width at half maximum which is much larger than the size of a single pixel of the detector. To satisfy the afore mentioned condition, a detector with a large number of pixels has to be used for imaging the focal spots. However, fixed number of pixels describing the sensor area of a digital camera (here camera and detector are used to denote the same device) puts an upper limit in the centroid detection accuracy in the conventional SHWS.

There have been reports on methods which can be effectively used to make the centroid detection more accurate. There are also attempts to reduce the adverse effect of noise in the standard centre of mass algorithm by suppressing the irrelevant noisy pixels of the detector. Such methods include applying weighting function [110, 113, 114, 115] and thresholding the detector pixel values [112, 116, 117, 118]. However, applying a weighting function or suppressing certain pixel information by applying a threshold value may result in a bias shift of the estimated centroid position, especially while dealing with an asymmetric focal spot [108, 109, 119]. To further reduce the effect of noise without the use of thresholding or weighting function, Fourier domain centroiding method [111, 120] was proposed. It is based on the detection of the phase shift between the reference image and the measured image in the Fourier domain. Although, the method shows good results for point-like spot; however, it is not readily applicable to other asymmetric spots [121]. Besides processing of the images in the Fourier domain (using Discrete Fourier Transform) requires more computational time. It has also been reported that accurate centroid detection can be performed by using least-square method [122]. In such method, gradient of an intensity function is fitted using an orthogonal polynomial function by least-square means. However, such method requires complex computing, and thus a better performance can be expected at the cost of computational time only. P. Arulmozhivarman et al. [122] presented a wavelet-based approach in a SHWS to compute the moments of a region by using a set of basis functions. Although the wavelet-based method provides superior result, but such a method has limitations in the case of dynamically varying focal spot positions. Also, the use of wavelet transform depends on proper selection of the wavelet basis function and requires more computational power. S. A. Sallberg et al. proposed [123] maximum a posteriori estimator (MPE) to improve the centroid detection algorithm in a SHWS by incorporating a priori knowledge of the wavefront tilt. However, only a few algorithms are found to be iterative to compute the MPE and there exist possibilities to obtain no minimum or several minima in the likelihood function. Therefore, most of the methods discussed above showed improvement in centroid detection accuracy, over the centroid detection algorithms, although, they require extensive pre-processing or post-processing of the data which significantly increases the computational time.

Crosstalk in a SHWS between adjacent detector subapertures also adversely affects the accurate detection of the focal spot centroid position. It can be reduced by expanding the detector subaperture areas. However, such expansion may put a limit on the spatial resolution achievable with the SHWS. Sequential projection of small portions of the wavefront [95] or sequential blocking of the lenslets array [124, 125] can also minimize the effect of crosstalk, thereby increasing the accuracy and dynamic range of the sensor. Unfortunately, here the operations in a sequential manner significantly reduce the frame rate of the sensor. Crosstalk can also be minimized through apodisation of the fabricated lenslets array [126]. However, apodisation of the lenslets array is quite tedious to realise in actual practice. Further, there are reports which suggest that numerical deconvolution [105] of the captured focal spot pattern can help to recover the information degraded due to crosstalk. However, deconvolution is a time consuming process and it produces acceptable results only if there is a lesser overlap between the spots [127].

In view of the above limitations in the state of the art to improve the centroid detection accuracy and to reduce the crosstalk or to improve the dynamic range of the sensor, we propose a scheme for the GAWS by employing a beam splitting mechanism that defines each of focal spot over a larger detector subaperture area. This is made possible by the programmability of the GAWS that facilitates the use of more than one digital camera to record the focal spots by splitting a single array of focal spots into multiple sub-arrays. The proposed method improves the centroid detection accuracy or reduces the crosstalk without performing any pre-processing or post-processing of the data.

## 7.4 Design of Binary Grating Arrays

We first consider an array of 4×4 binary diffraction gratings as discussed in section 3.6 of Chapter 3. Assuming $\Delta f_{0x} = \Delta f_{0y}$ in Eq. 3.18 of Chapter 3 results in a type of binary grating pattern as shown in Fig. 7.1 (i)(a). Such a type of binary grating pattern produces a regularly spaced focal spot array in the unaberrated case as shown in Fig. 7.1 (ii)(a), which can be captured using a single camera.

We then define the spatial frequencies of the grating element $(i, j)$, with similar

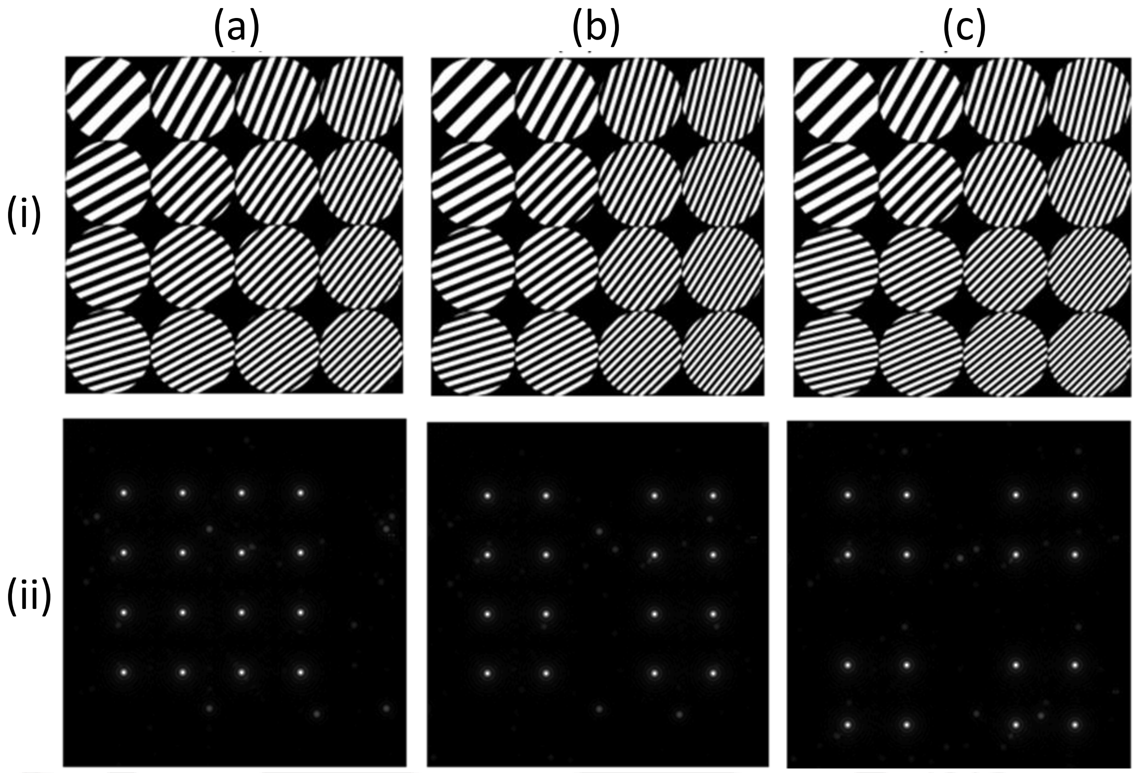

**Figure 7.1:** The three different types of grating patterns, (i)(a) type-A, (i)(b) type-B and (i)(c) type-C and the corresponding focal spots comprising (ii)(a) a single array, (ii)(b) two sub-arrays and (ii)(c) four sub-arrays, respectively.

meaning of the variables as described in section 3.6 of Chapter 3, as

$$\left.\begin{array}{r} f_{0x}^{i} = \begin{cases} f_{0x}^{1} + (i-1)\times \Delta f_{0x} & (if\ i<k) \\ f_{0x}^{1} + \Delta f^{1} + (i-1)\times \Delta f_{0x} & (if\ i\geq k) \end{cases} \\ f_{0y}^{j} = f_{0y}^{1} + (j-1)\times \Delta f_{0y} \end{array}\right\} \tag{7.1}$$

or

$$\left.\begin{array}{r} f_{0x}^{i} = f_{0x}^{1} + (i-1)\times \Delta f_{0x} \\ f_{0y}^{j} = \begin{cases} f_{0y}^{1} + (j-1)\times \Delta f_{0y} & (if\ j<k) \\ f_{0y}^{1} + \Delta f^{1} + (j-1)\times \Delta f_{0y} & (if\ j\geq k) \end{cases} \end{array}\right\} \tag{7.2}$$

Considering Eq. 7.1 and choosing $k = \frac{N}{2}$, results in another type of binary grating pattern as shown in Fig. 7.1 (i)(b), using $N$=4. The corresponding focal spots for such type of binary grating pattern comprises two sub-arrays of focal spots, separated along the X direction as shown in Fig. 7.1 (ii)(b). The separation in the X direction facilitates splitting the two sub-arrays using a beam splitter and directing them to two cameras for wavefront estimation. Lack of such a separation will result in loss of slope information corresponding to the extreme right column and the extreme left column of the left and right focal spot sub-arrays, respectively. The two sub-arrays of focal spots may also be separated along the Y direction for a similar type of binary grating pattern, if we consider Eq. 7.2.

We can also define the spatial frequencies of the grating element $(i, j)$ as,

$$\left.\begin{aligned} f_{0x}^{i} &= \begin{cases} f_{0x}^{1} + (i-1) \times \Delta f_{0x} & (if\, i < k) \\ f_{0x}^{1} + \Delta f_{0x}^{1} + (i-1) \times \Delta f_{0x} & (if\, i \geq k) \end{cases} \\ f_{0y}^{j} &= \begin{cases} f_{0y}^{1} + (j-1) \times \Delta f_{0y} & (if\, j < l) \\ f_{0y}^{1} + \Delta f_{0y}^{1} + (j-1) \times \Delta f_{0y} & (if\, j \geq l) \end{cases} \end{aligned}\right\} \tag{7.3}$$

where $\Delta f^{1}$, $\Delta f_{0x}^{1}$ and $\Delta f_{0y}^{1}$ are real numbers and $(k,\ l)$ are integers in between 1 and $N$. Considering Eq. 7.3 and choosing $\Delta f_{0x}^{1} = \Delta f_{0y}^{1}$ and $k = l = \frac{N}{2}$, gives rise to another type of binary grating pattern as shown in Fig. 7.1 (i)(c). The corresponding focal spots comprise four sub-arrays of focal spot, separated along both X direction and Y direction as shown in Fig. 7.1 (ii)(c), which can be captured simultaneously using four cameras. In this work, we denote the three types of binary grating pattern shown in Fig. 7.1 (i)(a) → Fig. 7.1 (i)(c) (designed using Eq. 3.18 Eq. 7.1 or Eq. 7.2 and Eq. 7.3) as type-A, type-B and type-C binary grating pattern, respectively.

## 7.5 Experimental Implementation

The schematic diagram of the experimental arrangement to improve the accuracy in centroid detection is shown in Fig. 7.2. Light beam from a green DPSS laser is expanded and collimated using the two lenses $L_1$ and $L_2$ to be incident on the SXGA-R2 FLCSLM. Initially, we display a type-C binary grating pattern (designed using Eq. 7.3) on the display panel of the LCSLM. The $+1$ diffraction orders are isolated using the lens $L_3$ and the iris diaphragm $ID$. The $+1$ order diffracted beams are then allowed to be incident on a mirror $M$, after the lens $L_4$ as seen in Fig. 7.2. The experimental arrangement after the mirror $M$ is shown within the red dotted box for better visual clarity. The mirror is kept at $45^{0}$ angle with the lens $L_4$ optical axis to direct the beams vertically downward towards a prism beam splitter $BS_1$. The prism beam splitter is a knife-edge right-angle prism having 25 mm × 25 mm reflective surfaces. Two other prism beam splitters $BS_2$ and $BS_3$ are positioned horizontally on the two sides of $BS_1$. The distance between $BS_1$ and $BS_2$ or $BS_3$ is kept at the minimum such that the lens $L_4$ refocuses the $+1$ order diffracted beams in a plane equidistant between $BS_1$ and $BS_2$ or $BS_1$ and $BS_3$. This ensures that the beams corresponding to the two pairs of focal spot arrays separated along X are accommodated with the reflecting surfaces of $BS_1$ and the beams from each of the sub-arrays separated along Y are incident on the reflecting surfaces of $BS_2$ and $BS_3$. Four lenses, $L_5$, $L_6$, $L_7$ and $L_8$ focus the four sub-arrays of $+1$ order beams onto four camera positions, Cam-1, Cam-2, Cam-3 and Cam-4, respectively. Each of the four cameras record both the reference as well as the shifted focal spot positions. The data from the four cameras are then combined in the PC to estimate the wavefront in a similar way as discussed before. It is to be mentioned that similar to the previous cases, the programmability of the sensor enables to switch between grating array dimensions such as between $4 \times 4$ and $8 \times 8$. Thus, the beam splitting arrangement and the use of four cameras increase the resultant number of camera pixels for each focal spot and detector subaperture area. In case of grating pattern of type B, beam splitting by $BS_2$ and $BS_3$ are not required. In such a case two lenses are placed in the two beam paths after $BS_1$ to focus the two sub-arrays of $+1$ order beams onto two cameras.

The present experimental arrangement shows the generation of four sub-arrays of focal spots; however, the proposed scheme can also be extended to generate more than four sub-arrays of focal spots.

## 7.6 Results and Discussion

We perform the experiment corresponding to the type-C grating pattern using two cameras only. For the same set of reference and shifted focal spots, the cameras are once placed at Cam-1 and Cam-2 positions and then at Cam-3 and Cam-4 positions. Here, we provide experimental results due to both type-A and type-C grating pattern for each of the grating array dimensions of $4 \times 4$ and $8 \times 8$. The arrays of focal spots due to the type-A and type-C grating patterns having a dimension of $4 \times 4$ are shown in Fig. 7.3. Figure 7.3 (a) shows the single array of focal spots due to the type-A grating pattern that is captured using a single camera, whereas Fig. 7.3 (b)$\rightarrow$ Fig. 7.3 (e) show the four sub-arrays of focal spots due to the type-C grating pattern, captured using four cameras. Each of the focal spots captured using a single camera is defined over a detector subaperture length $(D)$ of 158 pixels. We have estimated

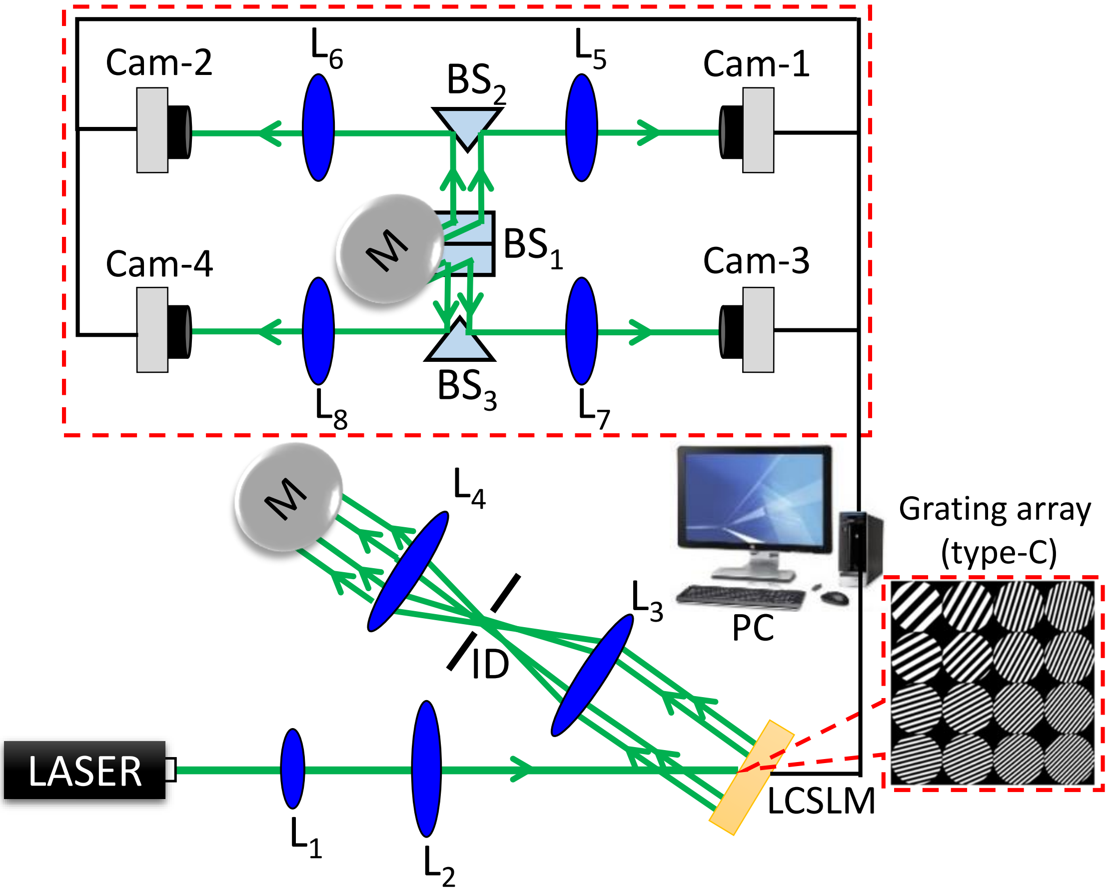

**Figure 7.2:** The experimental arrangement of the proposed scheme to use multiple cameras in a wavefront sensor by employing a beam splitting mechanism.

the full width at half maximum (FWHM) of each focal spot, and the average FWHM ($d$) is found to be ~11 pixels. However, each of the focal spots captured using four cameras is defined over a detector subaperture length ($D$) of 458 pixels and the value of FWHM ($d$) of each focal spot on the average is ~31 pixels. The ratio $R = \frac{d}{D}$ is found to be 0.069 in the case of the single array of focal spots and 0.067 in the case of four sub-arrays of focal spots. Thus, the enhancement of centroid detection accuracy in the case of the type-C grating pattern relative to the type-A grating pattern can be assessed while maintaining almost a constant ratio ($R$) in both the cases. Figure 7.4 (i)(a) shows a single focal spot from the single array of focal spots, in the case of the reference beam, captured during the display of the type-A grating pattern. The corresponding line plot along the centre of the spot is shown in Fig. 7.4 (i)(b). The same focal spot from the four sub-arrays of focal spots, during the display of the type-C grating pattern and the corresponding line plot along the centre of

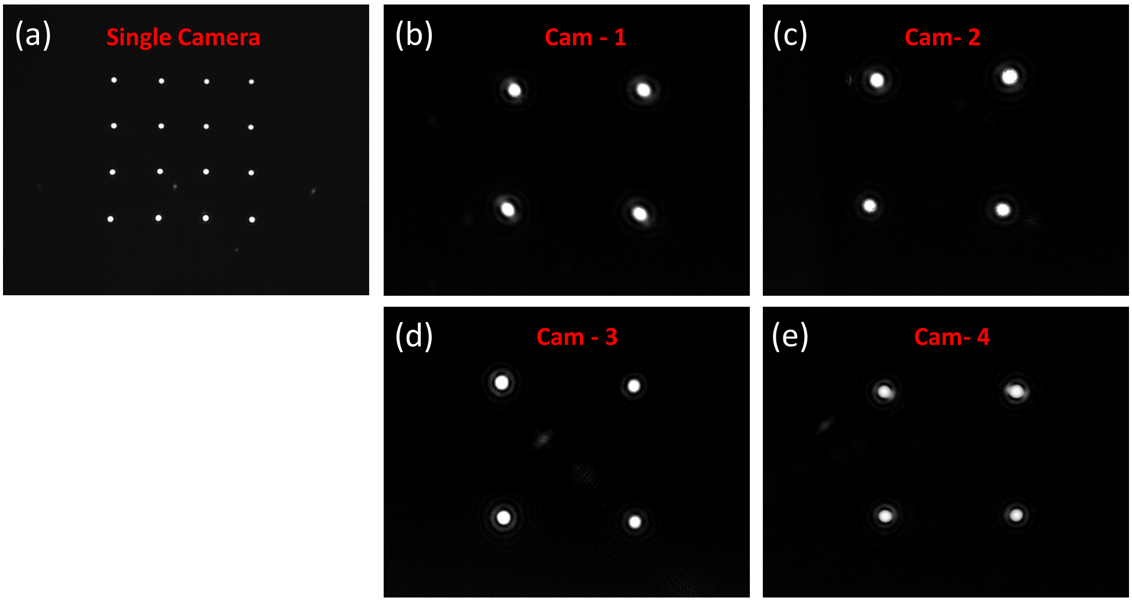

**Figure 7.3:** (a) An array of 4 × 4 focal spots due to the type-A grating pattern captured using a single camera, and the corresponding (b)-(e) four 2 × 2 sub-arrays of focal spots due to the type-C grating pattern, captured using four cameras.

the spot are shown in Fig. 7.4 (ii)(a) and Fig. 7.4 (ii)(b), respectively. It is to be noted that each of the +1 order focal spots corresponds to an unaberrated plane wavefront corresponding to a given zone. Thus, the focal spot is expected to have a symmetric intensity distribution with the centroid coinciding with the centre of the focal area. Therefore, the correct centroid position of a focal spot is defined as the co-ordinate of the middle point of the corresponding FWHM region. The measured centroid position on the other hand, is obtained by using the standard centre of mass algorithm (given by Eq. 2.1 in chapter 2). The correct centroid positions and the respective measured centroid positions are denoted by green colored star and red colored circle, respectively. We compute the centroid detection error by taking the root mean square (RMS) value of the difference between the correct centroid and the corresponding measured centroid. The RMS error for the type-A grating pattern, captured using a single camera is found to be 4.62 pixels, whereas for the type-C grating pattern captured using four cameras, the same is found to be 1.02 pixels. It is to be mentioned that the number of pixels used to define each of the focal spots in the case of four cameras (type-C grating pattern) is almost 7.94 times the number of pixels used to define the focal spot captured using a single camera (type-A grating pattern).

The experimentally obtained arrays of focal spots due to the type-A and type-

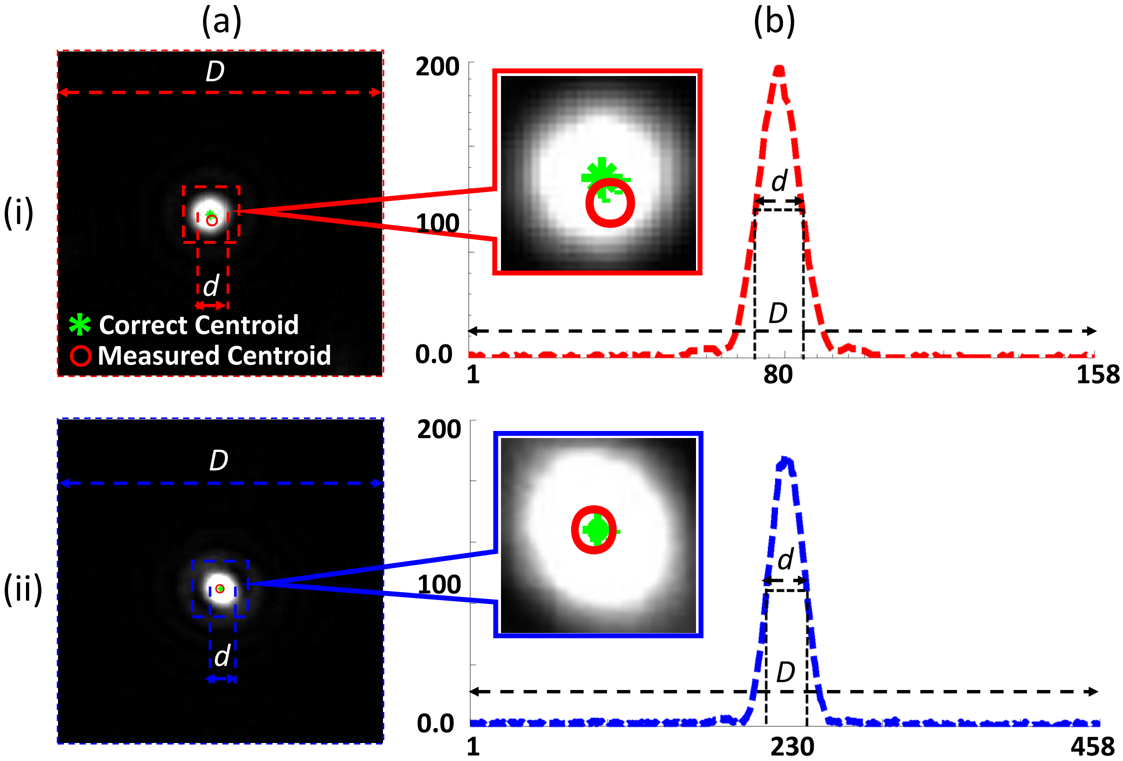

**Figure 7.4:** A (i)(a) single focal spot due to the type-A grating pattern (captured using a single camera) and its (i)(b) corresponding line plot across the centre of the spot, for a 4 × 4 grating array dimension. (ii)(a) The same focal spot due to the type-C grating pattern and (ii)(b) the corresponding line plot across the centre. The X and Y axes of the line plots are in camera pixel units and the intensity value in arbitrary units, respectively.

C grating patterns having a dimension of 8 × 8 are shown in Fig. 7.5. Figure 7.5 (a) is due to the type-A grating pattern that is captured using a single camera, whereas Fig. 7.5 (b)→ Fig. 7.5 (e) are four sub-arrays of focal spots due to the type-C grating pattern, captured using four cameras. The detector subaperture length ($D$) and the corresponding FWHM ($d$) are found to be 102 pixels and ∼27 pixels, respectively, for each focal spot (type-A grating pattern) captured using a single camera. However, the same are found to be 228 pixels and ∼60 pixels, respectively, for the focal spots (type-C grating pattern) captured using four cameras. The ratio $R$ is found to be 0.264 in the case of the single array of focal spots, due to the type-A grating pattern and 0.263 in the case of the four sub-arrays of focal spots due to the type-C grating pattern. Similarly, Fig. 7.6 (i)(a) shows a single focal spot (in the case of the reference beam) from the single array of focal spot, captured during the display of the type-A grating pattern and the corresponding line plot along the centre of the spot is shown in Fig. 7.6 (i)(b). The same focal spot from the four

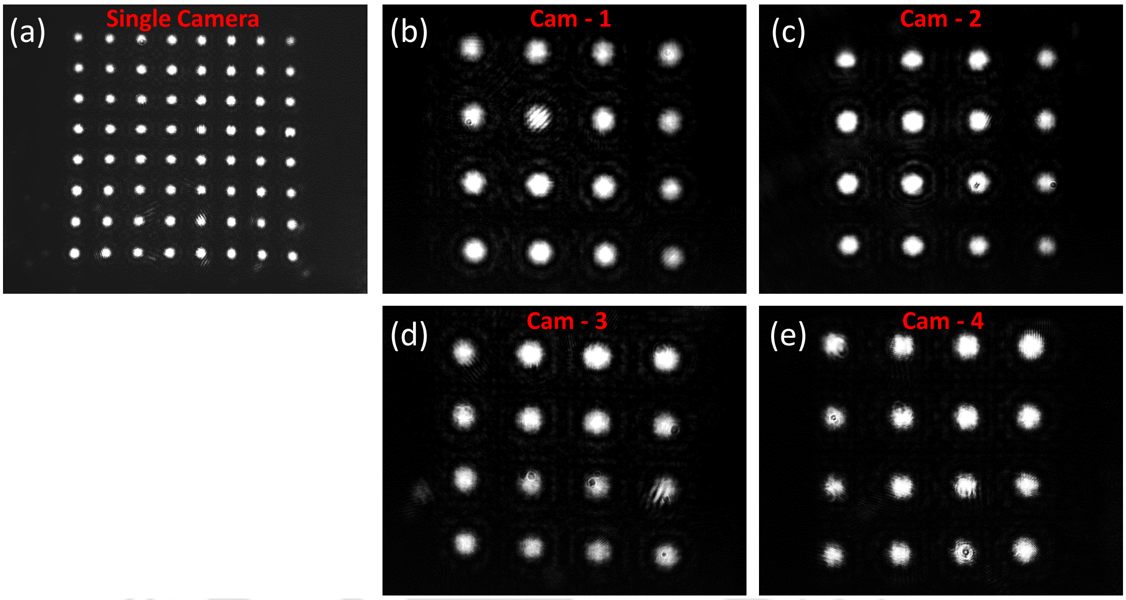

**Figure 7.5:** (a) An array of 8 × 8 focal spots due to the type-A grating pattern captured using a single camera, and the corresponding (b)-(e) four 4 × 4 sub-arrays of focal spots due to the type-C grating pattern captured using four cameras.

sub-arrays of focal spots, during the display of the type-C grating pattern, and the corresponding line plot along the centre of the spot are shown in Fig. 7.6 (ii)(a) and Fig. 7.6 (ii)(b), respectively. The centroid detection RMS error for the type-A grating pattern is found to be 3.14 pixels, whereas for the type-C grating pattern it is found to be 0.685 pixels. Further, the number of pixels used to define each of the focal spots in the case of four cameras ( type-C grating pattern) is almost 4.90 times the same due to the type-A grating pattern. The X-axis and Y-axis for all the line plots in Fig. 7.4 and Fig. 7.6 are in camera pixel units and the intensity value in arbitrary units, respectively.

From the above results it is evident that the use of multiple cameras describe each of the focal spots over a larger detector subaperture area, thereby increasing the effective number of camera pixels to locate the centroid position of a focal spot. Consequently, the centroid detection RMS error due to the type-C grating pattern is smaller in comparison to the type-A grating pattern. Also, we observe that the centroid detection RMS error decreases with the increase in grating array dimensions.

We perform another experiment to demonstrate the capability of the proposed scheme to enhance the dynamic range, considering grating array dimensions of 4 × 4 and 8 × 8. Figure 7.7 (i)(a) shows the 4 × 4 array of focal spots due to the type-A

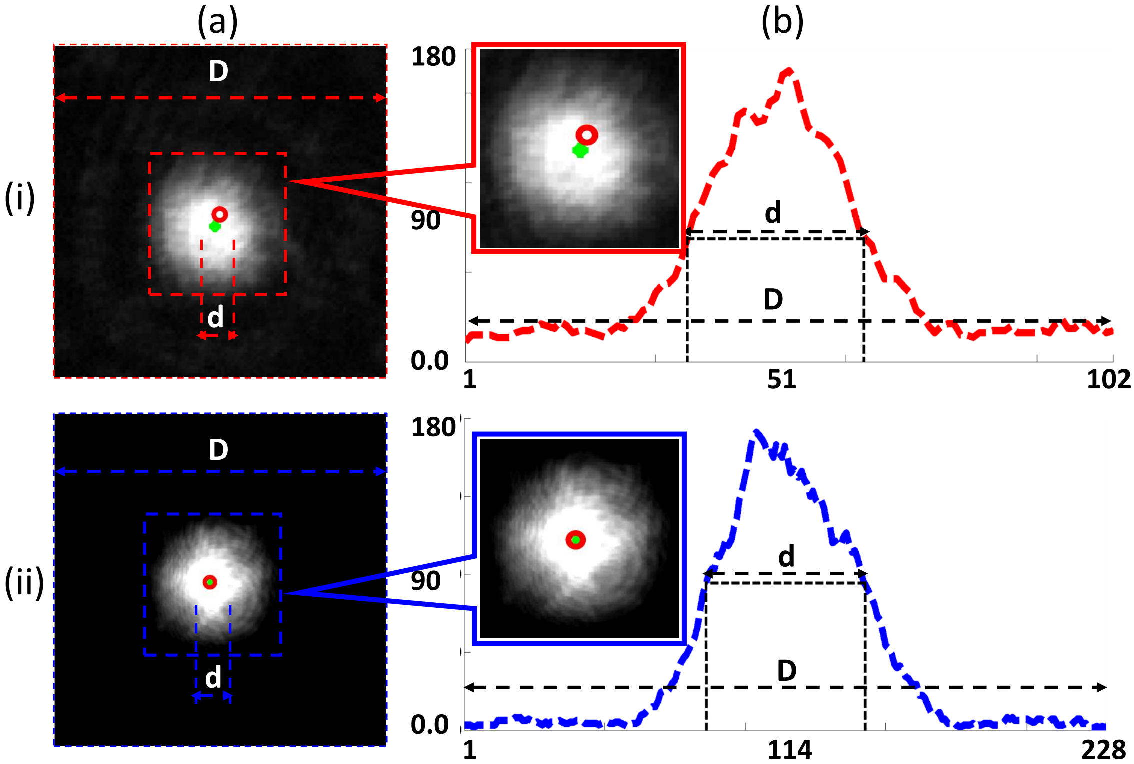

**Figure 7.6:** A (i)(a) single focal spot due to the type-A grating pattern (captured using a single camera) and its (i)(b) corresponding line plot across the centre of the spot, for a 8 × 8 grating array dimension. (ii)(a) The same focal spot due to the type-C grating pattern and (ii)(b) the corresponding line plot across the centre. The X and Y axes of the line plots are in camera pixel units and the intensity value in arbitrary units, respectively.

grating pattern, captured using a single camera. A single focal spot from such a pattern and the corresponding line plot along the centre of the spot are shown in Fig. 7.7 (i)(b) and Fig. 7.7 (i)(c), respectively. Figure 7.7 (ii)(a) shows the 2 × 2 array of focal spots due to the type-C grating pattern, captured using one of the four cameras. A single focal spot from the 2 × 2 array of focal spots and its corresponding line plot along the centre of the spot are shown in Fig. 7.7 (ii)(b) and Fig. 7.7 (ii)(c), respectively. Figure 7.8 shows similar plots for grating array dimensions of 8 × 8. The X-axis and Y-axis for all the line plots in Fig. 7.7 and Fig. 7.8 are in camera pixel units and the intensity value in arbitrary units, respectively. In order to make a comparison of enhancement in the dynamic range, each focal spot is defined over nearly same number of camera pixels (i.e., the value of $d$ is kept the same for both the types of grating pattern). In the case of the 4 × 4 grating pattern, the value of FWHM ($d$) is ∼30 pixels for both the type-A and type-C grating patterns, whereas the detector subaperture length ($D$) in the case of the type-A and type-C grating

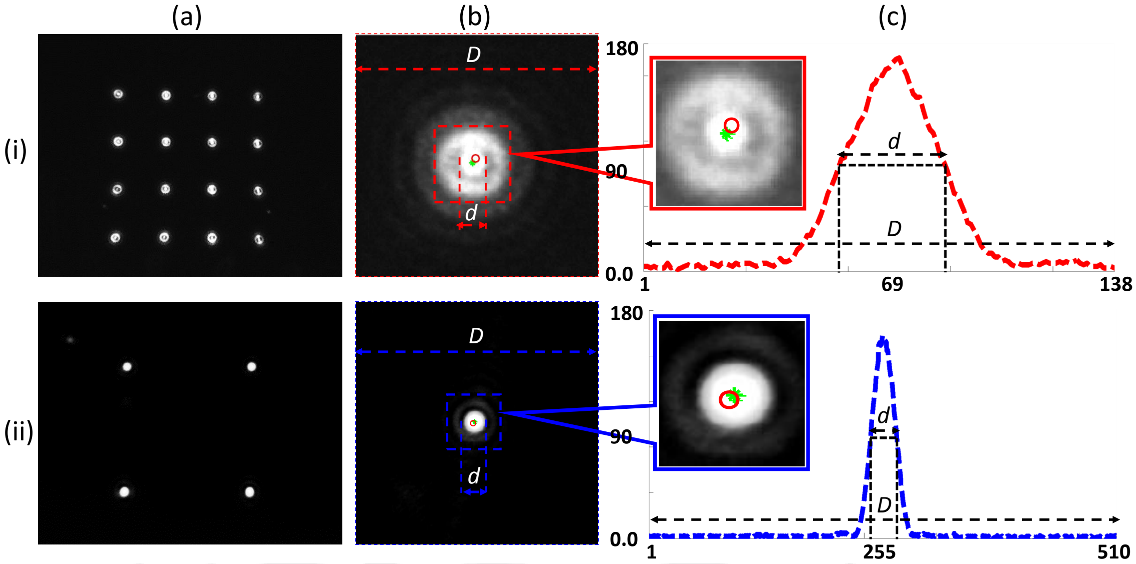

**Figure 7.7:** An array of (i)(a) $4\times4$ focal spots, (i)(b) a single focal spot (from (i)(a)) and the corresponding (i)(c) line plot along the centre of the spot, due to the type-A grating pattern captured using a single camera. (ii)(a) An array of $2\times2$ focal spots, (ii)(b) a single focal spot (from ii(a)) and the corresponding (ii)(c) line plot along the centre of the spot, due to the type-C grating pattern captured using one of four cameras. The X and Y axes of the line plots are in camera pixel units and the intensity value in arbitrary units, respectively.

patterns are 138 pixels and 510 pixels, respectively. Similarly, in the case of the $8\times8$ grating pattern, the value of FWHM ($d$) for both the type of grating patterns is ∼31 pixels, whereas the detector subaperture lengths ($D$) are 116 pixels and 258 pixels, in the case of the type-A and type-C grating patterns, respectively. The increase in detector subaperture length ($D$), while maintaining a constant FWHM ($d$), increases the dynamic range of the sensor by a factor of ∼3.69 and ∼2.22, in the case of the grating array dimensions $4\times4$ and $8\times8$, respectively. The crosstalk of the sensor using the four cameras is also reduced by a similar factor in comparison to a single camera.

We then apply the same computer generated holography technique [29, 30] as discussed previously to incorporate a linear combination of 5 Zernike modes, shown in Table 3.1 of chapter 3, as applied phase, $\phi(x,y) = 1Z_4+1Z_5\text{-}0.5Z_8+1Z_9\text{-}0.5Z_{11}$, to the reference beam. The wavefront estimation accuracy using the proposed beam splitting mechanism is illustrated in Fig. 7.9 for grating array dimension of $8\times8$, (in the case where the ratio $R$ is maintained constant for both type-A and type-C grating patterns). Figure 7.9(a) shows the false color image of the applied phase profile $\phi(x,y)$. The plots of the estimated phase profile using the modal estimation

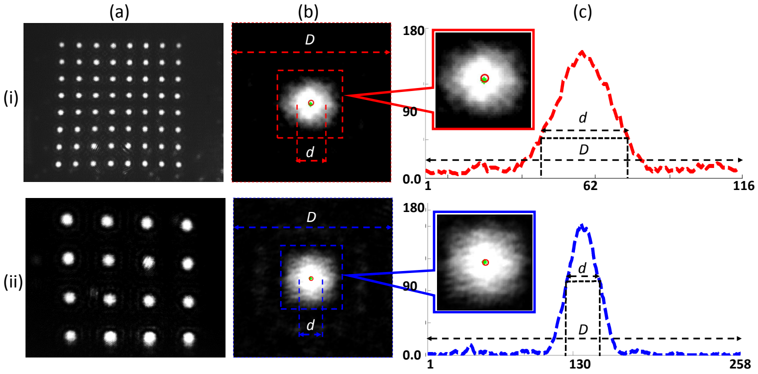

**Figure 7.8:** An array of (i)(a) 8 × 8 focal spots, (i)(b) a single focal spot (from (i)(a)) and the corresponding (i)(c) line plot along the centre of the spot, due to the type-A grating pattern captured using a single camera. (ii)(a) An array of 4 × 4 focal spots, (ii)(b) a single focal spot (from ii(a)) and the corresponding (ii)(c) line plot along the centre of the spot, due to the type-C grating pattern captured using one of four cameras. The X and Y axes of the line plots are in camera pixel units and the intensity value in arbitrary units, respectively.

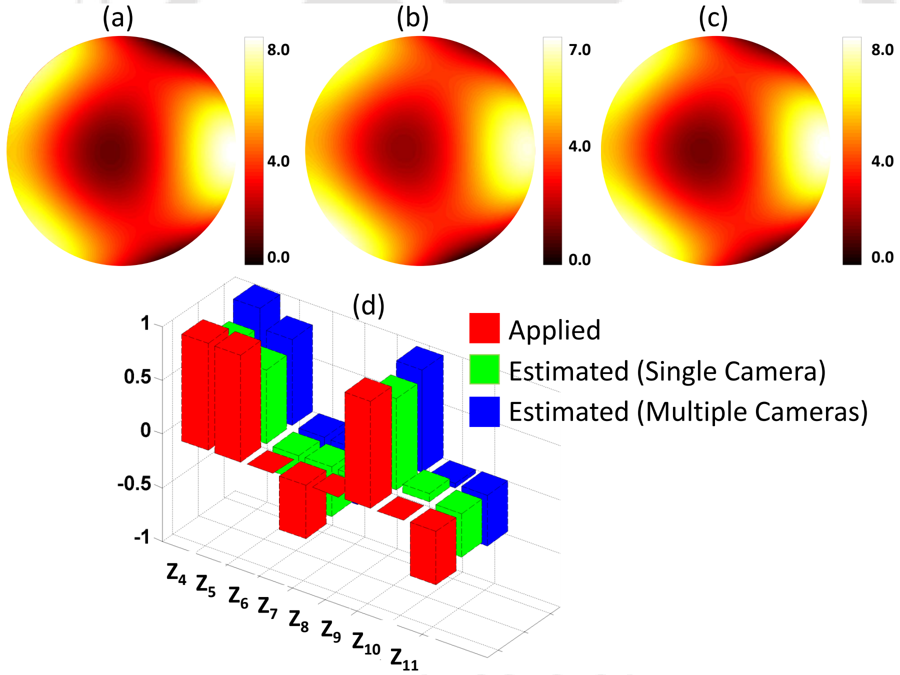

**Figure 7.9:** False color images of the (a) applied phase profile $\phi(x, y)$ and its corresponding estimated phase profile using modal estimation method using grating array dimension of 8 × 8 due to (b) the type-A grating pattern and (c) the type-C grating pattern. (d) Bar diagram showing the RMS amplitudes of the 8 Zernike modes applied (red color) and estimated for the type-A grating pattern (green color) and the type-C grating pattern (blue color), where the scale is in radian unit.

method as discussed in section 2.7 of chapter 2, for the type-A grating pattern and the type-C grating pattern are shown in Fig. 7.9(b) and Fig. 7.9(c), respectively. The bar diagrams in Fig. 7.9 (d) represent the root mean square (RMS) amplitudes of the 8 Zernike modes applied (red color) and detected using the modal estimation method for the type-A grating pattern (green) and the type-C grating pattern (blue), respectively. All the plots shown in Fig. 7.9 are in radian units. Similar to our previous discussion, the errors in the measured phase profiles is computed by obtaining the root mean square (RMS) value of the difference between the applied phase profile and the corresponding estimated phase profile. The RMS errors for the type-A grating pattern and the type-C grating pattern are found to be 0.0139 $\mu$m and 0.0085 $\mu$m, respectively.

## 7.7 Conclusion

In this chapter, we have proposed an improved centroid detection scheme in the grating array based zonal wavefront sensor (GAWS) by employing a beam splitting mechanism and using multiple digital cameras. A detail description about the proposed scheme is provided that illustrates generation of multiple sub-arrays of focal spots, which are to be captured using multiple cameras. Use of multiple cameras help in defining each of the focal spots using more number of pixels and over a larger detector subaperture area. We have described a proof-of-concept experimental arrangement that demonstrates the working of the proposed scheme for different grating array dimensions. Improvement in the centroid detection accuracy and the subsequent decrease in the centroid detection RMS errors have been observed due to the use of more number of cameras. It is to be noted that the improvement in centroid detection is achieved without any pre-processing or post-processing of the data. It is also observed that the proposed scheme has the capability to enhance the dynamic range of the sensor and to reduce the possibility of crosstalk between adjacent zones. We also provide experimental results that demonstrate wavefront estimation accuracy as a result of improvement in the centroid detection accuracy, due to the use of multiple cameras in comparison to a single camera.

# CHAPTER 8

# Design of a Zonal Wavefront Sensor Based on a Printed Array of Binary Diffraction Grating

## 8.1 Introduction

In this chapter, we describe the design and fabrication of a grating array based zonal wavefront sensor using a print of an array of binary diffraction gratings on a transparent polyester sheet. The binary diffraction grating array printed on the polyester sheet produces an array of focal spots corresponding to a diffraction order, similar to that of the focal spots produced by the Shack Hartmann wavefront sensor (SHWS). We provide the relations involving the controllable parameters of the grating array to generate a well separated $+1$ order focal spots, for a given focusing lens. We then present a brief description of the implementation of the proposed sensing method. Experimental results show the generation of $+1$ order focal spots, agreeing well with the numerical simulation results and demonstrate a reasonably accurate estimation of an applied phase profile in the incident beam.

## 8.2 Review of the Related Work

As discussed already the lenslets array is the most important component of the Shack Hartmann wavefront sensor (SHWS). Thus, fabrication of a high quality lenslets array is necessary to realise a good SHWS [128]. The lenslets array can be fabricated in a number of ways [129], such as by using glass compression molding [130], diamond turning [131], diamond flycutting [132], thermal reflow [133], etc. However, earlier method of fabrication of the lenslets array was quite tedious. It involved a number of operations, such as cutting and polishing of glass slab with certain shape, individual mounting of each lens, etc. [25]. Moreover, the fabricated lenslets array had limitations in the form of quality of the film, the material on which it could be fabricated, and the ability to make small lenslets. Another issue with the fabricated lenslets array is the uniformity over the shape, size, fill factor, and the geometrical arrangement of the lenslets, as the same has profound effect on the sampling of the incident beam [134]. Once fabricated the lenslet array has a fixed geometry; however, this fixed geometry on the other hand results in rigidity in the case of dynamic range of the SHWS. It is also necessary that all the lenslets should be so aligned that they produce the corresponding focal spots on a plane where the camera needs to be positioned. Any misalignment of the lenslets lead to measurement inaccuracies [135, 136].

Recent developments in the field of binary optics technology has minimised the fabrication related issues to a great extent. Nowadays, the design of the lenslets is accurately determined by the customized computer aided design (CAD) program. This leads to the designing of lenslets of various shape, size or pattern [26, 27]. However, often for different types of applications it becomes necessary to adjust the design parameters to make them specific for the task at hand. This requires redesigning and manufacturing of a new lenslets array and thus, cannot be done quickly and in a cost effective manner. The grating array based zonal wavefront sensor implemented using an LCSLM, as discussed in the previous chapters, facilitates quick implementation of new sensor designs specific to the application. However, the GAWS discussed already in this thesis essentially requires the availability of an LCSLM. In this chapter, we show that the GAWS can be implemented even without an LCSLM, by printing the grating array pattern on a polyester sheet [137]. The grating array synthesized in such a way is devoid of several fabrication related issues that need to be taken into account while fabricating a lenslet array. The grating array can be printed on a polyester sheet using an ordinary laser printer which facilitates application specific redesigning and quick sythesization of new sensor arrays in a cost effective manner.

## 8.3 Design Considerations

The grating array of a certain dimension is first numerically constructed, in a similar way as discussed in chapter 3. A laser printer is then used to print these numerically constructed grating array patterns on a transparent polyester sheet. The printer is used to print only in black or white even though it is capable of printing shades of grey. The polyester film used in this work is made of mostly amorphous material ($\sim$ 65 %) and has a thickness of around 100 micron. The polyester sheet used ensures that there is no streaky or messy printing. Each grating element is described over an area which is much larger than the size of a dot of the printer or a unit of the polyester film with specific optical property. This ensures uniformity of the optical properties over each grating element. The material of the polyester film is such that it does not introduce any artefacts or unwanted diffraction effects to the incident beam. Besides, the temperature variation during the measurement process has no significant effect on the optical properties of the fabricated individual grating elements. Thus, it is ensured that there is no variation in the optical properties in the generated focal spots due to the individual grating elements.

All the grating arrays generate focal spot arrays of the same dimension when an unaberrated beam is incident on the respective grating array. However, it is also possible to form lesser number of focal spot rows (regardless of the grating array dimension) for an unaberrated incident beam by choosing $(f_{0x}^i, f_{0y}^j)$ in a way as described in section 3.9 of Chapter 3. This results in the reduction of the effective number of rows of the digital camera, used to capture the focal spot arrays, leading to a higher sensing frame rate. However, the enhancement in sensing frame rate is accompanied by a reduction of the dynamic range in one direction. All the focal spots lie on the focal plane of the lens considering focusing by an aplanatic lens or focusing under paraxial approximation. Thus, the proposed scheme can avoid zonewise variation in the focal lengths which might arise when a lenslet array is fabricated. To enhance the dynamic range, adjacent $+1$ order spots in the focal plane must be sufficiently separated. However, achievable resolution of the printer puts the upper limit to the range of spatial frequencies that can be used to describe the grating elements. On the other hand, the lower limit of the spatial frequency is decided by the width of the 0 order focal spot so that there is no overlap between the 0 order spot and the $+1$ order spot corresponding to the grating element with the lowest spatial frequency. Therefore, to get the best performance with the scheme, a printer with the highest possible resolution must be selected.

### 8.3.1 Theoretical Expressions

Here, we develop a theoretical expression using laws of geometrical optics to relate the separation between 0 order and the +1 order beams with the various controllable parameters of the grating element.

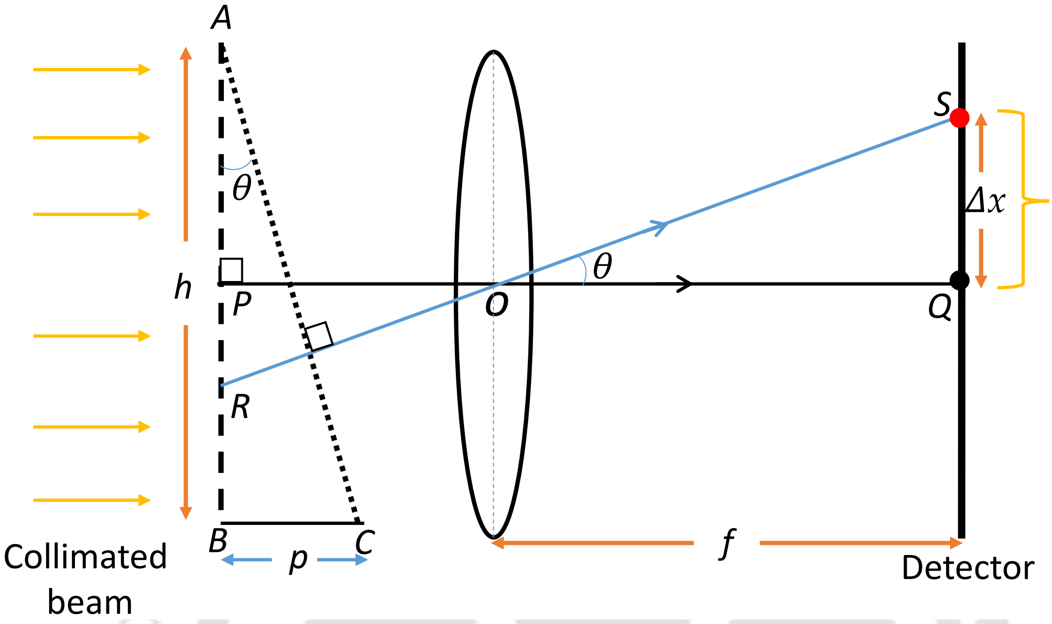

**Figure 8.1:** Ray diagram showing the shift of the focal spot as a function of tilt of the wavefront portion across a single grating aperture.

Let $AB$ represents a binary diffraction grating element which is illuminated by a collimated laser beam as shown in Fig. 8.1. The two chief rays $PQ$ and $RS$ pass through the centre of the lens to form 0 order focal spot and +1 order focal spot at the location $Q$ and $S$, respectively. Here, $h$ represents the physical dimension of a single diffraction grating element (to be printed on a transparent sheet); $p$ represents the path difference at the extreme end between the diffracted and the un-diffracted wavefronts $AB$ and $AC$; $f$ is the focal length of the converging lens; and $\Delta x$ is the distance between the 0 order focal spot and +1 order focal spot. Now,

$$\tan\theta = \frac{BC}{AB} = \frac{SQ}{OQ} \tag{8.1}$$

Therefore,

$$\frac{p}{h} = \frac{\Delta x}{f} \tag{8.2}$$

$$\Delta x = f\frac{p}{h} \tag{8.3}$$

The relation between the path difference ($p$) and phase difference is given by, path difference (p) $= \frac{\lambda}{2\pi}\times$ phase difference. The phase difference on the other hand depends on the spatial frequency (i.e., $f_{0x}$ value) defined during the computation of the diffraction grating element. For a given spatial frequency $f_{0x}$, the phase difference at the extreme end of the element is $2f_{0x}\pi$. Thus, we get,

$$p = \frac{\lambda}{2\pi} \times 2f_{0x}\pi$$

$$p = f_{0x}\lambda$$

Therefore, from Eq. 8.3, we get,

$$\Delta x = f\frac{f_{0x}\lambda}{h} \tag{8.4}$$

This expression is valid in case the tilt in the grating element is introduced in only one direction, i.e., either in horizontal direction or vertical direction. However, if the tilt is introduced in both the directions, then Eq. 8.4 gets modified as,

$$\Delta x = f\frac{\sqrt{(f_{0x})^2 + (f_{0y})^2}\lambda}{h} \tag{8.5}$$

As seen from Eq. 8.5, the separation between the 0 order focal spot and the +1 order focal spot is a function of focal length of the lens, physical dimension of the diffraction grating element, spatial frequency describing the tilt and the wavelength of the collimated beam. All these parameters are to be chosen appropriately so that it results in a well separated +1 order focal spots array.

### 8.3.2 Experimental Verification

Numerically constructed binary diffraction grating arrays of dimension $3\times 3$, $4\times 4$ and $12\times 12$ are printed on separate transparent polyester films. Figure 8.2(a) shows the numerically constructed binary diffraction grating array of dimension $3 \times 3$ which correspond to $h = H/N = 0.006$ m (where, $H$ and $N$ represents the physical length and the dimension of the printed array of grating pattern, respectively). The representative focal spots as obtained in the Fourier plane is shown in Fig. 8.2(b). Here, $O$ represents the 0 order focal spot. Let, us assume that the top-left grating

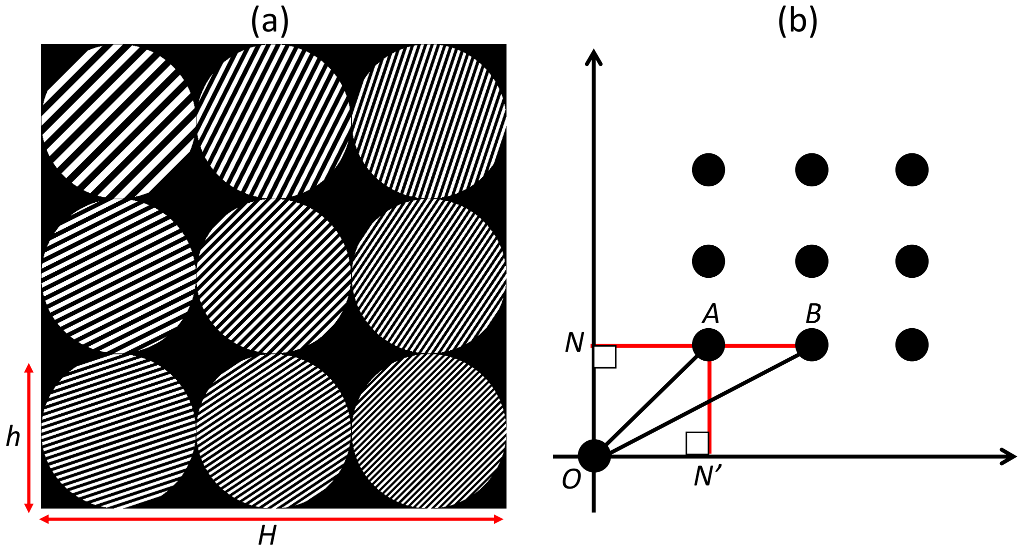

**Figure 8.2:** A binary diffraction grating array of dimension (a) 3 × 3 to be printed on a polyester sheet and (b) its representative focal spots obtained in the Fourier plane of the grating array.

element and its adjacent grating element (along horizontal direction) results in the +1 order focal spots $A$ and $B$, respectively, for a plane incident beam. Let, $AN$ and $AN'$ be the two normals drawn from the two +1 orders on the two orthogonal axes. Here, we use a converging lens of focal length ($f$) 1 m and a laser beam of wavelength ($\lambda$) = $532 \times 10^{-9}$ m. In the case of 3 × 3 grating pattern, the spatial frequencies of the top-left grating element is taken as 1.3 lines/mm [i.e., ($f^1_{0x}$, $f^1_{0y}$) = (8, 8)] along the two orthogonal directions. Further, the increment in spatial frequencies between adjacent elements is taken as 1.3 lines/mm [i.e., ($\Delta f^1_{0x}$, $\Delta f^1_{0y}$) = (8, 8)] along the two orthogonal directions. Substituting the respective values in Eq. 8.5, we get OA = 1.00 mm. Again since $f^1_{0x} = f^1_{0y}$ we have ON = AN. Therefore, by using Pythagoras theorem, we get,

$$\begin{aligned} OA^2 &= ON^2 + AN^2 \\ AN = \frac{OA}{\sqrt{2}} &= \frac{1}{\sqrt{2}} = ON \end{aligned} \tag{8.6}$$

Since $f^1_{0x} = f^1_{0y} = \Delta f^1_{0x} = \Delta f^1_{0y}$. Therefore $AN = AB = 0.707$ mm.

Hence, the theoretical expressions suggest that the separation between 0 order and the nearest +1 order is 1.00 mm (= OA), whereas the separation between consecutive +1 orders (= AB) is 0.707 mm. In the case of the 4 × 4 grating array, $h$

= 0.0045 m. The spatial frequencies of the top-left grating element is taken as 1.8 lines/mm [i.e., $(f^1_{0x},\ f^1_{0y}) = (8,\ 8)$] along the two orthogonal directions. The increment in spatial frequencies between adjacent elements is chosen to be 1.3 lines/mm [i.e., $(\Delta f^1_{0x},\ \Delta f^1_{0y}) = (8,\ 8)$] along the two orthogonal directions. The theoretical expressions now suggest the separation between 0 order and the nearest +1 order to be 1.33 mm, while the separation between consecutive +1 orders is suggested to be 0.709 mm. In the case of 12 × 12 grating pattern, $h = 0.0015$ m. The spatial frequencies of the top-left grating element is taken as 2 lines/mm [i.e., $(f^1_{0x},\ f^1_{0y}) = (3,\ 3)$] along the two orthogonal directions. Further, the increment in spatial frequencies between adjacent elements is taken as 0.66 lines/mm [i.e., $(\Delta f^1_{0x},\ \Delta f^1_{0y}) = (1,\ 1)$] along the two orthogonal directions. Thus, using the theoretical expressions, the separation between the 0 order and the nearest +1 order is found to be 1.5 mm, whereas the separation between consecutive +1 orders is found to be 0.35 mm.

In our experiment, camera records both the 0 order focal spot and the +1 order focal spots for a plane incident wavefront. We then estimate the separation between the centres of the 0 order and +1 order focal spot (i.e., OA) from the captured image. In the case of 3 × 3 grating pattern, the separation $OA$ is found to be 1.14 mm. Similarly, the separation between the centres of consecutive +1 orders is found to be of 0.68 mm. While, in the case of $4 \times 4$ grating pattern, a separation of about 1.23 mm is obtained between the centres of the 0 order focal spot and the nearest +1 order spot. The consecutive +1 order focal spot separation is found to be 0.69 mm. Similarly, in the case of $12 \times 12$ grating pattern, a separation of about 1.46 mm is obtained between the centre of the 0 order focal spot and the nearest +1 order spot. The consecutive +1 order focal spot separation on the other hand is found to be 0.32 mm. It is seen that the experimentally obtained focal spot locations agree reasonably well with the respective theoretically obtained locations. Thus, the grating array printed on a transparent sheet is able to generate the focal spots with reasonably accurate separation between them.

## 8.4 Experimental Implementation

The schematic diagram of the experimental arrangement to implement the proposed grating array based zonal wavefront sensor is shown in Fig. 8.3. The beam from a green DPSS laser is expanded and collimated using a lens combination of $L_1$ and $L_2$. To illuminate the entire grating pattern, printed on the transparent sheet of polyester film, over an area of 1.8 cm×1.8 cm, the diameter of the expanded beam is made $\sim$ 2.54 cm. The beams diffracted by the grating array is focused by lens $L_3$ of focal length 1 m. An iris diaphragm ($ID$) allows only the +1 order focal spots to enter the camera plane. The recorded arrays of +1 order focal spots corresponding to grating array of dimensions $3 \times 3$, $4 \times 4$ and $12 \times 12$ are shown in Figs. 8.4 (b), (d) and (f), respectively, while Figs. 8.4 (a), (c) and (e) show the corresponding +1 order focal spots obtained using numerical simulation. As stated earlier, the proposed sensing scheme has the capability to configure the spatial frequency of the grating elements in such a way that it produces focal spots with lesser number of rows. The spatial frequencies of the binary diffraction grating array of dimension $4 \times 4$ is reconfigured to result in a focal spot array of dimension $2 \times 8$. The focal spot array of dimension $2 \times 8$ as obtained experimentally and the corresponding focal spot array obtained numerically are shown in Figs. 8.4 (h) and (g), respectively. As already discussed it results in a reduction in the effective number of rows of the camera to capture the entire focal spot array by a factor of 2 as compared to the focal spot array of dimension $4 \times 4$. Since the frame rate of a camera is proportional to the effective number of rows or the height of the captured image, the formation of $2 \times 8$ focal spot array also results in an enhancement in the camera frame rate by a factor of 2. The generation of $12 \times 12$ focal spots as shown in Fig. 8.4 (f) demonstrate that the proposed sensing scheme has the capability to incorporate large number of zones into the sensor. However, the dynamic range per zone in such a case may get significantly reduced. This issue can be tackled by considering a printer with a higher DPI (dot per inch).

Through the above experiment, we successfully demonstrate the generation of widely separated focal spot arrays whose positions coincide with the expected positions. The close resemblance between the numerical results and the experimental results indicate that there is no observable variation in the optical properties between the individual grating elements. It is to be mentioned that the numerically generated focal spot arrays and the experimentally obtained focal spot arrays have different magnification factors. Also, there is a small amount of deviation in the focal spot positions in some cases, especially at the corners, due to field curvature from the focusing lens.

The next experiment performed aims to demonstrate the accuracy of wavefront measurement using the proposed sensor. Figure 8.5 shows the modified experimental setup in which a liquid crystal spatial light modulator (LCSLM) based arrangement

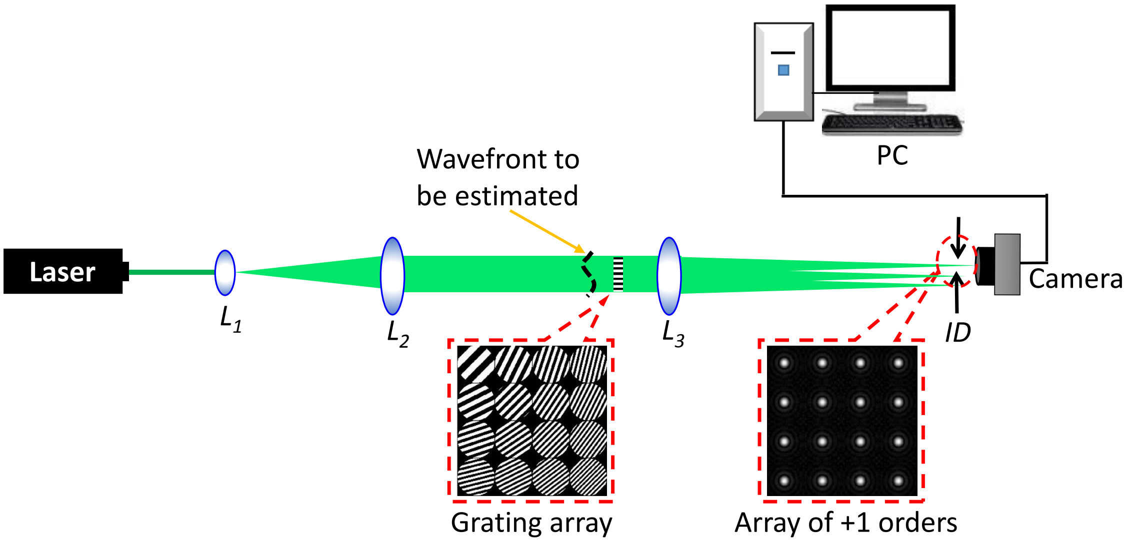

**Figure 8.3:** Arrangement of the proposed grating array based zonal wavefront sensing scheme.

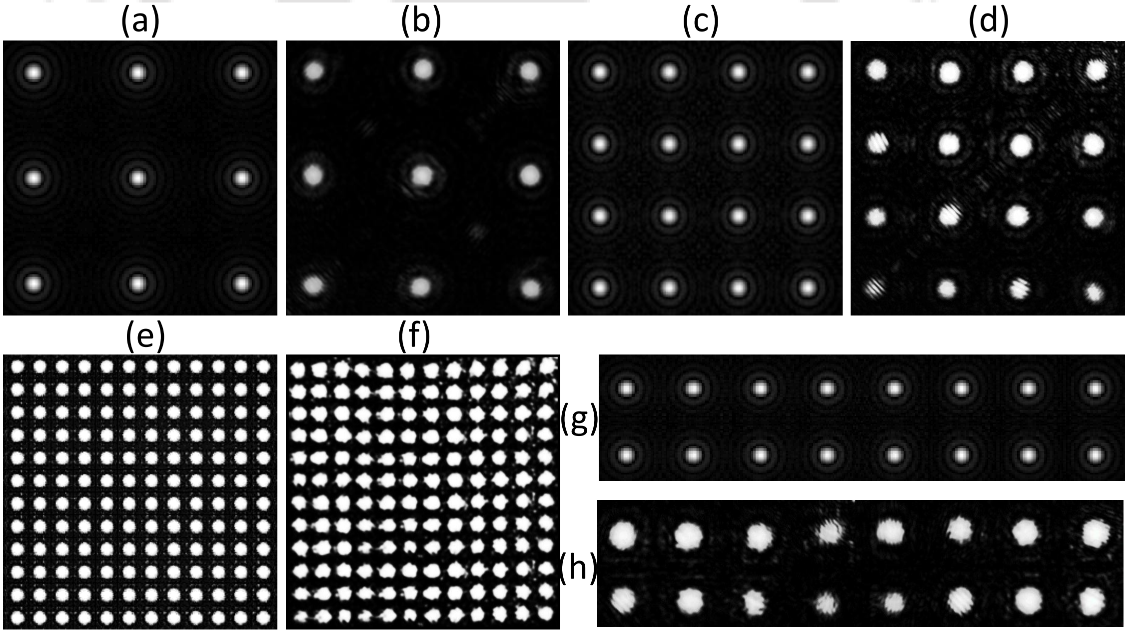

**Figure 8.4:** Regular 2D array of +1 order focal spots obtained numerically corresponding to grating patterns of dimension (a) 3 × 3, (c) 4 × 4, (e) 12 × 12 and (g) 2 × 8, and the respective experimentally obtained +1 focal spots corresponding to grating patterns of dimension (b) 3 × 3, (d) 4 × 4, (f) 12 × 12 and (h) 2 × 8.

is used. The LCSLM used here is of ferroelectric type (SXGA-R2). As discussed in chapter 3, the LCSLM assembly helps to generate a beam with user defined phase profile which can be made to incident onto the grating array printed on the transparent polyester film. As seen in Fig. 8.5, the collimated laser beam is incident on the LCSLM panel on which a particular type of hologram (described over $1024 \times 1024$ pixels) designed using a computer generated holography (CGH) technique [29, 30] is displayed. The hologram incorporates the phase profile of a certain amount of a Zernike mode aberration [65] into the +1 order beam diffracted by the hologram. Lens $L_3$ collects the light diffracted by the hologram and an iris diaphragm $ID_1$ isolates the +1 order beam to be incident on the grating array. The lens $L_4$ ensures that the +1 order beam illuminates the entire array of gratings printed on the transparent sheet. The lens combination $L_3$ and $L_4$ constitute a $4f$ relay system such that the LCSLM plane and the grating array plane are conjugate to one another. The array of +1 order beams diffracted by the printed grating pattern are focused onto the camera plane using the lens $L_5$. Again, to ensure that only the array of +1 order beams from the printed grating array pattern are incident on the detector plane, a second iris diaphragm, $ID_2$ is used.

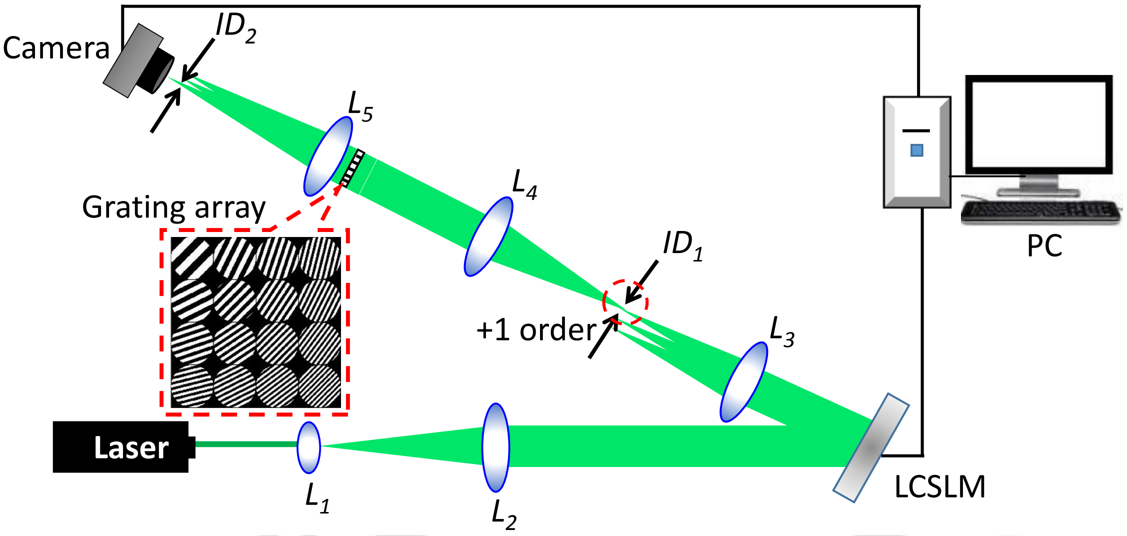

**Figure 8.5:** Schematic of the experimental arrangement comprising a liquid crystal spatial light modulator assembly, to demonstrate the accuracy of the proposed zonal wavefront sensor.

## 8.5 Results and Discussion

Here, we illustrate some of the results obtained from the experimental arrangement shown in Fig. 8.5, using grating array dimensions of $3 \times 3$, $4 \times 4$ and $12 \times 12$. Incident beams with three different phase profiles namely, the Zernike modes $Z_4$, $Z_5$ and $Z_{10}$ are generated using the LCSLM. At a time, each of the grating array dimension

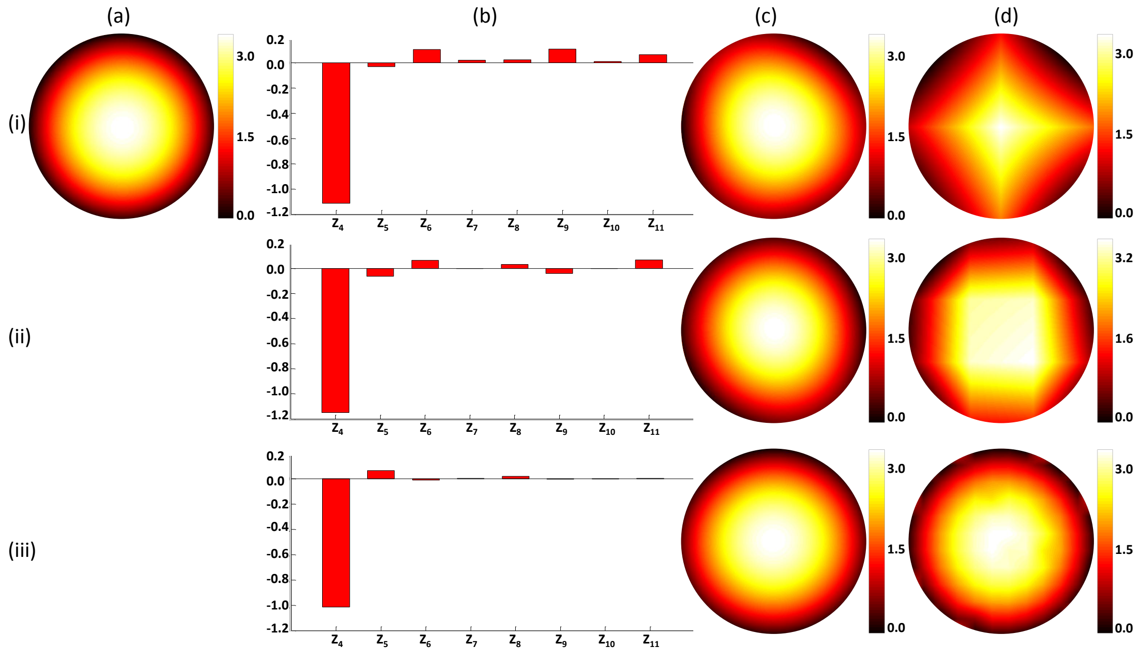

**Figure 8.6:** False color image representing the (a)(i) applied phase profile corresponding to Zernike mode $Z_4$. The corresponding estimated phase profiles, using modal estimation method, in the case of (c)(i) $3\times3$, (c)(ii) $4\times4$ and (c)(iii) $12\times12$ grating array dimensions, and using zonal estimation method in the case of (d)(i) $3\times3$, (d)(ii) $4\times4$ and (d)(iii) $12\times12$ grating array dimensions. The bar diagrams in (b)(i), (b)(ii) and b(iii) show the RMS amplitudes of the 8 Zernike modes detected using the modal estimation method for grating array dimensions of $3\times3$, $4\times4$ and $12\times12$, respectively. The axis labels appearing in all the images have the unit of radian.

is allowed to receive one particular Zernike mode phase profile. Both zonal and modal estimation methods are employed to measure the incident wavefront from the recorded focal spot shifts. For zonal estimation, the proposed improved algorithm described in section 4.4 of Chapter 4 is used and for modal estimation, the procedure described in section 2.7 of Chapter 2 is used. A total of 8 Zernike modes (i.e., $Z_4 \rightarrow Z_{11}$) are used for the modal wavefront estimation. We first incorporate Zernike mode $Z_4$ into the incident beam. Figure 8.6 (i)(a) shows the false color image of the applied phase profile, $Z_4$ of RMS (root mean square) amplitude equal to -1 radian. The bar diagrams shown in Fig. 8.6(b)(i)→Fig. 8.6(b)(iii) present the measured RMS amplitudes of the 8 Zernike modes obtained using the modal estimation method, for grating array dimensions of $3\times3$, $4\times4$ and $12\times12$, respectively. The plots in Fig. 8.6(c)(i)→Fig. 8.6(c)(iii) show the corresponding estimated phase profiles for grating array dimensions of $3\times3$, $4\times4$ and $12\times12$, respectively. The plots in Fig. 8.6(d)(i)→Fig. 8.6(d)(iii) show the bilinear interpolated phase profiles estimated by employing zonal estimation method for grating array dimensions of 3 × 3, 4 × 4 and 12 × 12, respectively. We then incorporate Zernike mode $Z_5$ of RMS amplitude

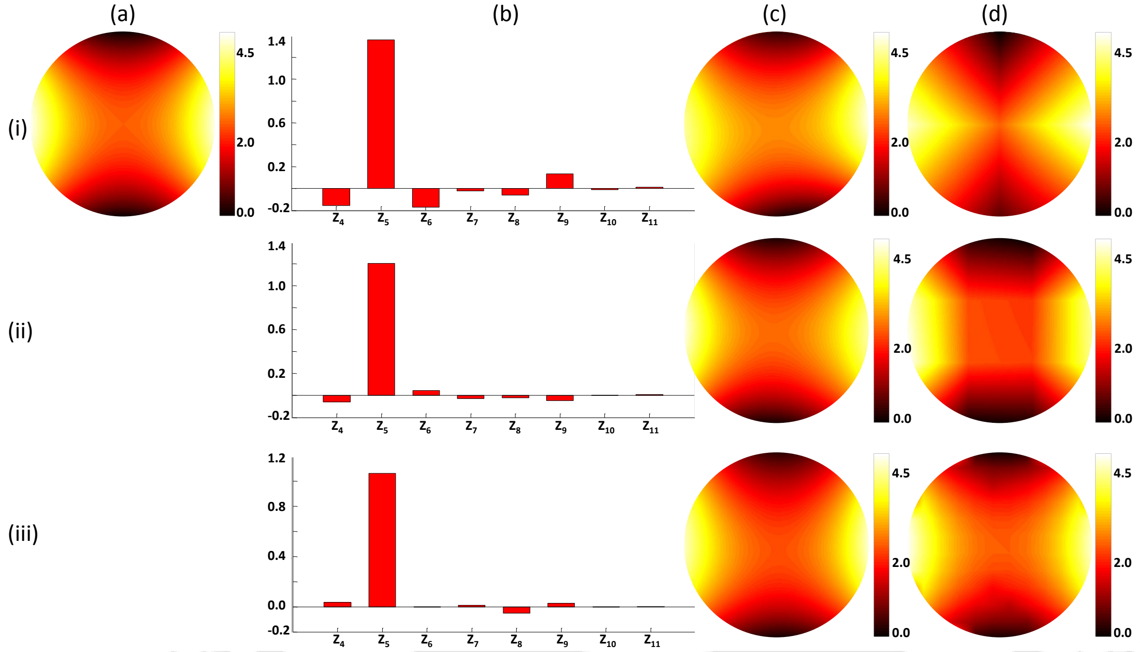

**Figure 8.7:** False color image representing the (a)(i) applied phase profile corresponding to Zernike mode $Z_5$. The corresponding estimated phase profiles, using modal estimation method, in the case of (c)(i) $3\times3$, (c)(ii) $4\times4$ and (c)(iii) $12\times12$ grating array dimensions, and using zonal estimation method in the case of (d)(i) $3 \times 3$, (d)(ii) $4 \times 4$ and (d)(iii) $12 \times 12$ grating array dimensions. The bar diagrams in (b)(i), (b)(ii) and b(iii) show the RMS amplitudes of the 8 Zernike modes detected using the modal estimation method for grating array dimensions of $3\times3$, $4\times4$ and $12\times12$, respectively. The axis labels appearing in all the images have the unit of radian.

equal to 1 radian into the incident beam. Likewise in Fig. 8.6, the false color image of the applied phase profile, the bar diagram of RMS amplitudes of 8 Zernike modes detected using the modal estimation method, the phase profiles estimated using the modal estimation method and the bilinear interpolated phase profiles estimated using the zonal estimation method are shown in Figs. 8.7 (a), (b), (c) and (d), respectively. We then incorporate Zernike mode $Z_{10}$ of RMS amplitude equal to 0.8 radian into the incident beam. The false color image of the applied phase profile, the bar diagram of RMS amplitudes of 8 Zernike modes detected using the modal estimation method, the phase profiles estimated using the modal estimation method and the bilinear interpolated phase profiles estimated using the zonal estimation method are shown in Figs. 8.8 (a), (b), (c) and (d), respectively. All the plots in Fig. 8.6→Fig. 8.8 are expressed in radian units. The error in the estimated phase profile is calculated from the RMS value of the difference between the applied phase profile and the corresponding estimated phase profile. The error in the case of zonal wavefront estimation is denoted as $(RMS)_z$, while the same in the case of modal wavefront estimation is denoted as $(RMS)_m$. The RMS amplitudes of the Zernike mode phase profiles applied and the RMS errors in the estimated phase profiles using both the modal estimation method and the zonal estimation method are shown in Table 8.1. From the above results, presented in Fig. 8.6→Fig. 8.8

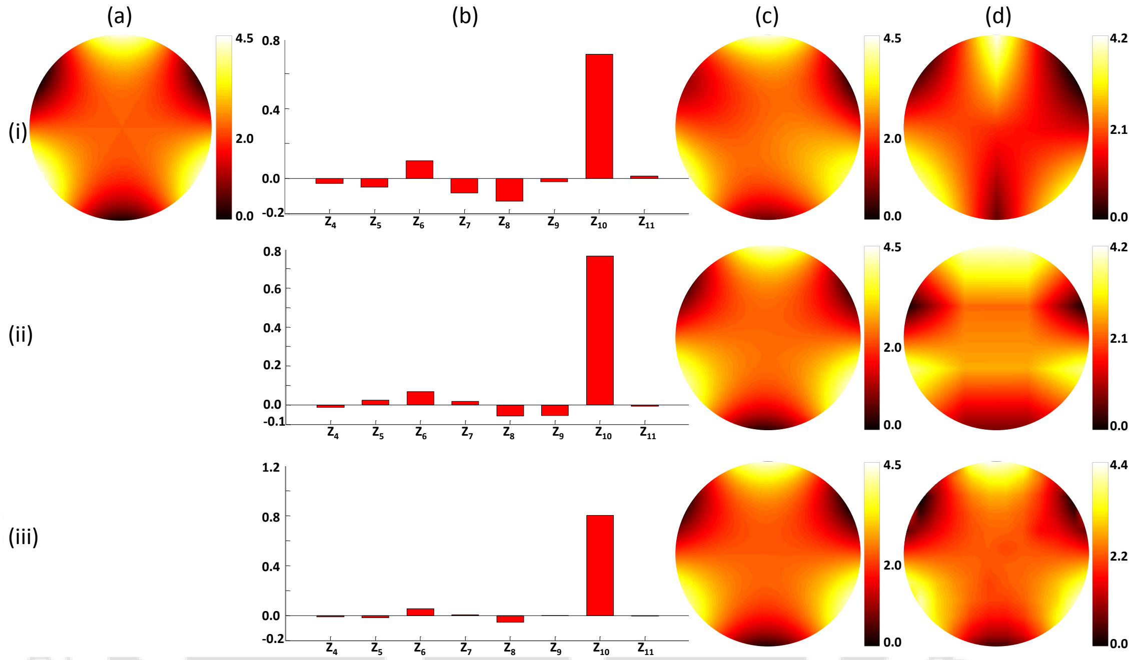

**Figure 8.8:** False color image representing the (a)(i) applied phase profile corresponding to Zernike mode $Z_{10}$. The corresponding estimated phase profiles, using modal estimation method, in the case of (c)(i) $3\times3$, (c)(ii) $4\times4$ and (c)(iii) $12\times12$ grating array dimensions, and using zonal estimation method in the case of (d)(i) $3 \times 3$, (d)(ii) $4 \times 4$ and (d)(iii) $12 \times 12$ grating array dimensions. The bar diagrams in (b)(i), (b)(ii) and b(iii) show the RMS amplitudes of the 8 Zernike modes detected using the modal estimation method for grating array dimensions of $3\times3$, $4\times4$ and $12\times12$, respectively. The axis labels appearing in all the images have the unit of radian.

and Table 8.1 corresponding to the grating arrays of dimension $3 \times 3$, $4 \times 4$ and $12\times12$, it is clear that the proposed wavefront sensor is able to estimate the incident wavefront reasonably well. It is also observed that the modal estimation method can estimate the phase profile of the applied Zernike mode more accurately than the zonal estimation method. Further, it is noticed that the RMS error of wavefront estimation decreases with increasing grating array dimensions (while the original wavefront dimension is kept constant).

| Zernike Modes ($Z_j$) | Applied RMS Amplitude (in rad) | (RMS)$_m$ in $\mu$m | | | (RMS)$_z$ in $\mu$m | | |
|---|---|---|---|---|---|---|---|
| | | 3×3 | 4×4 | 12×12 | 3×3 | 4×4 | 12×12 |
| 4 | -1 | 0.0186 | 0.0141 | 0.0052 | 0.0691 | 0.0512 | 0.0213 |
| 5 | 1 | 0.0249 | 0.0171 | 0.0058 | 0.0712 | 0.0526 | 0.0221 |
| 10 | 0.8 | 0.0322 | 0.0259 | 0.0124 | 0.0735 | 0.0580 | 0.0315 |

**Table 8.1:** Table showing the root mean square (RMS) errors in the estimated phase profile using the modal estimation method $(RMS)_m$ (in micron) and the zonal estimation method $(RMS)_z$ (in micron) for grating array dimensions of $3 \times 3$, $4 \times 4$ and $12 \times 12$, corresponding to Zernike modes, $Z_j$ ($j$ = 4, 5 and 10) for a particular applied RMS amplitude in radian.

## 8.6 Conclusion

In this chapter, we have implemented a zonal wavefront sensing scheme in which the core element is an array of plane diffraction gratings printed on a transparent sheet of polyester film. The proposed sensor is in fact a liquid crystal spatial light modulator (LCSLM) less version of the grating array based wavefront sensor (GAWS). An important feature of the grating array synthesized on a polyester film is that it is unaffected by several issues associated with the fabrication of a conventional lenslet array, commonly used in zonal wavefront sensing. Another advantage associated with the scheme is that it does not involve any specialized and expensive devices apart from a digital camera, leading to easy and cost effective implementation of the scheme. Further, the scheme offers advantages in the form of flexibility over the dynamic range, easy configurability, and option to enhance the sensing frame rate. The proposed sensing scheme is expected to be useful in wavefront sensing applications which do not demand a high spatial resolution. It will also be useful in applications which demand a cost effective and convenient way to alter the number of zones or the dynamic range of the zonal wavefront sensor used.

## CHAPTER 9

# Conclusion and Future Prospects

## 9.1 Introduction

In this chapter, we provide a brief summary of the entire thesis work. We also provide chapter-wise conclusion and important research findings along with the possibilities of future relevant research explorations.

## 9.2 Conclusion

The Shack Hartmann wavefront sensor (SHWS) is one of the most widely used zonal wavefront sensors, named after Johannes Franz Hartmann and Roland Shack. It consists of a 2D array of micro-lenses along with a detector placed at the common focal plane of these micro-lenses which captures the focal spot corresponding to each of the lenslets. A plane wavefront, when incident on the lenslet array, generates an evenly spaced grid of spots on the focal plane of the lenslets array. However, introduction of distortion into the incident wavefront will produce a displacement of the spots from their original locations. The shift of the focal spot centroid positions with respect to the reference positions contain information of the local wavefront slopes of the incoming distorted wavefront. These local slope information can be used in any of the standard estimation algorithm to obtain the phase profile of the incident beam. Thus, the SHWS has two essential steps, namely, the wavefront sensing and the wavefront estimation. However, a conventional Shack-Hartmann wavefront sensor encounters a number of issues in the process of wavefront sensing and wavefront estimation that puts limitations in the performance of the sensor.

The conventional SHWS has fixed number of lenses that leads to a fix dynamic range and there exists no option to dynamically vary the number of lenslets. Also, the conventional SHWS uses a digital camera to capture the focal spot array which has a low frame rate that limits the sensing frame rate of the sensor. An appropriate estimation geometry along with an estimation algorithm is mandatory for accurate measurement of wavefront in a SHWS. There are three basic estimation geometries available so far, which were proposed by Hudgin, Fried and Southwell. Of the three geometries, as far as robustness and error propagations are concerned, Southwell geometry is considered to be superior. Thus, the Southwell geometry is considered to be one of the most popular geometry for wavefront estimation. However, efforts are still on to come up with a more efficient estimation algorithm that can further improve the estimation performance over the Southwell algorithm without paying a cost to the processing time. An appropriate estimation algorithm should be evaluated in terms of the associated error propagation. Two important sources of error in the wavefront estimation process are the algorithm discretization error and slope measurement error. A robust estimation algorithm is expected to have less error propagation in regards to these important sources of error. The SHWS has limited spatial resolution due to the limited number of lenses used in sampling the incident wavefront. Scientific literature reveals several schemes to enhance the spatial resolution in the estimated wavefront in SHWS; however, the improvement comes at the expense of slower sensor frame rate. Another important aspect of the sensing process of a SHWS is the accuracy associated with the detection of the focal spot centroid position. The conventional SHWS has limited centroid detection accuracy due to the fixed number of pixels describing the sensor area of the digital camera. Existing ways to improve the accuracy comes at the cost of extensive pre-processing or post-processing of the data. Yet another important limitation of the SHWS is the fabrication of the lenslets array, as it is considered to be a tedious job because of the the number of steps involved. Recent developments in the fabrication technology has minimised its associated issues to a great extent. However, it still remains incompatible to many applications that require an easy and affordable fabrication scheme and can deliver a lenslet array of reasonably good performance, while the sensor parameters can be easily modified as when required by the application.

In the present thesis, we have developed a grating array based zonal wavefront sensor to address the above stated issues related to wavefront sensing and wavefront estimation in a SHWS. Our scheme has used a two dimensional array of plane diffraction gratings and a single focusing lens. This arrangement has thus replaced the lenslets array of the SHWS, thereby overcoming the limitations associated with the lenslets array. We have called such an arrangement as grating array based zonal wavefront sensor (GAWS). The proposed sensor has been implemented using a liquid crystal spatial light modulator (LCSLM), employing a computer generated holography technique.

The GAWS has offered a number of flexibilities and advantages over the SHWS. Unlike SHWS, in the case of GAWS, it is possible to form lesser number of focal spot rows than the number of rows of the grating array by configuring the spatial frequencies of each of the grating element. This has helped in enhancing the frame rate of the digital camera that images the array of focal spots as the camera can then be operated with lesser number of active rows. Formation of lesser number of focal spot rows also reduces the possibility of crosstalk in the vertical direction. The GAWS has also been implemented using a fast response FLCSLM that can display at least 1440 binary patterns in one second. This facility has been exploited to programmably incorporate lateral shifts in the grating array in order to enhance the spatial resolution in wavefront estimation. We have showed enhancement in the spatial resolution without compromising much on the sensing frame rate. The programmability of the GAWS has further enabled the use of more than one digital camera to record one focal spot array by splitting the single array into multiple sub-arrays. This has led to the enhancement in the centroid detection accuracy, without affecting the dynamic range of the sensor. The numerically constructed grating array pattern has also been synthesized by printing it on a polyester film (i.e. OHP sheet) using an ordinary laser printer. Such a grating array on the polyester film can be realised in an easy and affordable way that showed reasonable quality and uniformity. We have also proposed an improved zonal wavefront estimation algorithm which is an improved version over the well-known Southwell algorithm. The proposed algorithm has offered better wavefront estimation accuracy without much sacrifice on the processing time. It also has also showed superior performance in terms of error propagation during the estimation process.

Each of the schemes proposed in this thesis to address the issues associated with the conventional SHWS, has been demonstrated with proof-of-principle experiments. Apart from describing each of the schemes elaborately, the thesis has presented results of the various proof-of-principle experiments in order to emphasize the effectiveness of the proposed schemes. Below we also provide chapter-wise conclusion of the present thesis.

In **chapter1**, we have provided a general introduction to the research problem. We have introduced about the various types of wavefront sensors and provided a brief description about the popular Shack-Hartmann wavefront sensor (SHWS). Also, we have presented a brief overview of the various limitations associated with the sensing and estimation in a SHWS type zonal wavefront sensor. Further, we have provided a chapter-wise overview of the entire thesis.

In **chapter2**, a detailed description on wavefront sensing and wavefront estimation processes has been provided. The working principle of two important types of sensors, namely, the Shack Hartmann wavefront sensor and the Curvature wavefront sensor, falling under geometric sensors and interferometric sensors, respectively, has been described. We have then presented a detailed discussion about the two estimation methods, namely, zonal wavefront estimation and modal wavefront estimation. In the same chapter, there has also been a short introduction to the three important geometries associated with the wavefront estimation process.

In **chapter3**, we have provided a detailed theoretical description of the generation of a user defined wavefront and dynamic control of the $+1$ order focal spot positions, using a computer generated holography technique. We have then shown the construction of a grating array based zonal wavefront sensor (GAWS) using an array of binary diffraction gratings, whose working principle is similar to that of the Shack Hartmann wavefront sensor (SHWS). The efficient working of the GAWS has been illustrated experimentally for different grating array dimensions. Further, we have also demonstrated experimentally some other associated advantages of a GAWS, such as dynamic reconfiguration between various grating dimensions, high speed wavefront sensing and reduced crosstalk along vertical direction.

In **chapter4**, we have introduced an improved zonal wavefront estimation algorithm, applicable for Shack Hartmann type wavefront sensors. We have developed the necessary mathematical expressions for the proposed algorithm along with that for the Southwell algorithm. The proposed algorithm incorporates diagonal slope and phase information, in addition to the vertical and horizontal information, to estimate the phase at each grid point. We have also implemented both the improved algorithm as well as the Southwell algorithm, experimentally. Further, experimental results have been provided to demonstrate the improvement in wavefront estimation for both known wavefront and unknown wavefront, using the proposed algorithm, in comparison to the Southwell algorithm.

In **chapter5**, we have provided an analytical work out to analyze the two important sources of error associated with the improved wavefront estimation algorithm vis-a-vis the popular Southwell algorithm. We have developed the mathematical expressions for the slope measurement error which can be used to calculate the error propagation co-efficients for various grating array dimensions. We have also developed the expressions for algorithm discretization error for the improved algorithm and the Southwell algorithm. We have clearly demonstrated through the theoretical expressions that both the sources of error have less pronounced effect on the improved algorithm, in comparison to the Southwell algorithm. Further, we have also presented experimental results that validate the correctness of the theoretically developed expressions.

In **chapter6**, we have introduced a scheme to enhance the spatial resolution of the grating array based zonal wavefront sensor (GAWS) by using a sequence of laterally shifted binary grating patterns, realised with the help of the 24 bit-planes display of an FLCSLM. The proposed scheme of spatial resolution enhancement has been elaborately described, that includes capturing of all the focal spot arrays by the camera for the complete sequence, without being affected by the typical frame rate of the camera. We have also described the working of the proposed scheme by performing an experiment with different bit-plane numbers (i.e., for $b$ = 1, 4, 9 and 16). Experimental results presented have demonstrated that the proposed scheme can detect spatial wavefront features that would have been missed by the conventional method. Further, we have also provided numerical simulation results that quantify the enhancement in spatial resolution.

In **chapter7**, we have proposed a scheme to improve the accuracy of centroid detection in the grating array based zonal wavefront sensor (GAWS) by using more than one digital camera via a beam splitting mechanism. We have described the enhancement in centroid detection accuracy based on the generation of multiple subarrays of focal spots to be captured using multiple cameras. We have also shown the experimental implementation of the proposed scheme that enables describing each of the focal spots with more number of pixels and over a larger detector subaperture area. Ability of the same set-up to enhance the dynamic range of the sensor and to reduce the possibility of crosstalk between adjacent zones has also been described briefly. Further, we have also provided experimental results that demonstrates wavefront estimation accuracy as a result of improvement in centroid detection accuracy, due to use of multiple cameras in comparison to the use of a single camera.

In **chapter8**, we have introduced a zonal wavefront sensing scheme by using an array of plane diffraction gratings printed on a transparent sheet of polyester film. We have presented mathematical relations to generate a well separated $+1$ order focal spots, for a given focusing lens and also have elaborately described the synthesis of the grating array pattern. The proposed scheme does not involve any specialized and expensive devices apart from a digital camera, leading to an easy and cost effective implementation of the scheme. Further, we have provided experimental results that show the generation of $+1$ order focal spots, agreeing well with the numerical simulation results and demonstrate a reasonably accurate estimation of an applied phase profile of the incident beam.

## 9.3 Future Prospects

The research work taken up in this thesis can be extended further. Below some of such prospective research problems are discussed.

- The grating array based zonal wavefront sensor discussed in the thesis consists of circular grating elements. However, it is also possible to design diffraction grating aperture with any arbitrary shape, employing the computer generated holography technique. In future, new grating designs with newer shape of the grating element, such as hexagonal shape, that has almost 100% fill factor, can be considered. It is expected that the symmetric nature of hexagonal shape of the aperture will further help in reducing estimation error by incorporating more number of phase and slope values at equal separations from a phase point.

- Optical vortices occur naturally when a light beam propagates through the atmosphere due to a process called scintillation. Vortex point is a singular point with zero amplitude and an undefined phase. The beam carrying the vortex is found to have a helical wavefront where the phase value varies from 0 to $2n\pi$ (where n is the topological charge) along the circumference of the vortex point. Due to the undefined phase at the vortex there exists every possibility to lose information that is being carried by the light beam undergoing scintillation. Thus, it is important to locate the exact position of the singular point to eliminate the distortions on the propagating laser beam introduced by the atmosphere. Recently, it was shown that the SHWS can be used to detect singular point in an optical vortex. However, the process of wavefront sensing and estimation in the SHWS still imposes major limitations in the detection of the exact location of the singular point. In this regard, the GAWS can play an important role. Owing to the programmability of the various parameters of the sensor, the GAWS is expected to facilitate more accurate determination of the vortex point location.

- We have presented a detailed theoretical workout about the centroid (or slope) measurement error. However, we have not quantified various individual errors separately that together make up for the centroid (or slope) measurement error. Such errors include errors due to photon noise, readout noise, focal spot sampling noise, etc. Thus, in future each of these errors can be quantified separately to figure out ways to minimize them.
- In chapter 7 we have proposed a scheme to improve the accuracy of centroid detection in the GAWS by using multiple digital cameras via a beam splitting mechanism. Although, the proposed scheme showed improvement in centroid detection accuracy, but the use of multiple cameras increases its development cost significantly. However, the same objective can be accomplished using a single camera with more intermediate optics to direct the sub-arrays of focal spots onto a single camera, while sequentially displaying the sub-arrays of grating pattern on the FLCSLM.

# References

[1] Joseph M Geary. *Introduction to wavefront sensors*, volume 18. Spie Press, 1995.

[2] D Malacara-Doblado and I Ghozeil. Hartmann, hartmann–shack, and other screen tests. *Optical Shop Testing, Third Edition*, pages 361–397, 2007.

[3] Enrique J Fernández, Ignacio Iglesias, and Pablo Artal. Closed-loop adaptive optics in the human eye. *Optics letters*, 26(10):746–748, 2001.

[4] Jae Won Cha, Jerome Ballesta, and Peter TC So. Shack-hartmann wavefront-sensor-based adaptive optics system for multiphoton microscopy. *Journal of biomedical optics*, 15(4):046022–046022, 2010.

[5] B Schäfer, M Lübbecke, and K Mann. Hartmann-shack wave front measurements for real time determination of laser beam propagation parameters. *Review of scientific instruments*, 77(5):053103, 2006.

[6] TW Nicholls, GD Boreman, and JC Dainty. Use of a shack–hartmann wavefront sensor to measure deviations from a kolmogorov phase spectrum. *Optics letters*, 20(24):2460–2462, 1995.

[7] Junzhong Liang, Bernhard Grimm, Stefan Goelz, and Josef F Bille. Objective measurement of wave aberrations of the human eye with the use of a hartmann–shack wave-front sensor. *JOSA A*, 11(7):1949–1957, 1994.

[8] Tae Moon Jeong, Manoj Menon, and Geunyoung Yoon. Measurement of wavefront aberration in soft contact lenses by use of a shack–hartmann wave-front sensor. *Applied optics*, 44(21):4523–4527, 2005.

[9] Jin-Seok Lee, Ho-Soon Yang, and Jae-Won Hahn. Wavefront error measurement of high-numerical-aperture optics with a shack-hartmann sensor and a point source. *Applied optics*, 46(9):1411–1415, 2007.

[10] Peter John Rodrigo, René Lynge Eriksen, Vincent Ricardo Daria, and Jesper Glückstad. Shack-hartmann multiple-beam optical tweezers. *Optics Express*, 11(3):208–214, 2003.

[11] Lawrence E Schmutz. Wavefront measuring system with integral geometric reference (igr), May 13 1997. US Patent 5,629,765.

[12] William H Southwell. Wave-front estimation from wave-front slope measurements. *JOSA*, 70(8):998–1006, 1980.

[13] Xin Wei and Larry N Thibos. Modal estimation of wavefront phase from slopes over elliptical pupils. *Optometry & Vision Science*, 87(10):E767–E777, 2010.

[14] Daniel M Topa. Wavefront reconstruction for the shack-hartmann wavefront sensor. In *International Symposium on Optical Science and Technology*, pages 101–115. International Society for Optics and Photonics, 2002.

[15] Sophia I Panagopoulou and Daniel P Neal. Zonal matrix iterative method for wavefront reconstruction from gradient measurements. *Journal of Refractive Surgery*, 21(5):S563–S569, 2005.

[16] Roland V Shack and BC Platt. Production and use of a lenticular hartmann screen. In *Journal of the Optical Society of America*, volume 61, page 656. Amer. Inst. Physics Circulation Fulfillment Div., 500 Sunnyside Blvd, Woodbury, NY 11797-2999, 1971.

[17] Rui Liu, Daniel E Milkie, Aaron Kerlin, Bryan MacLennan, and Na Ji. Direct phase measurement in zonal wavefront reconstruction using multidither coherent optical adaptive technique. *Optics express*, 22(2):1619–1628, 2014.

[18] J. Hartmann. Objektuvuntersuchungen. *Zt. Instrumentenkd*, 24(1), 1904.

[19] Richard H Hudgin. Wave-front reconstruction for compensated imaging. *JOSA*, 67(3):375–378, 1977.

[20] David L Fried. Least-square fitting a wave-front distortion estimate to an array of phase-difference measurements. *JOSA*, 67(3):370–375, 1977.

[21] Weiyao Zou and Jannick P Rolland. Quantifications of error propagation in slope-based wavefront estimations. *JOSA A*, 23(10):2629–2638, 2006.

[22] Akondi Vyas, MB Roopashree, and B Raghavendra Prasad. Dither-based sensor for improved consistency of adaptive optics system. In *SPIE Astronomical Telescopes+ Instrumentation*, pages 773928–773928. International Society for Optics and Photonics, 2010.

[23] Lei Huang and Anand Asundi. Improvement of least-squares integration method with iterative compensations in fringe reflectometry. *Applied optics*, 51(31):7459–7465, 2012.

[24] Guanghui Li, Yanqiu Li, Ke Liu, Xu Ma, and Hai Wang. Improving wavefront reconstruction accuracy by using integration equations with higher-order truncation errors in the southwell geometry. *JOSA A*, 30(7):1448–1459, 2013.

[25] Ben C Platt and Roland Shack. History and principles of shack-hartmann wavefront sensing. *Journal of Refractive Surgery*, 17(5):S573–S577, 2001.

[26] Daniel R Neal, Justin D Mansell, James K Gruetzner, R Morgan, and Mial E Warren. Specialized wavefront sensors for adaptive optics. In *SPIE's 1995 International Symposium on Optical Science, Engineering, and Instrumentation*, pages 338–348. International Society for Optics and Photonics, 1995.

[27] JD Mansell, DR Neal, and SW Smith. Binary-optic smoothing with isotropic etching. *Applied optics*, 36(20):4644–4647, 1997.

[28] BR Boruah. Zonal wavefront sensing using an array of gratings. *Optics letters*, 35(2):202–204, 2010.

[29] Mark A A Neil, MJ Booth, and T Wilson. Dynamic wave-front generation for the characterization and testing of optical systems. *Optics letters*, 23(23): 1849–1851, 1998.

[30] BR Boruah. Dynamic manipulation of a laser beam using a liquid crystal spatial light modulator. *American Journal of Physics*, 77(4):331–336, 2009.

[31] Zacarias Malacara and Manuel Servin. *Interferogram analysis for optical testing*, volume 84. CRC press, 2016.

[32] John W Hardy, J E_ Lefebvre, and CL Koliopoulos. Real-time atmospheric compensation. *JOSA*, 67(3):360–369, 1977.

[33] Eric P Goodwin and James C Wyant. Field guide to interferometric optical testing. SPIE, 2006.

[34] Francois Roddier. Curvature sensing and compensation: a new concept in adaptive optics. *Applied Optics*, 27(7):1223–1225, 1988.

[35] Daniel Malacara. *Optical shop testing*, volume 59. John Wiley & Sons, 2007.

[36] Gary Chanan. Principles of wavefront sensing and reconstruction. *Center for Adaptive Optics (CfAO) Proceedings: Summer School on Adaptive Optics, Santa Cruz, CA*, 2000.

[37] Huaqiang Li, Helun Song, Changhui Rao, and Xuejun Rao. Accuracy analysis of centroid calculated by a modified center detection algorithm for shack–hartmann wavefront sensor. *Optics Communications*, 281(4):750–755, 2008.

[38] James W Beletic, Reinhold J Dorn, Thomas Craven-Bartle, and Barry Burke. A new ccd designed for curvature wavefront sensing. In *Optical Detectors for Astronomy II*, pages 283–309. Springer, 2000.

[39] Robert K Tyson. *Principles of adaptive optics*. CRC press, 2015.

[40] Hongyu Ren, Feng Gao, and Xiangqian Jiang. Improvement of high-order least-squares integration method for stereo deflectometry. *Applied optics*, 54 (34):10249–10255, 2015.

[41] François Roddier and Claude Roddier. Wavefront reconstruction using iterative fourier transforms. *Applied Optics*, 30(11):1325–1327, 1991.

[42] Klaus R Freischlad and Chris L Koliopoulos. Modal estimation of a wave front from difference measurements using the discrete fourier transform. *JOSA A*, 3(11):1852–1861, 1986.

[43] Wansong Li, Thorsten Bothe, Christoph von Kopylow, and Werner PO Juptner. Evaluation methods for gradient measurement techniques. In *Photonics Europe*, pages 300–311. International Society for Optics and Photonics, 2004.

[44] Lei Huang, Mourad Idir, Chao Zuo, Konstantine Kaznatcheev, Lin Zhou, and Anand Asundi. Comparison of two-dimensional integration methods for shape reconstruction from gradient data. *Optics and Lasers in Engineering*, 64:1–11, 2015.

[45] Stefan Kindermann, Andreas Neubauer, and Ronny Ramlau. A singular value decomposition for the shack–hartmann based wavefront reconstruction. *Journal of Computational and Applied Mathematics*, 236(8):2186–2199, 2012.

[46] Guang-Ming Dai. Wavefront reconstruction from slope data within pupils of arbitrary shapes using iterative fourier transform. *The Open Optics Journal*, 1:1–3, 2007.

[47] Alfredo Dubra. Wavefront sensor and wavefront corrector matching in adaptive optics. *Optics express*, 15(6):2762–2769, 2007.

[48] Gregor Gregorcic. The singular value decomposition and the pseudoinverse. *matrix*, 2(1):2, 2001.

[49] Guang-ming Dai. Modal wave-front reconstruction with zernike polynomials and karhunen–loève functions. *JOSA A*, 13(6):1218–1225, 1996.

[50] Robert J Noll. Zernike polynomials and atmospheric turbulence. *JOSA*, 66 (3):207–211, 1976.

[51] Guang-ming Dai. Modal compensation of atmospheric turbulence with the use of zernike polynomials and karhunen–loève functions. *JOSA A*, 12(10): 2182–2193, 1995.

[52] Glyn Walsh, HC Howland, and WN Charman. Objective technique for the determination of monochromatic aberrations of the human eye. *JOSA A*, 1 (9):987–992, 1984.

[53] Chengwu Cui and Vasudevan Lakshminarayanan. Choice of reference axis in ocular wave-front aberration measurement. *JOSA A*, 15(9):2488–2496, 1998.

[54] Lisa A Poyneer, Donald T Gavel, and James M Brase. Fast wave-front reconstruction in large adaptive optics systems with use of the fourier transform. *JOSA A*, 19(10):2100–2111, 2002.

[55] Max Born and Emil Wolf. Principles of optics ch. 9. *Cambridge University Press*, 7:436–445, 1999.

[56] Guang-Ming Dai. Wavefront expansion basis functions and their relationships. *JOSA A*, 23(7):1657–1668, 2006.

[57] Christopher A Palmer and Erwin G Loewen. *Diffraction grating handbook.* Newport Corporation New York, 2005.

[58] Joseph W Goodman. *Introduction to Fourier optics Ch. 4.* Roberts and Company Publishers, 2005.

[59] Bosanta R Boruah and Abhijit Das. Zonal wavefront sensor with reduced number of rows in the detector array. *Applied optics*, 50(20):3598–3603, 2011.

[60] Burkhard Buttkus. The dirac delta function and its fourier transform. In *Spectral Analysis and Filter Theory in Applied Geophysics*, pages 41–47. Springer, 2000.

[61] Truman F Kellie. Holographic article and process for making same, June 13 1978. US Patent 4,094,575.

[62] Sean F Johnston. Holography: From science to subcultures. *Optics and Photonics News*, 15(7):36–41, 2004.

[63] Bryon R Brown and Adolf W Lohmann. Complex spatial filtering with binary masks. *Applied Optics*, 5(6):967–969, 1966.

[64] BR Brown and AW Lohmann. Computer-generated binary holograms. *IBM Journal of research and Development*, 13(2):160–168, 1969.

[65] Virendra N Mahajan. Zernike circle polynomials and optical aberrations of systems with circular pupils. *Applied optics*, 33(34):8121–8124, 1994.

[66] Uzi Efron. *Spatial light modulator technology: materials, devices, and applications*, volume 47. CRC Press, 1994.

[67] URL http://www.forthdd.com/products/sxga-r3/.

[68] Eric R Fossum. Cmos image sensors: Electronic camera-on-a-chip. *IEEE transactions on electron devices*, 44(10):1689–1698, 1997.

[69] Williard S Boyle and George E Smith. Charge coupled semiconductor devices. *Bell Labs Technical Journal*, 49(4):587–593, 1970.

[70] URL https://www.baslerweb.com/en/.

[71] URL https://www.thorlabs.com/newgrouppage9.cfm?objectgroup_id=4024.

[72] URL http://sine.ni.com/nips/cds/view/p/lang/en/nid/14518.

[73] URL http://www.mellesgriot.com/Products/Lasers/Helium-Neon-Lasers.

[74] URL http://www.mellesgriot.com/Products/Lasers/DPSS-Lasers.

[75] URL http://www.microchip.com/wwwproducts/en/PIC18F2550.

[76] DW de Lima Monteiro, G Vdovin, and PM Sarro. High-speed wavefront sensor compatible with standard cmos technology. *Sensors and Actuators A: Physical*, 109(3):220–230, 2004.

[77] Giancarlo Pedrini, Wolfgang Osten, and Mikhail E Gusev. High-speed digital holographic interferometry for vibration measurement. *Applied optics*, 45(15): 3456–3462, 2006.

[78] Biswajit Pathak, Abhijit Das, and Bosanta R Boruah. High-speed zonal wavefront sensing. In *Photonics Asia*, pages 85570A–85570A. International Society for Optics and Photonics, 2012.

[79] Biswajit Pathak and Bosanta R Boruah. Reduction in the amount of crosstalk with reduced number of focal spot rows in a grating array based zonal wavefront sensor. In *International Conference on Optics & Photonics 2015*, pages 965414–965414. International Society for Optics and Photonics, 2015.

[80] Cornelis C de Visser and Michel Verhaegen. Wavefront reconstruction in adaptive optics systems using nonlinear multivariate splines. *JOSA A*, 30(1):82–95, 2013.

[81] Hui Guang, Yajun Wang, Lianxin Zhang, Lulu Li, Ming Li, and Linhong Ji. Enhancing wavefront estimation accuracy by using higher-order iterative compensations in the southwell configuration. *Applied Optics*, 56(8):2060–2067, 2017.

[82] Biswajit Pathak and Bosanta R Boruah. Improved wavefront reconstruction algorithm for shack–hartmann type wavefront sensors. *Journal of Optics*, 16 (5):055403, 2014.

[83] Mary L Boas. *Mathematical methods in the physical sciences*, volume 2. Wiley New York, 1966.

[84] James B Saunders. Measurement of wave fronts without a reference standard: Part 1. the wave-front-shearing interferometer. *J. Res. Nat. Bur. Stand*, 1961.

[85] MP Rimmer. Method for evaluating lateral shearing interferograms. *Applied optics*, 13(3):623–629, 1974.

[86] Weiyao Zou and Zhenchao Zhang. Generalized wave-front reconstruction algorithm applied in a shack–hartmann test. *Applied optics*, 39(2):250–268, 2000.

[87] Weiyao Zou and Jannick P Rolland. Iterative least-squares wavefront estimation for general pupil shapes, August 8 2006. US Patent 7,088,457.

[88] Biswajit Pathak and Bosanta R Boruah. Analysis of error propagation in an improved zonal phase-gradient model. In *SPIE/COS Photonics Asia*, pages 92721Y–92721Y. International Society for Optics and Photonics, 2014.

[89] Biswajit Pathak and Bosanta R Boruah. Investigation of algorithm discretization error in a zonal wavefront estimation process. In *SPIE LASE*, pages 973916–973916. International Society for Optics and Photonics, 2016.

[90] Klaus R Freischlad. Wave-front integration from difference data. In *San Diego'92*, pages 212–218. International Society for Optics and Photonics, 1993.

[91] Harrison H Barrett and Kyle J Myers. *Foundations of image science*. John Wiley and Sons, 2013.

[92] Gene H Golub. Cf van loan matrix computations. *The Johns Hopkins*, 1996.

[93] PS Doyle and PT Underhill. Handbook of materials modeling, 2005.

[94] Daniel R Neal and Justin D Mansell. Sub-lens spatial resolution shack-hartmann wavefront sensing, April 23 2002. US Patent 6,376,819.

[95] Wei Su, Yan Zhou, and Qing Chun Zhao. Sequential wavefront sensor, November 4 2008. US Patent 7,445,335.

[96] Wei Su and Yan Zhou. Adaptive sequential wavefront sensor with programmed control, November 12 2013. US Patent 8,579,437.

[97] Xavier Jean-François Levecq and Fabrice Harms. Device for analysing a wavefront with enhanced resolution, November 27 2007. US Patent 7,301,613.

[98] Lars Seifert, Jan Liesener, and Hans J Tiziani. The adaptive shack–hartmann sensor. *Optics Communications*, 216(4):313–319, 2003.

[99] Xiang Li, Liping Zhao, Zhong Ping Fang, Krishna Asundi Anand, Lin Seng Ong, and Herawan Rinov. Optical wavefront sensor and optical wavefront sensing method, April 17 2012. US Patent 8,158,917.

[100] K Buse and M Luennemann. 3d imaging: wave front sensing utilizing a birefringent crystal. *Physical review letters*, 85(16):3385, 2000.

[101] Gregory A Howland, Daniel J Lum, and John C Howell. Compressive wavefront sensing with weak values. *Optics express*, 22(16):18870–18880, 2014.

[102] M Schwertner, MJ Booth, and T Wilson. Wavefront sensing based on rotated lateral shearing interferometry. *Optics Communications*, 281(2):210–216, 2008.

[103] Fengzhao Dai, Jie Li, Xiangzhao Wang, and Yang Bu. Exact two-dimensional zonal wavefront reconstruction with high spatial resolution in lateral shearing interferometry. *Optics Communications*, 367:264–273, 2016.

[104] Biswajit Pathak and Bosanta R Boruah. Zonal wavefront sensing with enhanced spatial resolution. *Optics Letters*, 41(23):5600–5603, 2016.

[105] J Primot, G Rousset, and JC Fontanella. Deconvolution from wave-front sensing: a new technique for compensating turbulence-degraded images. *JOSA A*, 7(9):1598–1608, 1990.

[106] Xiaoming Yin, Xiang Li, Liping Zhao, and Zhongping Fang. Automatic centroid detection for shack-hartmann wavefront sensor. In *Advanced Intelligent Mechatronics, 2009. AIM 2009. IEEE/ASME International Conference on*, pages 1986–1991. IEEE, 2009.

[107] Genrui Cao and Xin Yu. Accuracy analysis of a hartmann-shack wavefront sensor operated with a faint object. *Optical Engineering*, 33(7):2331–2335, 1994.

[108] S Thomas, T Fusco, A Tokovinin, M Nicolle, V Michau, and G Rousset. Comparison of centroid computation algorithms in a shack–hartmann sensor. *Monthly Notices of the Royal Astronomical Society*, 371(1):323–336, 2006.

[109] Jorge Ares and Justo Arines. Influence of thresholding on centroid statistics: full analytical description. *Applied optics*, 43(31):5796–5805, 2004.

[110] KL Baker and MM Moallem. Iteratively weighted centroiding for shack-hartmann wave-front sensors. *Optics express*, 15(8):5147–5159, 2007.

[111] Ling Wei, Guohua Shi, Jing Lu, Jinsheng Yang, Xiqi Li, and Yudong Zhang. Centroid offset estimation in the fourier domain for a highly sensitive shack–hartmann wavefront sensor. *Journal of Optics*, 15(5):055702, 2013.

[112] Xiaoming Yin, Xiang Li, Liping Zhao, and Zhongping Fang. Adaptive thresholding and dynamic windowing method for automatic centroid detection of digital shack-hartmann wavefront sensor. *Applied optics*, 48(32):6088–6098, 2009.

[113] M Nicolle, T Fusco, G Rousset, and V Michau. Improvement of shack–hartmann wave-front sensor measurement for extreme adaptive optics. *Optics letters*, 29(23):2743–2745, 2004.

[114] Sung-Hoon Baik, Seung-Kyu Park, Cheol-Jung Kim, and Byungheon Cha. A center detection algorithm for shack–hartmann wavefront sensor. *Optics & Laser Technology*, 39(2):262–267, 2007.

[115] Thierry Fusco, Magalie Nicolle, Gerard Rousset, Vincent Michau, Jean-Luc Beuzit, and David Mouillet. Optimization of a shack-hartmann-based wavefront sensor for xao systems. In *Proceedings of SPIE*, volume 5490, pages 1155–1166, 2004.

[116] Justo Arines and Jorge Ares. Minimum variance centroid thresholding. *Optics letters*, 27(7):497–499, 2002.

[117] Jorge Ares and Justo Arines. Effective noise in thresholded intensity distribution: influence on centroid statistics. *Optics letters*, 26(23):1831–1833, 2001.

[118] JF Ren, CH Rao, and QM Li. An adaptive threshold selection method for hartmann-shack wavefront sensor. *Opto-electronic Engineering*, 1:000, 2002.

[119] Justo Arines and Jorge Ares. Significance of thresholding processing in centroid based gradient wavefront sensors: effective modulation of the wavefront derivative. *Optics communications*, 237(4):257–266, 2004.

[120] Tenghao Li, Lei Huang, and Mali Gong. Wavefront sensing for a nonuniform intensity laser beam by shack–hartmann sensor with modified fourier domain centroiding. *Optical Engineering*, 53(4):044101–044101, 2014.

[121] Ling Wei, Jieling He, Yi He, Jinsheng Yang, Xiqi Li, Guohua Shi, and Yudong Zhang. Error analysis for the fourier domain offset estimation algorithm. *Optics Communications*, 361:110–115, 2016.

[122] P Arulmozhivarman, L Praveen Kumar, and AR Ganesan. Measurement of moments for centroid estimation in shack–hartmann wavefront sensorâĂŤa wavelet-based approach and comparison with other methods. *Optik-International Journal for Light and Electron Optics*, 117(2):82–87, 2006.

[123] Scott A Sallberg, Byron M Welsh, and Michael C Roggemann. Maximum a posteriori estimation of wave-front slopes using a shack–hartmann wave-front sensor. *JOSA A*, 14(6):1347–1354, 1997.

[124] Geunyoung Yoon. Large dynamic range shack-hartmann wavefront sensor, August 19 2008. US Patent 7,414,712.

[125] Chia-Yu Ai. Apparatus and method for measuring a wavefront using a screen with apertures adjacent to a multi-lens array, April 15 2003. US Patent 6,548,797.

[126] Daniel R Neal and Justin D Mansell. Apodized micro-lenses for hartmann wavefront sensing and method for fabricating desired profiles, December 2 2003. US Patent 6,656,373.

[127] Bernd Schäfer and Klaus Mann. Determination of beam parameters and coherence properties of laser radiation by use of an extended hartmann-shack wave-front sensor. *Applied optics*, 41(15):2809–2817, 2002.

[128] Vinna Lin, Hsiang-Chun Wei, Hsin-Ta Hsieh, and Guo-Dung John Su. An optical wavefront sensor based on a double layer microlens array. *Sensors*, 11 (11):10293–10307, 2011.

[129] H Ottevaere, R Cox, Hans-Peter Herzig, T Miyashita, K Naessens, M Taghizadeh, R Völkel, HJ Woo, and H Thienpont. Comparing glass and plastic refractive microlenses fabricated with different technologies. *Journal of Optics A: Pure and Applied Optics*, 8(7):S407, 2006.

[130] GC Firestone and AY Yi. Precision compression molding of glass microlenses and microlens arraysâĂŤan experimental study. *Applied optics*, 44(29):6115–6122, 2005.

[131] AY Yi and L Li. Design and fabrication of a microlens array by use of a slow tool servo. *Optics letters*, 30(13):1707–1709, 2005.

[132] Sebastian Stoebenau and Stefan Sinzinger. Ultraprecision machining techniques for the fabrication of freeform surfaces in highly integrated optical microsystems. In *SPIE Optical Engineering+ Applications*, pages 742608–742608. International Society for Optics and Photonics, 2009.

[133] V Lin, HC Wei, HT Hsieh, JL Hsieh, and GD J Su. Design and fabrication of long-focal-length microlens arrays for shack-hartmann wavefront sensors. *IET Micro & Nano Letters*, 6(7):523–526, 2011.

[134] Otavio Gomes De Oliveira and Davies William de Lima Monteiro. Optimization of the hartmann–shack microlens array. *Optics and Lasers in Engineering*, 49(4):521–525, 2011.

[135] Johannes Pfund, Norbert Lindlein, and Johannes Schwider. Misalignment effects of the shack–hartmann sensor. *Applied optics*, 37(1):22–27, 1998.

[136] Jorge Ares, Teresa Mancebo, and Salvador Bara. Position and displacement sensing with shack–hartmann wave-front sensors. *Applied Optics*, 39(10):1511–1520, 2000.

[137] Biswajit Pathak, Suraj Kumar, and Bosanta R Boruah. Zonal wavefront sensing using a grating array printed on a polyester film. *Review of Scientific Instruments*, 86(12):125002, 2015.

# Publications/Conference/Achievements

## (a) Patents:

1. **Biswajit Pathak**, Rahul Kesarwani, Bosanta R. Boruah and Alika Khare, “System, Apparatus and Method for Monitoring of Surface Profile and Thickness Measurement in Thin Films", Patent Application No.: PCT/IB2016/05426 18 July, 2016; Publication No.: WO2017098343 A1, 15 June, 2017 (International).

2. **Biswajit Pathak**, Rahul Kesarwani, Bosanta R. Boruah and Alika Khare, “System, Apparatus and Method for Monitoring of Surface Profile and Thickness Measurement in Thin Films", Patent Application No.: 4088/DEL/2015, 12 December, 2015 (National).

3. **Biswajit Pathak** and Bosanta R. Boruah, “A Method and Device for Zonal Wavefront Sensing by Beam Splitting", Patent Application No.: 3935/DEL/2014, 26 December, 2014 (National).

4. **Biswajit Pathak** and Bosanta R. Boruah, “A Method and Device for Zonal Wavefront Sensing via Sequential Spatially Shifted Grating Array Patterns", Patent Application No.: 3752/DEL/2014, 18 December, 2014 (National).

## (b) Journals and Proceedings:

1. **Biswajit Pathak** and Bosanta R. Boruah, “Improvement in Error Propagation in the Shack-Hartmann type Zonal Wavefront Sensors", 2017 (Under Review, Journal of Optical Society of America A).

2. **Biswajit Pathak** and Bosanta R. Boruah, “A Zonal Wavefront Sensor with Multiple Detector Planes", 2017 (in Progress).

3. **Biswajit Pathak** and Bosanta R. Boruah, “Advantages Associated with a Zonal Wavefront Sensor Using only One Row of Focal Spots", 2017 (in Progress).

4. **Biswajit Pathak** and Bosanta R. Boruah, “Zonal Wavefront Sensing with Enhanced Spatial Resolution", Optics Letters, Vol. 41(23), 5600-5603 (2016).

5. **Biswajit Pathak**, Suraj Kumar and Bosanta R. Boruah, “Zonal Wavefront Sensing Using a Grating Array Printed on a Polyester Film", Review of Scientific Instruments, Vol. 86 (12) 125002 (2015).

6. **Biswajit Pathak** and Bosanta R. Boruah, “Improved Wavefront Reconstruction Algorithm for Shack-Hartmann Type Wavefront Sensors", Journal of Optics (IOP), Vol. 16 (5) 055403 (2014) **(was selected as Journal of Optics paper of the week during 18-25, April 2014)**.

7. **Biswajit Pathak** and Bosanta R. Boruah, “Investigation of Algorithm Discretization Error in a Zonal Wavefront Estimation Process", Proceedings of SPIE: 9739 973916 (2016).

8. **Biswajit Pathak** and Bosanta R. Boruah, “Binary Hologram Based High Speed Zonal Wavefront Sensing with Reduced Estimation Time", Proceedings of SPIE: 9741 97410T (2016).

9. **Biswajit Pathak** and Bosanta R. Boruah, “Reduction in the Amount of Crosstalk with Reduced Number of Focal Spot Rows in a Grating Array Based Zonal Wavefront Sensor", Proceedings of SPIE: 9654 965414 (2015).

10. **Biswajit Pathak** and Bosanta R. Boruah, “Analysis of Error Propagation in an Improved Zonal Phase-Gradient Model", Proceedings of SPIE: 9272 92721Y (2014).

11. **Biswajit Pathak** and Bosanta R. Boruah, “Zonal Wavefront Estimation Using an Array of Hexagonal Grating Patterns", Proceedings of AIP: Vol. 1620, pp. 86-91 (2014).

12. **Biswajit Pathak**, Abhijit Das and Bosanta R. Boruah, “High-Speed Zonal Wavefront Sensing", Proceedings of SPIE: 8557 85570A (2012).

### (c) Conference Presentations:

1. International Topical Meeting on Applied and Adaptive Optics, (INTOPMAA), IIST, Kerala, India (2017), **Biswajit Pathak** and Bosanta R. Boruah, “Zonal Wavefront Sensing with Enhanced Spatial Resolution and Improved Centroid Detection Accuracy".

2. International Topical Meeting on Applied and Adaptive Optics, (INTOPMAA), IIST, Kerala, India (2017), **Biswajit Pathak**, S. S. Goutam Buddha and Bosanta R. Boruah, "Comparison of Centroid Detection Algorithms in Atmospheric Turbulence Condition".

3. International Conference on Light and Light based Technologies, Tezpur University, India (2016), **Biswajit Pathak** and Bosanta R. Boruah, "Spatial Resolution Enhancement Using Grating Array Based Zonal Wavefront Sensor".

4. International Conference on Light and Light based Technologies, Tezpur University, India (2016), **Biswajit Pathak** and Bosanta R. Boruah, "Zonal Wavefront Sensing with Improved Accuracy".

5. SPIE Photonics West - 2016, California, USA (2016), **Biswajit Pathak** and Bosanta R. Boruah, "Investigation of Algorithm Discretization Error in a Zonal Wavefront Estimation Process".

6. SPIE Photonics West - 2016, California, USA (2016), **Biswajit Pathak** and Bosanta R. Boruah, "Binary Hologram Based High Speed Zonal Wavefront Sensing with Reduced Estimation Time".

7. South Asian Workshop on Optics & Photonics, Guwahati, India (2015), **Biswajit Pathak** and Bosanta R. Boruah, "Development of a Low-Cost Zonal Wavefront Sensing Method".

8. TE-QIP Symposium to Celebrate the 2015 International Year of Light, Guwahati, India (2015), Santanu Konwar, **Biswajit Pathak** and Bosanta R. Boruah, "Hologram Based Wavefront Sensor of Light Beams".

9. International Conference on Optics and Photonics, Calcutta, India (2015), **Biswajit Pathak** and Bosanta R. Boruah, "Reduction in the Amount of Crosstalk with Reduced Number of Focal Spot Rows in a Grating Array Based Zonal Wavefront Sensor".

10. Photonics Asia, Beijing, China (2014), **Biswajit Pathak** and Bosanta R. Boruah, "Analysis of Error Propagation in an Improved Zonal Phase-Gradient Model".

11. OPTICS$'$-14: International Conference on Light, Kerala, India (2014), **Biswajit Pathak** and Bosanta R. Boruah, “Zonal Wavefront Estimation Using an Array of Hexagonal Grating Patterns".

12. XXXVII National Symposium of Optical Society of India, Pondicherry, India (2013), **Biswajit Pathak** and Bosanta R. Boruah, “Wavefront Sensing Using a Grating Array with High Frame Rate".

13. XXXVII National Symposium of Optical Society of India, Pondicherry, India (2013), **Biswajit Pathak** and Bosanta R. Boruah, “An Improved Zonal Wavefront Reconstructor Slope Geometry".

14. Photonics Asia, Beijing, China (2012), **Biswajit Pathak**, Abhijit Das and Bosanta R. Boruah, “High-Speed Zonal Wavefront Sensing".

15. First IITG Optical Society of America Student Chapter Workshop on Optics, Guwahati, India (2012), **Biswajit Pathak** and Bosanta R. Boruah, “An Improved Slope Model for Zonal Wavefront Reconstruction".

### (d) Training/Workshop Attended:

1. LabVIEW Core-I And Core-II Course, National Instruments Bangalore held from 23/04/12-27/04/12.

2. IEEE Matlab Workshop, I.I.T. Guwahati held from 22/06/13-23/06/13.

3. IEEE Workshop on Advanced MATLAB, I.I.T. Guwahati held from 30/08/14-31/08/14.

4. The IEEE Workshop on Power, Mechatronics, Robotics and Control, I.I.T. Guwahati PMRC 2015 held from 29/08/15-30/08/15.

5. Third IEEE Workshop on Advanced MATLAB Applications, I.I.T. Guwahati held from 01/10/16-02/10/16.

6. Workshop on Intellectual Property Rights-Invent, Protect & Prosper, I.I.T. Guwahati held from 30/11/16-01/12/16.

### (e) Achievements (Related to PhD Work):

1. Received **third best poster presentation award** for the paper entitled “Zonal Wavefront Sensing with Enhanced Spatial Resolution and Improved Centroid Detection Accuracy", in the International Topical Meeting on Applied and Adaptive Optics, 2017 (INTOPMAA), organized by IIST, Kerala, India.

2. Received **Departmental (Physics) best paper award** for the paper entitled “Liquid Crystal Spatial Light Modulator Based Wavefront Sensing and its Application", in the Research Conclave, 2017, organized by IIT Guwahati, India.

3. Received **Optical Society of India second best contributory paper award** in the oral session for the paper entitled “Spatial Resolution Enhancement in a Grating Array Based Zonal Wavefront Sensor", in the International Conference on Light and Light based Techology, 2016, held at Tezpur University, India.

4. Received **Optical Society of India second best contributory paper award** in the poster session for the paper entitled “Zonal Wavefront Sensing with Improved Accuracy", in the International Conference on Light and Light based Techology, 2016, held at Tezpur University, India.

5. Received **1st runner-up for the paper** entitled “Wavefront Sensing Using Computer Generated Holography Technique", in the Research Conclave, 2016, organized by IIT Guwahati, India.

6. Received **“SPIE Student Officer Travel Grant" (USD 3190)** to present two contributory papers at “SPIE Photonics West-2016", at San Francisco, California, USA from 13-18 Feb, 2016, organized by SPIE.

7. Selected for the prestigious **“Newport Spectra-Physics Research Excellence Travel Awards"** (USD 750) to present two contributory papers at “SPIE Photonics West-2016", at San Francisco, California, USA from 13-18 Feb, 2016, organized by SPIE.

8. Won cash prize of Rs. 20, 000/- for the project proposal entitled “Development of a Bio-speckle Analyser with an Edge-detector Operator" in the

**“GBP’s Talent Search Contest On Innovative Research Ideas Leading To Entrepreneurial Venture In Biotechnology And Allied Areas"** in the Assam Biotech Conclave, 2015, held at Guwahati Biotechnology Park, Guwahati, India.

9. The Journal entitled, “Improved Wavefront Reconstruction Algorithm for Shack-Hartmann Type Wavefront Sensors", Journal of Optics (IOP), Vol. 16 (5) 055403(2014) was selected as the **Journal of Optics paper of the week during 18-25, April 2014**.
10. Received the **best paper award** in the Optical Instrumentation & Techniques category for the paper entitled “Zonal Wavefront Estimation Using an Array of Hexagonal Grating Patterns", in the OPTICS$'$14: International Conference on Light, 2014, held at Kerala, India.
11. Received the **best oral presentation award** in the Optical Instrumentation and Optical Metrology categories for the paper entitled “An Improved Zonal Wavefront Reconstructor Slope Geometry", in the XXXVII National Symposium of Optical Society of India, 2013, held at Pondicherry, India.
12. Received the **Optical Society of America best student contributory paper award** for the paper entitled “An Improved Slope Model for Zonal Wavefront Reconstruction", in the First IITG OSA Student Chapter Workshop on Optics, 2012, held at IIT Guwahati, India.

***